

**Characterization of alteration and mineralization at the Archean Grey Fox and Hislop
magmatic-hydrothermal gold deposits, Matheson, Ontario**

by

Christopher Hugh Kelly

A thesis submitted in partial fulfillment
of the requirements for the degree of
Master of Science (MSc) in Geology

The Faculty of Graduate Studies
Laurentian University, Sudbury,
Ontario, Canada

© Christopher Hugh Kelly, 2021

THESIS DEFENCE COMMITTEE/COMITÉ DE SOUTENANCE DE THÈSE
Laurentian Université/Université Laurentienne
Faculty of Graduate Studies/Faculté des études supérieures

Title of Thesis Titre de la thèse	Characterization of alteration and mineralization at the Archean Grey Fox and Hislop magmatic-hydrothermal gold deposits, Matheson, Ontario	
Name of Candidate Nom du candidat	Kelly, Christopher Hugh	
Degree Diplôme	Master of Science	
Department/Program Département/Programme	Geology	Date of Defence Date de la soutenance June 30, 2021

APPROVED/APPROUVÉ

Thesis Examiners/Examineurs de thèse:

Dr. Daniel Kontak
(Co-Supervisor/Co-directeur(trice) de thèse)

Dr. Bruno Lafrance
(Co-Supervisor/Co-directeur(trice) de thèse)

Dr. Gyorgyi Tuba
(Committee member/Membre du comité)

Dr. Noémie Fayol
(External Examiner/Examineur externe)

Approved for the Faculty of Graduate Studies
Approuvé pour la Faculté des études supérieures
Tammy Eger, PhD
Vice-President Research (Office of Graduate Studies)
Vice-rectrice à la recherche (Bureau des études supérieures)
Laurentian University / Université Laurentienne

ACCESSIBILITY CLAUSE AND PERMISSION TO USE

I, **Chris Kelly**, hereby grant to Laurentian University and/or its agents the non-exclusive license to archive and make accessible my thesis, dissertation, or project report in whole or in part in all forms of media, now or for the duration of my copyright ownership. I retain all other ownership rights to the copyright of the thesis, dissertation or project report. I also reserve the right to use in future works (such as articles or books) all or part of this thesis, dissertation, or project report. I further agree that permission for copying of this thesis in any manner, in whole or in part, for scholarly purposes may be granted by the professor or professors who supervised my thesis work or, in their absence, by the Head of the Department in which my thesis work was done. It is understood that any copying or publication or use of this thesis or parts thereof for financial gain shall not be allowed without my written permission. It is also understood that this copy is being made available in this form by the authority of the copyright owner solely for the purpose of private study and research and may not be copied or reproduced except as permitted by the copyright laws without written authority from the copyright owner.

ABSTRACT

The Abitibi Greenstone belt (AGB) is host to some of the world's largest gold deposits and their study has led to various gold deposit models and classifications. The latter includes a syenite-associated deposit type, which was first recognized in the early 2000s. This type of mineralization is present at the Grey Fox and Hislop deposits, which are located 80 km east of Timmins, Ontario. A study of their geologic setting, alteration, mineralogy, mineral chemistry, veining styles, and metal associations, suggest that these deposits, as well as others in the area, developed in different zones of a larger magmatic-hydrothermal system associated with alkalic intrusions of probable Timiskaming age (i.e., <2680 Ma). As such, they formed relatively early in the deformation history of the belt and predate the formation of the more common orogenic or greenstone-hosted quartz-carbonate vein deposits, such as the nearby Black Fox, which make up much of the gold budget in the AGB. A strong host-rock control is present at both deposits and their complex alteration histories provide insights on the formation of multiple mineralization styles within a single system. These different mineralization styles are described here to provide guidelines for mineral exploration for this deposit type in the Abitibi greenstone belt, as well as in other greenstone belts globally.

Keywords: Hydrothermal gold, alteration, geochemistry, syenite-associated, intrusion-associated, Grey Fox Deposit, Hislop Mine, Black Fox Mine, Abitibi greenstone belt, Porcupine-Destor

CO-AUTHORSHIP STATEMENT

This thesis is written to be submitted to a journal following modification for length and content with the candidate as the first author and co-authored by D.J. Kontak, B. Lafrance, G. Tuba, and I. Chappell. Field mapping was completed by the candidate and I. Chappell. The candidate also completed the following tasks: relogging of drill core; sample selection; sample preparation, including 1) cutting pucks that were made into thin sections by Willard Desjardin, technologist at the Harquail School of Earth Sciences and 2) prepare sample material sent to ALS laboratories for geochemistry; characterization of samples through petrography and scanning electron microscope; treatment and interpretation of whole-rock geochemical data; LA-ICP-MS data interpretation (collection completed by Joseph Petrus, Geochemical Fingerprinting Laboratory at Laurentian University); and construction of the figures and tables in the thesis. The interpretations and writing presented in this thesis benefited and were developed through discussions with, and review by, the co-authors, but the candidate is responsible for the interpretations and conclusions presented.

ACKNOWLEDGEMENTS

I would like to thank my supervisors, Dr. Daniel Kontak and Dr. Bruno Lafrance, whose encouragement and support throughout my thesis, particularly in the final stages, helped get me past the finish line, and Dr. Györgi Tuba, who has been a pillar of encouragement, knowledge, and guidance.

I thank all the professors at the Harquail School of Mines, who were always available to lend their expertise for any question, as well as the staff, who help myself and all of us students every day. In particular, I would like to thank Roxane Mehes and Edda Bozzato, who on more occasions than I can count helped me navigate Laurentian, and Willard Desjardin, William Zhe, and Joseph Petrus, without whom my research would not be possible. A large thanks to all my fellow graduate students as well, which there are too many to name, but whose support and discussions helped shape me as a geologist and a person.

I thank Kirkland Lake Gold and McEwen Mining, who through their generous funding and openness for information sharing made this project possible, and the exploration teams from both companies, who provided an open environment for discussion and whose knowledge built the foundation of my research.

Finally, I would like to thank my family: my father, Michael, mother, Judy, and sister, Lisa, who have been there for me through every step.

Table of Contents

Abstract	iii
Co-Authorship Statement.....	iv
Acknowledgements.....	v
List of Tables	ix
List of Figures	x
List of Appendices	xiii
1 Chapter 1: Introduction to Thesis	1
1.1 Introduction	1
1.2 Objectives of the Thesis	1
1.3 Structure of Thesis	2
2 Chapter 2: Characterization of alteration and mineralization at the Archean Grey Fox and Hislop magmatic-hydrothermal gold deposits, Matheson, Ontario	4
2.1 Introduction	4
2.2 Geologic Setting	5
2.3 Deposit Geology and Mineralization	7
2.4 Sampling and Analytical Techniques.....	9
2.4.1 Field work and sampling	9
2.4.2 Petrography and SEM-EDS analysis.....	10
2.4.3 Whole-rock lithochemistry	10

2.4.4	Laser ablation mapping of pyrite	11
2.4.5	Zircon separation for geochronology	11
2.5	Petrological Characterization of ore Hosting units	11
2.5.1	Metavolcanic units	12
2.5.2	Tuffaceous metasedimentary rocks.....	14
2.5.3	Felsic-intermediate intrusions	15
2.5.4	Lamprophyre dikes.....	16
2.6	Mineralogy and Distribution of Alteration Types.....	17
2.6.1	Grey Fox.....	17
2.6.2	Hislop	20
2.6.3	Black Fox	23
2.7	Relationship of Gold Mineralization to Veining.....	24
2.7.1	Grey Fox and Hislop vein systems and associated gold mineralization	24
2.7.2	Veining and associated gold mineralization at the Black Fox deposit.....	26
2.8	Micro-Scale Chemistry of Alteration and Mineral Phases.....	27
2.8.1	Raster analysis.....	27
2.8.2	Chlorite, carbonate, and pyrite chemistry	28
2.9	Metal Associations	30
2.9.1	Mass balance calculations	30
2.9.2	Grey Fox whole-rock metal associations	31

2.9.3	Element distribution maps of pyrites	31
2.10	Discussion.....	33
2.10.1	Chemical and textural features of host metavolcanic rocks at Grey Fox and Hislop deposits	33
2.10.2	Nature of felsic-intermediate intrusions and lamprophyres at Hislop, Grey Fox, and Black Fox	35
2.10.3	Nature of mineralization at Grey Fox	37
2.10.4	Nature of mineralization at Hislop	44
2.10.5	Mineralization at Black Fox	49
2.10.6	Comparison of the deposits in the Hislop township.....	51
2.10.7	Related mineralized zones in the Hislop township	53
2.10.8	Genetic model for early mineralization in the Hislop township	54
2.10.9	Syenite-associated deposits elsewhere in the Abitibi.....	57
2.10.10	Implications for exploration	58
2.11	Conclusions	59
2.12	References	61
2.13	Tables.....	69
2.14	Figures	76
Appendix A: Whole-Rock Lithochemistry results.....		118
Appendix B: Pyrite Laser Ablation Maps.....		131

LIST OF TABLES

Table 1: Mineral abbreviations used to label microscope and SEM-EDS photomicrographs.	69
Table 2: Whole-rock lithochemistry for the three ultramafic samples from the Black Fox deposit.....	70
Table 3: Sample information for felsic intrusions at Hislop, Grey Fox, and Black Fox .	72
Table 4: Summary of major minerals (A) and sulphides/trace minerals (B) present in each alteration assemblage in the different zones of the Grey Fox deposit	73
Table 5: Summary of minerals present in the different alteration assemblages of the main units at the Hislop deposit.....	74
Table 6: Metal additions determined through isocon diagrams for each alteration assemblage at Grey Fox and Hislop.....	74
Table 7: Summary of mineral deposits in the Hislop Township that may have formed as part of the Hislop magmatic-hydrothermal event	75

LIST OF FIGURES

Figure 1: Geology and distribution of gold deposits in the southern Abitibi greenstone belt.....	76
Figure 2: Simplified geology of the Hislop Township with locations of the studied deposits (Hislop, Grey Fox, Black Fox) as well as historical gold mines and occurrences in the vicinity (Ross, Royal Oak-Gold Pike, Gibson).....	77
Figure 3: General geology and mineralization features of the Grey Fox and Hislop deposits	78
Figure 4: Discrimination diagrams of metavolcanic units from Hislop, Grey Fox, and Black Fox	79
Figure 5: Macro- and micro-textural features of metavolcanic units at Grey Fox and Hislop	80
Figure 6: Additional rock units from the Grey Fox and Hislop deposits	81
Figure 7: Chemical discrimination diagrams for felsic intrusions at Hislop, Grey Fox, and Black Fox	83
Figure 8: Chemical discrimination diagrams for lamprophyres (LAM).....	84
Figure 9: Core photos showing the Grey Fox Contact Zone with different zones of alteration and veining outlined.....	85
Figure 10: Examples of the chlorite-albite-quartz alteration from the different zones at Grey Fox	86
Figure 11: Examples of the sodic-carbonate alteration at Grey Fox in	87
Figure 12: Examples of the muscovite-chlorite alteration at Grey Fox.....	89
Figure 13: Vein-associated K-feldspar alteration and decarbonatization at Grey Fox....	90

Figure 14: Examples of potassic alteration at Hislop	91
Figure 15: Examples of sodic-carbonate alteration at Hislop.....	92
Figure 16: Alteration in the ultramafic metavolcanics at the Black Fox deposit	93
Figure 17: Orientations and conjugate features of vein sets	94
Figure 18: Vein samples from the Grey Fox deposit.....	95
Figure 19: Au-associated veins present in the pit wall at Hislop.....	96
Figure 20: Veins at the Black Fox deposit.....	97
Figure 21: Semi-quantitative SEM-EDS raster analysis of different alteration types from mafic metavolcanic rocks of the Grey Fox Contact Zone	98
Figure 22: Chlorite chemistry, as determined from SEM-EDS analysis, for different alteration types and host rocks.....	99
Figure 23: Dolomite chemistry, as determined from SEM-EDS analysis, for different alteration types	100
Figure 24: Diagrams showing the chemistry of pyrite from SEM-EDS analysis.....	101
Figure 25: Isocon diagrams constructed after Grant (1986) for the sodic-carbonate alteration and the chlorite-rich alteration at the Grey Fox deposit	102
Figure 26: Isocon diagrams constructed after Grant (1986) for the K-feldspar-carbonate alteration at Hislop	103
Figure 27: Isocon diagrams constructed after Grant (1986) for the sodic-carbonate alteration at Hislop.....	104
Figure 28: Plot of metal associations from whole-rock lithogeochemical data for variably altered and mineralized samples from Grey Fox	105

Figure 29: Auriferous pyrite from the mafic metavolcanics in the Grey Fox Contact Zone	106
Figure 30: Auriferous pyrite from the intermediate metavolcanics in the Grey Fox 147 Zone	107
Figure 31: Auriferous pyrite from the felsic metavolcanics in the Hislop deposit.....	108
Figure 32: Cubic pyrite from the mineralized felsic intrusion from the Black Fox deposit	109
Figure 33: Box and whisker plots for metals in pyrite, as determined from LA ICP-MS analysis, from the Grey Fox (Contact and 147 Zones), Hislop, and Black Fox deposits.	110
Figure 34: Paragenesis of alteration and mineralization for the three ore zones at the Grey Fox deposit.....	111
Figure 35: A plot of $\log(m_{KCL+K^+}/m_{HCl+H^+})$ versus Temperature showing the stability fields for K-bearing alteration phases.....	112
Figure 36: Octahedral pyrite with the cross-section displayed to produce a hexagonal shape	113
Figure 37: Alteration paragenesis for the Hislop deposit	114
Figure 38: A simplified summary of the different geological events inferred to have constructed the AGB, with interpreted intervals of gold emplacement.....	115
Figure 39: Interpretation of the Hislop magmatic-hydrothermal system as a time slice after mineralization but before subsequent deformation in the area	117

LIST OF APPENDICES

Appendix A: Whole-Rock Lithochemistry results..... 118

Appendix B: Pyrite Laser Ablation Maps..... 131

1 CHAPTER 1: INTRODUCTION TO THESIS

1.1 INTRODUCTION

The Abitibi greenstone belt (ABG) of northern Ontario and Quebec hosts abundant gold deposits of differing size and styles. An association - be it spatial or genetic - between felsic, generally alkali, intrusions and gold mineralization has long been known and more recently classified as intrusion (syenite)-associated deposits (IAD), and the formation of these deposits is linked to that of the Timiskaming basin (ca. ≤ 2680 Ma) (Robert, 2001; Kontak et al., 2008; Bleeker, 2015; Fayol and Jébrak, 2017). During deformation of these basins, the early deposits are overprinted by subsequent alteration and deformation, which is also associated with gold mineralization (Dubé and Mercier-Langevin, 2020; Bleeker, 2015; Bateman et al., 2008), making it difficult to identify and characterize them. The Grey Fox and Hislop deposits near Matheson (Ontario) provide a rare chance to study an undeformed IAD system, where the two deposits are interpreted to have formed in different zones of a larger magmatic-hydrothermal system. This study aims to characterize these two deposits in terms of host rocks, alteration, veining, and metal associations to provide insight into deposit variability within a single system and develop a genetic model for their formation. Furthermore, this mineralization style is compared with the nearby Black Fox deposit, which is more typical of the greenstone-hosted quartz-carbonate vein deposits of the AGB.

1.2 OBJECTIVES OF THE THESIS

By studying the Grey Fox and Hislop gold deposits, this study aims to contribute to the understanding of the syenite-associated classification of gold deposits and provide further details into the variability that can occur in a single system. The main objectives of this thesis are:

1. Characterize the Grey Fox and Hislop deposits in terms of host rock units, alteration (mineralogy, mineral chemistry, and mass balance), veining, metal associations, and pyrite chemistry.
2. Establish a genetic model for the formation of the Grey Fox and Hislop deposits and put their formation in context of the current understanding of events in the history of the Abitibi greenstone belt.
3. Compare and contrast the syenite-associated style of mineralization to the more commonly described orogenic systems, specifically using the nearby Black Fox deposit.
4. Through the understanding developed in this study, provide insight for further exploration for intrusion-associated mineralization in Archean greenstone belts.

1.3 STRUCTURE OF THESIS

This thesis consists of two chapters. The first chapter is a general introduction to the thesis that provides background information and presents the thesis objectives. Chapter 2 is written as a paper to be submitted to a journal following modification of content and length and is entitled, “Characterization of alteration and mineralization at the Archean Grey Fox and Hislop magmatic-hydrothermal gold deposits, Matheson, Ontario”. Co-authors on this manuscript are:

- Kontak, D.J., Mineral Exploration Research Centre, Harquail School of Earth Sciences, Laurentian University, 935 Ramsey Lake Road, Sudbury, Ontario, P3E 2C6
- Lafrance, B., Mineral Exploration Research Centre, Harquail School of Earth Sciences, Laurentian University, 935 Ramsey Lake Road, Sudbury, Ontario, P3E 2C6
- Tuba, G., Mineral Exploration Research Centre, Harquail School of Earth Sciences, Laurentian University, 935 Ramsey Lake Road, Sudbury, Ontario, P3E 2C6

- Chappell, I., Mineral Exploration Research Centre, Harquail School of Earth Sciences,
Laurentian University, 935 Ramsey Lake Road, Sudbury, Ontario, P3E 2C6

2 CHAPTER 2: CHARACTERIZATION OF ALTERATION AND MINERALIZATION AT THE ARCHEAN GREY FOX AND HISLOP MAGMATIC-HYDROTHERMAL GOLD DEPOSITS, MATHESON, ONTARIO

2.1 INTRODUCTION

The Archean Abitibi greenstone belt (AGB) stretches from Timmins in Ontario to Val d'Or in Quebec. It is one of the world's most prolific gold districts with over 145 Moz of gold production since the early 1900s (Dubé and Gosselin, 2007) and an endowment of ca. 235 Moz (Monecke et al., 2017). Like other Archean greenstone belts, many deposit-types are present (Groves et al., 1998; Poulsen et al., 2000; Groves et al., 2003; Goldfarb et al., 2005; Robert et al., 2007; Dubé and Gosselin, 2007; Bateman et al., 2008) and a spatial correlation is recognized between the deposits and large-scale structures, of which the Porcupine-Destor (PDDZ) and Cadillac-Larder Lake (CLLDZ) deformation zones are the most prominent (Fig. 1A). These structures extend for 100s of km and are considered to be the surface expression of deep-rooted crustal breaks along which mineralizing fluids were channelled (e.g., Dubé and Gosselin, 2007; Bleeker, 2015).

At the deposit scale, much of the historically and currently mined gold in the AGB occurs in high-strain zones characterized by quartz-carbonate-sulphide veins or disseminated auriferous pyrite (e.g., Dubé and Gosselin, 2007; Lafrance, 2015a). However, locally there appears to be a connection, either passive or causal, between gold mineralization and alkaline intrusions (generally felsic to intermediate) contemporaneous with development of syn-orogenic basins early in the deformation history of the AGB (Robert, 2001; Kontak et al., 2008; Bleeker, 2015; Fayol and

Jébrak, 2017). Because of the prolonged deformation related to the PDDZ and CLLDZ, these intrusion-associated deposits (IAD) can be overprinted by later features that mask many of the original deposit features. Additionally, remobilization and/or a second mineralizing event can affect these deposits, as seen for example at the Wasamac (Mériaud and Jébrak, 2017) and Renabie (McDivitt et al., 2018) deposits. Furthermore, the features of both IADs and other types can differ due to the variable nature of their host rocks and depth of formation, which together produce a wide range of mineralization styles.

The Grey Fox and Hislop gold deposits are located about 80 km east of Timmins in northern Ontario (Fig. 1A, B). They represent IADs located south of the PDFZ and proximal to the orogenic Black Fox deposit. The results of detailed surface mapping and core relogging complemented by petrographic study, SEM-EDS analysis, whole-rock and mineral chemistry, and elemental mapping of pyrite using laser ablation inductively coupled plasma mass spectrometry (LA-ICP-MS) are presented here. These results are integrated into a deposit model, which is then compared to the adjacent, shear-hosted orogenic Black Fox deposit to highlight the contrasting nature of IAD and orogenic gold deposits.

2.2 GEOLOGIC SETTING

The southern AGB in the southeast Superior province is dominated by E-W striking mafic to felsic metavolcanic rocks and clastic metasedimentary rocks (Fig. 1). The metavolcanic rocks range in age from 2750 Ma to 2696 Ma (Ayer et al., 2005). They are ultramafic- to felsic in composition with tholeiitic- to calc-alkaline affinities, and record greenschist to amphibolite facies metamorphism. These volcanic sequences were deformed prior to deposition of two sedimentary assemblages: 1) the older Porcupine assemblage (ca. \leq 2690-2685 Ma), which is dominated by

turbiditic units consisting of well-bedded greywackes, siltstones, and mudstones; and 2) the younger Timiskaming assemblage (ca. ≤ 2676 -2670 Ma), which is dominated by alluvial and fluvial sedimentary rocks (ibid). Alkali magmatism was broadly coeval with Timiskaming sedimentation, both as volcanic flows and deeper-seated intrusions. Debate still exists whether the Timiskaming sedimentary rocks were deposited in restricted, pull-apart basins along transpressional faults (Ayer et al., 2005; Bateman et al., 2008) or in a larger extensional basin (Rowins et al., 1993; Bleeker, 2015). Later deformation and metamorphism at 2665-2655 Ma (Ayer et al., 2005) resulted in the formation of the PDFZ and overprinting of the Porcupine and Timiskaming assemblages and intrusions.

Gold mineralization in the region can be grouped into two general types: orogenic-style and intrusion-associated. The former is characterized by a strong spatial and temporal association with brittle-ductile compressional or transpressional shear zones (6-12 km depth; 300°–475°C; Goldfarb et al., 2005 and references therein). Ore zones are associated with laminated veins along steeply dipping faults and shallow-dipping extensional veins with variable enrichment in Ag-As +/- W, B, Te, Bi, Mo and Au:Ag ratios >5 (Robert et al., 2007). In these settings, the Au fluid is generally attributed to a metamorphic source (e.g., Ridley and Diamond, 2000; Cassidy and Hagemann, 2000). In contrast, IADs are attributed to intrusive activity, in particular during the formation of the Timiskaming basin (Robert, 2001), and are related to shallower epizonal depths of formation as suggested by the porphyritic texture of the intrusions (Robert et al., 2007). Ore zones form as disseminated-stockwork zones and/or in association with crustiform-style veins and are commonly enriched in Te, Sb, and Hg (Robert et al., 2007). The source of the fluid in these systems is poorly constrained and equivocal, but the two most likely scenarios are: 1) exsolved

magmatic fluids from the intrusions themselves; or 2) metamorphic devolatilization of the country rocks due to increased metamorphic gradient resulting from the magmatism (references above).

2.3 DEPOSIT GEOLOGY AND MINERALIZATION

The Grey Fox, Hislop, and Black Fox deposit settings are hosted by ca. 2710-2704 Ma felsic- to ultramafic metavolcanic rocks of the Tisdale assemblage and ca. \leq 2680 Ma metasedimentary rocks and felsic intrusions (generally alkalic) of the Timiskaming assemblage representing the youngest rock units (Figs. 1B and 2; Berger, 2002; Ayer et al., 2005). In the Timmins area, the metavolcanic rocks and Porcupine turbidites underwent two compressional deformation events (D₁ and D₂) prior to the deposition of the Timiskaming sedimentary rocks (Bateman et al., 2008; Dubé and Mercier-Langevin, 2020). In the study area, the first post-Timiskaming deformation (D₃) developed during south-over-north shearing related to a shortening event at 2665-2640 Ma, which at Black Fox is characterized by N-verging drag folds that fold lithologic contacts and an earlier foliation (Haugaard et al., 2021; Mitrofanov et al., 2018 Chappell, pers. comm.). The second post-Timiskaming event (D₄) is characterized by E-trending dextral shear zones and Z-shaped folds (Chappell, pers. comm.) and is consistent with the regional deformation event recognized in the belt (Bateman et al., 2008; Ayer et al., 2005; Robert, 2001).

Mineralization styles vary significantly among deposits. Whereas the Black Fox deposit is hosted by intensely sheared ultramafic metavolcanic rocks localized to the PDDZ, the Grey Fox deposit is hosted in a competent block of felsic- to mafic metavolcanic rocks enveloped by sheared ultramafic rocks (Fig. 2). In contrast, the Hislop deposit occurs along the contact between the competent block and the sheared ultramafics. Mineralization in the more competent rocks is characterized by brittle textures, such as breccia and/or crustiform quartz-carbonate vein that cut

relatively undeformed metavolcanic and metasedimentary rock, as noted at Grey Fox and the northern section of Hislop. Conversely, at Black Fox, massive quartz-carbonate veins are hosted by sheared ultramafic metavolcanic rocks.

The Grey Fox deposit (Fig. 2) contains an estimated indicated resource of 620,000 ounces of Au at a grade of 7.2 g/t and inferred resource of 133,000 oz of Au at a grade of 6.3 g/t (McEwen Mining, 2021a). Three main zones are defined by drilling (Fig. 3A): (1) the Contact Zone at the contact between metasedimentary and mafic metavolcanic rocks with Au mineralization in both units; (2) the 147 Zone hosted in intermediate metavolcanics characterized by abundant volcanic features (e.g., hyaloclastites, varioles); and (3) the South Zone hosted in felsic metavolcanic rocks with abundant spherulites, hyaloclastites, and in situ breccia from autobrecciation. In all zones, Au occurs as refractory gold in arsenian pyrite in altered host rocks and as visible gold in quartz-carbonate breccia and crustiform veins that cut the altered host rocks. Mineralization is truncated at depth by sheared ultramafic units and the crustiform veins are overprinted by the shear foliation.

The Hislop deposit (Fig. 2) has been in intermittent production from 1990 to 2015. (Rocque et al., 2016). It produced 160,000 oz of Au (ibid) and has current proven and probable reserves of 33,000 oz at a grade of 5.8 g/t, measured and indicated resources of 173,000 oz at a grade of 4.0 g/t, and inferred resources of 97,000 oz at a grade of 3.8 g/t (Kirkland Lake Gold, 2021). The deposit was mined initially as an underground mine and later as two open pit operations. Mineralization is focused in and around a syenitic intrusion at the contact between ultramafic metavolcanic rocks to the south and mafic and felsic metavolcanic rocks to the north. Gold is localized within an alteration halo that surrounds and is developed within the syenitic intrusion, as well as associated with quartz veining that cuts this earlier alteration. The latter is found in more

competent rocks, such as the felsic metavolcanics in the north wall (Fig. 3B) and the syenite intrusion itself.

The Black Fox deposit (Fig. 2; formerly the Glimmer mine) was previously mined as an open pit (1997 to 2001 and 2009 to 2015) with underground production beginning in 2011, which is nearing its end. As of 2020, it had produced 944,000 oz of Au (McEwen Mining, 2021b). At the end of 2020, it had a proven and probable reserve of 14,000 oz at 4.05 g/t and a measured and indicated resource of 84,000 oz at 5.28 g/t with 41,000 oz inferred at 5.32 g/t (McEwen Mining, 2021a). Gold mineralization is in massive quartz-carbonate fault-fill and extensional veins, which are localized in sheared and faulted carbonatized ultramafic (i.e., komatiitic) and basaltic metavolcanic rocks.

2.4 SAMPLING AND ANALYTICAL TECHNIQUES

2.4.1 Field work and sampling

Mapping of portions of the Hislop and Black Fox open pits was complemented at Black Fox with additional mapping of underground workings. At Grey Fox, 2,000 m of drill core from eleven holes that intersected the three ore zones were re-logged. This work aimed to define the relationships between lithology, alteration, structure, veining, and Au mineralization. Representative samples of least altered lithologies and alteration types were collected in addition to systematic sampling (1-5 m spacing) in parts of the Hislop open pit and Black Fox underground mines. A total of 376 samples were collected for follow-up work: 168 from Hislop, 51 from Black Fox and 157 from Grey Fox.

2.4.2 Petrography and SEM-EDS analysis

A subset of samples (104) were prepared as polished thin sections (30 μm) for transmitted and reflected light study using an Olympus BX-51 microscope. In addition, 58 of 104 samples were examined with a JEOL 6400 scanning electron microscope (SEM) coupled to an Oxford Sight energy dispersive spectrometer (EDS) in the Micro-Analytical Centre (MAC), Laurentian University, Sudbury, Canada. Semi-quantitative analyses were done in point and raster modes using an accelerating voltage of 20 kV, a 1.005 nA beam current, and a working distance of 15 mm. The photomicrographs presented are labelled using abbreviations of Whitney and Evans (2010) (Table 1).

2.4.3 Whole-rock lithochemistry

Three whole-rock lithochemical databases are included in this study. Two sets were provided by McEwen Mining for Grey Fox and were analyzed at AGAT laboratories, Mississauga, Canada; this material used typical core sample lengths of one metre. In the first dataset (n=181; 147 and South zones), material was prepared by lithium borate fusion and analyzed for major and minor elements by XRF and trace elements by LA-ICP-MS. In addition, carbon was analyzed by LECO combustion and Au as metallic Au-ICP after fire assay. In the second dataset (n=10,827; all three ore zones), the material was analyzed for Au and metal concentrations by ICP-OES after fire assay and *aqua regia* digestion, respectively. The third dataset (n=31) consists of field samples from the Hislop and Black Fox deposits and 10-20 cm core intervals from the Grey Fox deposit. Weathered surfaces and veins were removed, and the samples were sent for analysis to ALS laboratories in Vancouver, Canada. Major and minor elements were analyzed by ICP-AES after a lithium borate fusion. Trace elements were analyzed by both ICP-MS after a lithium borate fusion

with acid digestion and quadrupole ICP-MS after four-acid digestion. Concentrations of ferrous iron were determined by titration, total carbon by a LECO furnace, and Au by ICP-AES after fire assay.

2.4.4 Laser ablation mapping of pyrite

Four pyrite grains from Au-bearing zones in the studied deposits were used for LA-ICP-MS elemental mapping to assess chemical zoning and quantify elemental abundances; these include two grains from the Grey Fox deposit (from the 147 and Contact zones), and one each from the Hislop and Black Fox deposits. Analysis done at the Geochemical Fingerprinting Laboratory at Laurentian University used the protocol of Gourcerol et al. (2018a). Ablation was done with a Renoetics Resolution M-50 laser and the ionized material was analyzed with a Thermo X-Series II quadrupole ICP-MS for Fe, Al, Ti, Co, Ni, Cu, Zn, As, Se, Mo, Pd, Ag, Cd, In, Sn, Sb, Te, W, Pt, Au, Pb, and Bi. The data were used to generate 2D elemental distribution maps and the line traverse data was converted into time-slice domain data (Gourcerol et al., 2018a) and plotted on binary diagrams to examine elemental relationships.

2.4.5 Zircon separation for geochronology

Zircon separation was attempted for the syenite intrusive unit from the Hislop open pit to be used for geochronology, but two attempts at heavy mineral separation using a Wilfley table followed by heavy liquids (methylene iodide) did not yield any zircon.

2.5 PETROLOGICAL CHARACTERIZATION OF ORE HOSTING UNITS

The ore hosting units are altered to varying degrees, which obscures the protolith identity. The problem is compounded by many of the units having a similar green color due to greenschist and/or

amphibolite grade metamorphism. To determine the protolith, detailed petrography, together with whole-rock lithochemistry, was used to identify precursors.

2.5.1 *Metavolcanic units*

Due to the presence of variable alteration in these samples, immobile trace elements are used to discriminate protoliths (Fig. 4A) and identify magmatic affinity, which is uniformly tholeiitic (Fig. 4B). The abundance and patterns of the rare earth elements (REE) are similar to those of various Tisdale Group metavolcanic rocks, as established by Diné et al. (2008) (Fig. 4C), with distinctly lower values for ultramafic metavolcanic rocks. Despite being altered, these samples display similar tholeiitic trends with Fe-enrichment followed by a decrease in Fe and Mg in the felsic units (Fig. 4D). Additionally, as the major- and trace-element chemistry of the mafic- and felsic metavolcanic samples at Hislop and Grey Fox are similar, they are discussed together below.

Ultramafic metavolcanic rocks are the most deformed units in all three deposit areas (Fig. 5A) and form two distinct subgroups: 1) talc-carbonate altered (grey); and 2) chlorite-carbonate altered (black), which is variably altered to fuchsite-carbonate (green). The major, minor, and select trace element data that help to compare these ultramafic units are provided in Table 2. The talc-carbonate rocks are only observed at the Black Fox deposit and are rarely auriferous. In contrast, the chlorite-carbonate rocks are in all three deposit areas and are host to Au at Hislop and Black Fox, with the fuchsite-carbonate also present and mineralized at the latter. Both rock types are massive or strongly sheared (Fig. 5A) with no volcanic textures preserved, although spinifex is reported in the area (Troop, 1989).

The least altered *mafic metavolcanic rocks* form massive and pillowed flows (Fig. 5B). The least altered samples consist of amphibole and plagioclase (An₄₀₋₆₅), with minor leucoxene and magnetite. The SiO₂ content ranges from 40-55 wt. %, Fe₂O_{3(tot)} from 8-15 wt. %, and MgO from 3.5-7 wt. %. Samples plot in the basalt field on all chemical discrimination diagrams (Fig. 4A, B, C).

Intermediate metavolcanic flows are typically aphanitic and strongly altered. They contain flow-top facies features, including hyaloclastite fragments (Fig. 5C), varioles (<0.5 cm: Fig. 5D), amygdules, and breccias. The more massive, least altered interiors of the flows consist of amphibole, plagioclase (An₄₅₋₆₅), magnetite, and ilmenite. In flow-tops, the interiors of fragments are least altered and contain chlorite, albite with rare residual plagioclase, quartz, titanite, and apatite, with the margins being variably altered to albite or muscovite with complete loss of chlorite; quartz commonly lines fractures between fragments. The varioles consist of radial linear inclusions defined by small (<10 µm) individual mafic grains (chlorite or amphibole in least altered) surrounded by feldspar +/- quartz (Fig. 5E); as the term variole is a field term and as these are texturally similar to the spherulites described below in the felsic metavolcanics, for the rest of the thesis these will be referred to as spherulites instead of varioles. Overall, these rocks have a similar major-element chemistry as the mafic metavolcanics, with slightly higher SiO₂ (40-58 wt. %) and Fe₂O_{3(tot)} (8-18 wt. %) but lower MgO (1-4 wt. %). The best discriminatory element for the intermediate units is P₂O₅, as it is higher compared to all other metavolcanic rocks - 0.3-0.75 wt. % versus <0.2 wt. %. They are also easily discriminated using their Zr/Ti versus Nb/Y values (Fig. 4A), forming a distinct cluster along the boundary between basalt and andesitic basalt, and using a Jensen Cation Plot (Fig. 4D), where they cluster at the peak of the trend with the highest

Ti+Fe enrichment. Additionally, on a chondrite-normalized REE plot (Fig. 4C), their concentrations fall within the intermediate tholeiite field as defined by Dinel et al. (2008).

Like the other metavolcanic rocks, the *felsic metavolcanics* are aphanitic, spherulitic (< 2-5 cm: Fig. 5F), amygdular (Fig. 5G), hyaloclastic, and brecciated. Their modal mineralogy is dominated by feldspars and quartz with lesser mafic minerals (clinopyroxene and chlorite) than the other units. This unit also contains a blue, iridescent mineral in small quantities thought to be an alkali-amphibole based on petrography and semi-quantitative analysis. Spherulites are typically larger than in intermediate rocks (≤ 5 cm; Fig. 5F) and commonly coalesced together forming massive sections (Fig. 5G). Like previously described for the intermediate units, they are defined on the micro-scale by radiating branches of mafic grains (possibly clinopyroxene or amphibole altered to chlorite) that persist through subsequent alteration (Fig. 5H, I). The immobile trace element compositions of these rocks are similar at both deposits (Fig. 4) and indicate a dacitic to rhyolitic protolith, which is reflected in their major chemistry by higher SiO₂ (60-70 wt. %) and lower Fe₂O_{3(tot)} (5-12 wt. %) and MgO (<2 wt. %) relative to the intermediate metavolcanic rocks.

2.5.2 Tuffaceous metasedimentary rocks

The least altered metasedimentary rock units observed at the Grey Fox and Black Fox deposits are massive with local bedding-parallel foliation present that is enhanced by alteration (Fig. 6A). The beds are composed of very fine-grained albite (95+%) and minor quartz and as such are thought to represent a tuffaceous protolith. Minor pyrite is present and is either elongate and parallel to the foliation or equant.

2.5.3 *Felsic-intermediate intrusions*

Felsic to intermediate intrusions occur in all the deposits, but have the strongest association with mineralization at Hislop, where the mineralization is centered in and around a purple, porphyritic felsic intrusion, with additional thinner, brick-red to pink, phaneritic intrusions in the north wall of the pit (Fig. 6B,C,D,E). A third intrusion is also observed in the south wall of the Hislop pit but was not accessible due to ground conditions (Fig. 6E). As production at Hislop terminated before this study began and much of the intrusions were difficult to access or inaccessible, the results presented here rely on data and observations presented in Van Lichtenvelde (2002), complemented with samples from the McEwan geochemical database, and select samples taken as part of this study in the Hislop and Black Fox open pits. Three groups of felsic to intermediate intrusions are identified through their general mineralogy and geochemistry and naming here correspond to that suggested by Van Lichtenvelde (2002): 1) syenites, 2) melanosyenites, and 3) quartz-feldspar porphyries (QFP). Discrimination diagrams based on geochemistry and calculated normative mineralogy are presented in Figure 7. Principal normative minerals, LOI, C, Au, and SiO₂ are listed in Table 3.

The *syenites* are pink to purple to red, with porphyritic and phaneritic varieties comprising K-feldspar and plagioclase phenocrysts. During mapping of the Hislop pit in 2015/2016, two texturally distinct units were encountered: 1) a purple, coarse-grained, heavily altered porphyritic unit with K-feldspar phenocrysts and a sericitized matrix that was at the centre of the deposit (Syenite I; Fig. 6B,C); and 2) a pink-red, fine- to medium-grained phaneritic unit comprising K-feldspar (Or₁₀₀) and plagioclase (Ab₁₀₀), which was found as thinner dykes within the metavolcanics to the north of Syenite I and was considerably less altered (Syenite II; Fig. 6D).

The *melanosyenites*, not studied in detail here, are described as dark, brick red or purple on fresh surfaces, fine-grained to coarse-grained intrusions composed of altered feldspars (K-feldspar and plagioclase) and chlorite after biotite (ibid).

The *QFPs* are light grey to dark grey at Hislop and pink at Black Fox. They are porphyritic with plagioclase phenocrysts and a fine-grained matrix of plagioclase and quartz.

The *mineralized syenites* at Hislop, as described by Van Lichtervelde (2002), are light pink to grey in color, fine-grained, and strongly altered. In the geochemical discrimination diagrams (Fig. 7), this group is pulled out as a separate unit, as is the syenite clast collected from within the ultramafic metavolcanics, to assess relative to the less altered units. Additionally, two strongly altered and pyrite-rich felsic intrusions collected from the Black Fox that were sent for whole-rock geochemistry are also plotted separately. One is grey and fine-grained and the other is light red and medium to coarse-grained, however, detailed petrography was not completed.

2.5.4 *Lamprophyre dikes*

K-rich mafic intrusive rocks at the Hislop and Grey Fox deposits are interpreted as lamprophyres (LAM). Their description is from Van Lichtervelde (2002) as is their geochemistry, which is presented in Figure 8. The LAMs are brown to dark green, fine-grained, and altered; as such the mineralogy is difficult to determine but consists predominantly of biotite, chlorite, and calcite with rare feldspars. Like the syenites, these units are host to mineralization at Hislop, and a mineralized syenite xenolith was also observed within a LAM intrusion (ibid). Finally, these intrusions record strong deformation fabrics. Relative to the felsic intrusions, they have lower Zr/Ti ratios (Fig. 8A,B), lower SiO₂ concentrations (Fig. 8A,C), but still high alkali content relative to

silica (Fig. 8C). Their REE profiles show a similar slope to the syenite intrusions, with abundances similar to the melanosyenites but slightly increased (Fig. 8D).

2.6 MINERALOGY AND DISTRIBUTION OF ALTERATION TYPES

Summarized below are the various types of alteration at the Grey Fox and Hislop deposits and their relationship to gold mineralization. For Black Fox, observations presented in the technical report (Brisson, 2014) are also included.

2.6.1 *Grey Fox*

The alteration assemblages in the different zones are similar and thus are described together. Early chlorite-albite-quartz and sodic-carbonate alteration overprint greenschist to amphibolite-facies metamorphosed rocks, which are collectively cut by a muscovite-chlorite alteration. In addition, two vein-related alteration types are present: 1) K-feldspar, where quartz-carbonate veins cut the metamorphosed rocks; and 2) decarbonatization, which overprints the disseminated carbonate-albite alteration. A summary of the mineralogy of each alteration type for the three zones is presented in Table 4. In the Contact zone, alteration and mineralization are present along the contact between mafic metavolcanic rocks to the east and metasedimentary rocks to the west, with the sodic-carbonate alteration being replaced by the muscovite-chlorite alteration at the contact between the two units (Fig. 9). In the 147 and South zones, a similar zoned alteration is observed, however the spatial distribution is more erratic and fracturing of the host rocks has a stronger control on its distribution.

2.6.1.1 Alteration Type 1: chlorite-albite-quartz

The earliest alteration results in a green to dark green color in hand sample that is similar and indistinguishable from the metamorphosed host rocks (predominantly plagioclase and amphibole). This alteration partially to completely replaces metamorphic mineral assemblages, but primary textures are locally still preserved (Fig. 10A versus B). It is dominated by chlorite (intermediate and mafic metavolcanic rocks), albite (sediments and felsic metavolcanic rocks), and quartz, with minor to trace calcite, rutile, magnetite, and apatite +/- titanite in the intermediate metavolcanics +/- bastnäesite in the felsic units (Fig. 10).

2.6.1.2 Alteration Type 2: sodic-carbonate

This alteration is characterized by carbonate (dolomite-ankerite) and albite +/- quartz (Fig. 11), with minor to trace amounts of magnetite, rutile, and pyrite. It renders the rock whitish where carbonate is abundant and purplish where albite (+/- quartz) dominates. The modal abundance of each mineral is host rock dependent, with carbonate as a minor component in the felsic metavolcanic rocks and as a major component in intermediate and mafic metavolcanic rocks. The alteration is generally patchy but is more pervasive and widespread closer to the contact between the metavolcanic and metasedimentary rocks and where veins occur.

2.6.1.3 Alteration Type 3: muscovite-chlorite – gold-bearing

This alteration cuts across all previously described alteration types. It is pervasive in areas with strong Au-mineralization (e.g., mafic metavolcanic-metasedimentary contact) but also is commonly present throughout the deposit area as narrow (<1 mm), fracture-controlled alteration. This alteration varies from: 1) a muscovite-dominant (Fig. 12A, E, F, G, H), white to beige

alteration visually similar to the sodic-carbonate alteration; to a 2) chlorite-dominant (Fig. 12B), dark green alteration visually similar to the background metamorphic and chlorite-albite-quartz alterations. This Type 3 chlorite is more Fe-rich (see below) than chlorites in other alteration zones and is more pronounced in the Contact Zone. Muscovite and/or chlorite replace older metamorphic and alteration albite and carbonate (Fig. 12A), with the latter becoming more Fe-rich (see below) with siderite being present in the South Zone. Additional major phases present are quartz and hematite and/or pyrite (auriferous) where alteration is more pervasive, with minor apatite and rutile and trace amounts of barite, monazite, xenotime, cobaltite, galena, molybdenite, sphalerite, arsenopyrite, pyrrhotite, scheelite, allosclerite (or glaucodot, an As-Co sulphide), and native gold. Hematite in this alteration type is present in greater abundance than magnetite in the lesser altered rocks.

2.6.1.4 Alteration Type 4a: K-feldspar – gold-bearing

The K-feldspar alteration is more localized than the other alteration types and is mainly present in fragments of wall rock hosted by auriferous veins. More rarely they are observed as reddish alteration around veins that cut relatively unaltered rocks (i.e., chlorite-albite-quartz alteration; Fig. 13A). It is dominated by K-feldspar (Or₁₀₀) and quartz with minor to moderate auriferous pyrite, minor calcite, rutile, and apatite and trace galena, scheelite, molybdenite, sphalerite, xenotime, and native gold (Fig. 13B). K-feldspar is also present as inclusions in auriferous pyrite.

2.6.1.5 Alteration Type 4b: decarbonatization – gold-bearing

Decarbonatization is observed at the 147 and South zones where quartz-carbonate veins cut sodic-carbonate altered rocks lacking muscovite-chlorite alteration. In such cases, a purple-red

halo around these veins is characterized by an almost complete loss of carbonate (Fig. 13C, D), and a coarsening of rutile. The halos are dominated by albite, quartz, and auriferous pyrite with minor rutile, xenotime, and monazite.

2.6.2 *Hislop*

Several alteration types are observed at Hislop: 1) early potassic alteration (i.e., muscovite, K-feldspar) that occurs around and within the central Syenite I intrusion (Fig. 6E); 2) sodic-carbonate alteration that is centered on quartz-carbonate veins that occur preferentially in the Syenite I and the felsic metavolcanic rocks to the north of it; and 3) a relatively late-stage talc alteration in the ultramafic rocks south of Syenite I associated with the shearing. In addition, late-stage epidote fills fractures that cut the mafic metavolcanic units. The alteration assemblages, as well as the interpreted protolith mineralogy, are summarized in Table 5.

2.6.2.1 *Alteration Type 1: potassic (intrusion-halo) – gold-bearing*

This alteration is pervasive within all rock types, but its mineralogy depends on the host rock. It is expressed by K-feldspar in felsic (Fig. 14A) and ultramafic (Fig. 14B) metavolcanic rocks and muscovite in the mafic metavolcanic rocks (Fig. 14C) and the main Syenite I (Fig. 14D).

The least altered felsic metavolcanic rocks have a distinctive red color and are dominated by K-feldspar, albite, and clinopyroxene (Fig. 14A), with minor Ti bearing hematite (<2 at. %), apatite, titanite, calcite, biotite, alkali-amphibole, and magnetite with variable muscovite and chlorite (<5% each). Magnetite and biotite occur where hematite, K-feldspar or clinopyroxene are absent, but such zones were not pervasive.

Potassic alteration is the only alteration present in the mafic metavolcanic rocks, where it is expressed by amphibole and muscovite (with minor residual plagioclase), as well as minor disseminated leucoxene (magnetite, ilmenite, titanite) (Fig. 14B) and trace apatite. This assemblage is cut by fractures and calcite veinlets with K-feldspar selvages and halos (1-2 mm).

The matrix of the porphyritic syenite (Syenite I) at the centre of the Hislop deposit is nearly completely altered to muscovite (Fig. 14C), where it contains anomalous gold values (~0.116 ppm Au). The mineralized syenites described by Van Lichtervelde (2002) are associated with a carbonate-muscovite alteration. Syenite II is less altered, red in colour due to hematite, and has variable K₂O contents (9.21 wt.% versus 5.80 wt.%) and similarly anomalous gold values (0.16 ppm and 0.14 ppm, respectively).

In the ultramafic rocks, alteration is progressive with a change in color from medium- to dark grey (distal; >5 m from syenite), to beige-tan (proximal; <5 m from syenite; Fig. 6E), and finally a pale green with pink specks (adjacent; <1 m from syenite). In distal samples, the rock consists of carbonate, albite, and talc with minor magnetite, whereas adjacent to Syenite I, K-feldspar dominates with minor carbonate in the rock matrix and veins (Fig. 14D). A fracture-controlled fuchsite alteration cuts the veining near the syenite but is not well constrained in this study.

2.6.2.2 *Alteration Type 2: sodic-carbonate (vein-halo) – gold-bearing*

This alteration overprints the potassic alteration and is present as halos around quartz-carbonate veins that cut through the felsic metavolcanic rocks and Syenite I at the centre of the deposit. In the felsic metavolcanic rocks, a progressive alteration halo surrounds the quartz-carbonate veins. The outer zone (<1 m away from veins) is indistinguishable from the surrounding

potassic altered rocks, but K-feldspar is almost completely replaced by albite. Moderate quartz, Ti-bearing hematite, chlorite, and carbonate (early coarse euhedral calcite and later anhedral dolomite) are also present with minor/trace rutile, apatite, and talc (Fig. 15A). Adjacent to the veins (e.g., 0.5 to 10 cm), the wall rock is bleached and rusted with abundant pyrite present and a loss of hematite. It is still dominated by albite, but carbonate and quartz are more abundant relative to the outer zone; (Fig. 15B). Minor phases include rutile, apatite, chlorite, and trace amounts of monazite, xenotime, sphalerite, and tellurides (petzite and a Pb-Te+/-Ag phase) are present. Late chloritic seams are also present with abundant pyrite, which cut the veined parts of the rock.

In Syenite I, a similar halo-style sodic alteration is present but without gold mineralization. The buff to beige alteration overprints the host rock textures and is similar to that observed in the felsic metavolcanic rocks. The sericitized matrix of the syenite is altered to albite +/- quartz with minor carbonate and pyrite (Fig. 15C). Although not shown, primary K-feldspar megacrysts are preserved.

2.6.2.3 *Alteration Type 3: talc (deformation-related)*

In the ultramafic metavolcanic rocks, two alteration types are present distal to the potassic alteration. They are defined by an early chlorite alteration that is cut by a strongly foliated talc alteration. The latter increases in abundance away from the syenite contact, with little to no chlorite present distally (>5 m from the contact with Syenite 1). From Van Lichtenvelde (2002), a clast of syenite is present within this sheared talc-chlorite unit, suggesting that the deformation is late and postdates the emplacement of Syenite I.

2.6.2.4 *Epidote-chlorite-albite (late fracture-filling)*

A late set of epidote veinlets contain previously altered K-feldspar altered fragments. They are surrounded of alteration halos of chlorite and albite after amphibole and muscovite. These veins were only observed in the mafic metavolcanic rocks in the Hislop pit. A similar style of epidote veining is found in the late diabase dikes in the area that cut mineralization.

2.6.3 *Black Fox*

Samples collected from the open pit and underground workings in this study generally did not return highly anomalous Au values. Thus, here we summarize observations from technical reports on the Black Fox deposit, with additional detail on the development of fuchsite alteration in the ultramafic metavolcanic rocks as it is a common alteration present in ultramafic-hosted orogenic gold settings in the AGB (Ispolatov et al., 2008; Lafrance, 2015b) and was studied more in depth as part of this study. Figure 16A shows the relationship of the ultramafic metavolcanics in the Black Fox open pit.

As noted earlier, the ultramafic metavolcanic rocks are subdivided into two types based on chemistry and mineralogy, with two alteration assemblages in the second type: 1) talc-carbonate altered (grey), which contains little chromite (Fig. 16B); 2) and chlorite-dolomite-albite altered (black) with more abundant chromite (Fig. 16C), and which is variably altered to fuchsite-chlorite-albite-dolomite (green; Fig. 16D). In general, type 2 is host to most of the gold mineralization with veining and associated mineralization present in both alteration packages. Conversely, Au-mineralization in type 1 is much less common but when present is associated with quartz veinlets (Rhys, 2016). In the fuchsite-bearing unit, the fuchsite and chlorite are relatively late and cut the earlier assemblages (Fig. 16DII, DIII). In addition to the dominant mineral assemblage, a Ba-

bearing muscovite (not shown) was identified in fuchsite-altered rocks at the contact of a mineralized felsic intrusive. Other rock units hosting mineralization include mafic metavolcanics and felsic dykes, both of which have a gold-associated alteration zone of albite-carbonate-muscovite-pyrite and gold-bearing quartz-carbonate veins (Mitrofanov et al., 2018).

2.7 RELATIONSHIP OF GOLD MINERALIZATION TO VEINING

Veins at the Grey Fox and Hislop deposits differ markedly from those at the Black Fox deposit. In addition to having different textures and orientations, they also differ in setting of formation with the Grey Fox and Hislop veins being relatively undeformed compared to the Black Fox veins, which are strongly folded.

2.7.1 Grey Fox and Hislop vein systems and associated gold mineralization

In both the Grey Fox and Hislop deposits, there are strong associations between veining and gold mineralization with two dominant styles present: 1) invisible or refractory gold in pyrite within alteration halos of the veins; and 2) as visible gold in veins. At Grey Fox, vein-related alteration is predominantly K-feldspar, decarbonatization, and muscovite-chlorite, whereas at Hislop it is albite and carbonate, although K-feldspar alteration around the syenite is also auriferous (Rocque et al., 2016). Visible gold is present only at Grey Fox, where it is encountered in all zones but most abundant in the 147 Zone.

Veins at Grey Fox preferentially occur in intermediate (147 Zone) and felsic (South Zone) metavolcanic rocks, as well as at the contact between the mafic metavolcanic rocks and sedimentary rocks (Contact Zone). They have two principal orientations, $222^{\circ}/55^{\circ}$ NW and $046^{\circ}/65^{\circ}$ SE, that can change slightly in different host rocks (Chappell, pers. comm.) (Fig. 17A).

Where vein sets intersect, the veins are brecciated and alteration and mineralization are enhanced. Veins at Hislop have similar orientations (red in Fig. 17A) and are mutually cross-cutting (Fig. 17B). Like Grey Fox, the veins preferentially occur in more competent rocks, which at Hislop are represented by the felsic metavolcanic rocks and the syenite intrusion.

The Grey Fox veins are subdivided based on mineral composition, cross-cutting relationships, and by their crustiform (Fig. 18A, B) and brecciated (Fig. 18C-E) textures. Three distinct vein stages are observed. Early comb-textured quartz contains visible gold and is either clear to slightly white or dark grey to black due to the presence of fine-grained disseminated molybdenite (Fig. 18A, C, E). This quartz lines crustiform veins (Fig. 18A, B), cements brecciated veins and wall rock (Fig. 18C, D), and also occurs as veins overprinting all other vein types (Fig. 18E). Coarse, strongly zoned carbonate minerals, with alternating Mg- and Fe-rich growth zones (Fig. 18B; inset), overgrows the comb quartz in crustiform veins and is gold-barren. A fine-grained intergrowth of quartz and carbonate can overgrow the previous stages (Fig. 18A, B) or cement breccias (Fig. 18C, E) but is typically gold-barren. At depth, these veins are deformed together with the ultramafic metavolcanics (Fig. 18F).

The gold-associated veins at Hislop are quartz rich with minor carbonate (dolomite-ankerite). They occur either as narrow, linear veins (Fig. 19A, B), or as breccia veins with fragments of the host rock (Fig. 19C). They generally lack crustiform textures.

At both deposits, veins cut all the alteration types, although at Grey Fox veins are also cut by fracture-controlled muscovite-chlorite alteration. As different relationships with alteration are seen at deposits, these are described separately below.

Grey Fox deposit: Alteration halos are sometimes seen around the veins but are narrow (<2 cm) and have variable mineral assemblages. In muscovite altered zones, veins generally lack visible haloes, whereas in the carbonate-albite altered zones the decarbonatization adjacent to the veins results in an albite-quartz-rutile assemblage (Fig. 13C, D). Where veins cut chlorite-albite-quartz alteration, as observed in the 147 Zone (Fig. 13A), a progressive alteration is seen. First a thin (<0.2 mm) zone of hematite-muscovite with minor calcite occurs that overprints the chlorite-albite-quartz assemblage. This grades into K-feldspar alteration with increased calcite and abundant auriferous pyrite (Fig. 13A, B); chlorite is also present throughout but decreases in the hematite-muscovite zone before increasing towards the vein. In other zones, where veining also cuts the chlorite-albite-quartz material, a carbonate-albite, then albite-quartz-rutile alteration occurs around veins and in the vein fragments (Fig. 18D), with intense pyrite associated with the albite-rich alteration.

Hislop deposit: Veins have intense, bleached, and rusted albite-quartz-carbonate alteration halos (≤ 0.5 m; Fig. 19) with abundant pyrite close to the veins. These veins and related alteration cut and overprint the earlier, K-feldspar alteration that surrounds the syenite that is at the core of the deposit and also contains gold (Rocque et al., 2016).

2.7.2 *Veining and associated gold mineralization at the Black Fox deposit*

Veins at Black Fox are massive and composed of quartz and carbonate, generally with a mottled texture and variably recrystallized (Chappell pers. comm.). They preferentially occur in carbonate-chlorite altered ultramafic rocks as fault-fill (Fig. 20A) and *en echelon* veins forming complex vein arrays (Fig. 20B) with mutually cross-cutting relationships. Smaller, cm-scale, barren *en echelon* veins cut the mineralized veins. The fault-fill veins are up to 2 m in width,

generally strike east to southeast (100° - 170°) and have shallow to moderate dips (30° - 60°). Both vein types are oblique to and cut across an earlier foliation, which is also present in wall rock fragments contained within the laminated fault-fill veins. The veins are also folded by drag folds (Fig. 20A) and boudinaged and transposed parallel to the associated foliation (Chappell pers. comm.). This suggests that they were emplaced early during this folding event, which is interpreted to be part of the first post-Timiskaming compressional deformation (Haugaard et al., 2021; Mitrofanov et al., 2018).

Gold is found within, and associated with, both fault-fill and *en echelon* veins, where it is concentrated along the vein walls and on chlorite slip surfaces (Fig. 20C). Additionally, gold occurs in association with pyrite in altered mafic metavolcanic rocks and strongly albite-altered intrusions (Brisson, 2014).

2.8 MICRO-SCALE CHEMISTRY OF ALTERATION AND MINERAL PHASES

Semi-quantitative SEM-EDS data were collected to assess the chemistry of alteration minerals phases (e.g., chlorite, carbonate) in different alteration zones in addition to raster-type analysis. The data are discussed separately below.

2.8.1 Raster analysis

The mafic metavolcanic rocks from the Grey Fox Contact Zone were chosen for raster analysis at the micro-scale for three reasons: (1) the unit is fine-grained and relatively homogeneous at this scale, which is not the case for the flow-top metavolcanics of the 147 and South zones; (2) as the alteration is focused at the contact between mafic metavolcanic and metasedimentary rocks, its progression and overprinting relationships are easy to document; and

(3) least altered samples representing the starting material was identified. Eight samples were analyzed with results summarized in Figure 21. As $Fe/(Fe+Mg)$ or $Fe\#$, as atomic proportions, varied systematically with alteration (Fig. 21A, B), this ratio is plotted on the x-axis to monitor how the major elements vary with each alteration stage (Fig. 21C-I). Areas with abundant hematite and pyrite were avoided since this would “spike” the analysis with respect to Fe.

The chlorite-albite-quartz (Type 1) alteration is relatively isochemical, with only minor loss of Mg and Na noted; the apparent loss in Ca (Fig. 21G) resulted from the plucking of calcite during thin section preparation. The sodic-carbonate alteration (Type 2) is characterized by loss of Mg, Fe, and Si and gain of Na and K, with the latter attributed to the presence of fracture-controlled muscovite-chlorite alteration. The data for the muscovite±chlorite alteration (Type 3) plot as a continuum and show almost a complete loss of Na, progressive loss of Mg, Ca, Si and Al, and variable gain for Fe and K that depends specifically on the abundance of the phase present (i.e., chlorite versus muscovite).

2.8.2 Chlorite, carbonate, and pyrite chemistry

Chlorite chemistry varies systematically with the alteration at Grey Fox but is more ambiguous at Hislop. Trends are seen in terms of $Fe\#$ and Mg-Al-Fe (at. %) (Fig. 22), but as there is significant overlap in the sodic-carbonate and muscovite-chlorite alteration at Grey Fox, this may have affected the results. Additionally, a sample containing vein halo K-feldspar alteration overprinting the chlorite-albite-quartz alteration in the 147 Zone is plotted separately as 147 Zone (II). For Hislop, two auriferous samples are included and are color coded separately (i.e., in darker blue).

At Grey Fox, as the alteration progresses from chlorite-albite-quartz to sodic-carbonate to muscovite- and/or chlorite, there is a continual increase in the Fe# of the chlorite for the Contact and 147 Zones with near constant Al. One exception to this is found in the sample analyzed from the 147 Zone where the potassic vein-halo alteration overprints the chlorite-albite-quartz alteration assemblage but the chlorite chemistry did not show consistent Fe-enrichment. In the South zone, the chlorite chemistries from all the alteration zones overlap in Mg, Al and Fe composition but are uniformly Fe-rich. For Hislop, little chlorite occurs in the least altered sample, but the Fe content is elevated in the more altered, gold-bearing samples adjacent to veins compared to distal samples with sodic-carbonate alteration.

Like chlorite, carbonate also exhibits variable and systematic changes in its chemistry, again reflecting an increase in the Fe# with increasing alteration intensity (Fig. 23). This, however, is not as discriminatory as the chlorite signature due to the larger compositional ranges in individual samples and the smaller overall range in the data from all samples.

Vein carbonate typically shows alternating Fe- and Mg-rich zonation within single crystals (Fig. 23B, C) that span the overall range for Fe# noted for carbonate in host rock alteration and these are shown separately in Fig. 23D. Furthermore, where late fractures related to the muscovite-chlorite alteration cut the carbonate, the Fe# increases (Fig. 23D).

Pyrite in auriferous samples from all three zones at Grey Fox display oscillatory zoning, as seen in back-scattered electron images (Fig. 24A). This is due to variable As enrichment of up to 4 at. % in the pyrite (Fig. 24B) and As ↔ S substitution with the darker bands being enriched in As compared to the lighter bands. In contrast, Fe shows two apparent trends in a Fe versus As plot (Fig. 24C) with Fe content uniform at <2 at. % As and then decreasing as As concentration increases.

2.9 METAL ASSOCIATIONS

2.9.1 *Mass balance calculations*

The Grant (1986) isocon method is used to determine elemental changes in all alteration types. The results are presented in Figures 25, 26, and 27. Mafic metavolcanic rocks from the Contact zone were chosen to assess elemental changes at Grey Fox, and at Hislop, ultramafic samples were chosen to assess elemental changes related to the K-feldspar alteration (Fig. 26) and felsic metavolcanic rocks were used to assess elemental changes related to the sodic-carbonate vein-style alteration (Fig. 27). A summary of the change in metal concentrations for all alteration assemblages is presented in Table 6.

At Grey Fox, isocons are near unity indicating that only minor mass change (<10%) occurred (Fig. 25A, B). For the sodic-carbonate + muscovite-rich alteration, there are significant gains in C, S, Na₂O (effect of albite) and K₂O (effect of muscovite) with losses of SiO₂, CaO, Fe₂O_{3(tot)} and MgO. In contrast, the chlorite-rich alteration shows gains in Fe₂O_{3(tot)}, MgO, and S, losses in C, Na₂O, SiO₂, and CaO, and minor losses in K₂O. For trace elements, there were significant additions of Au, As, Mo, W, U and Pb during the muscovite-chlorite alteration, with Au increasing in abundance with muscovite (Fig. 25A). For the other elements, enrichment and depletion are variable, with the muscovite-rich alteration showing gains in Rb, Cs, Li and Sb, and the chlorite-rich alteration showing gains in Zn, Sn, Li and the LREE. The enrichment of the LREE was also noted by Gelinás (2012).

At the Hislop deposit, the potassic alteration shows gains in the major elements K₂O, S, CaO, C, LOI, and losses in Na₂O (Fig. 26), with this signature being more pronounced in the stronger potassic alteration proximal to the syenite (Fig. 26B). Similarly, the largest gain in metals

(As, W, Au, Pb, Sn, Ag, Mo, Sb, Bi) and some trace elements (e.g., Sr, Rb, Li, Cs, LREE) are also associated with this stronger alteration (Fig. 26B).

The distal sample of the sodic-carbonate alteration at Hislop shows large losses in K₂O, FeO and S, similar SiO₂, and increases in C, LOI, CaO and Na₂O (Fig. 27A), whereas the vein-proximal sample shows the inverse except for gains in LOI and SiO₂ (Fig. 27B). Gains in Au, Ag, Mo, As, Pb, Bi, W and Cu occurred in the more altered samples, with only significant gains in Mo, Sb and As occurring in the less altered samples.

2.9.2 Grey Fox whole-rock metal associations

A whole-rock lithogeochemical database of 10,827 analyses of variably altered and mineralized rocks for the Grey Fox deposit provides the means to evaluate metal content and associations related to mineralization; results are shown in the box and whisker (Fig. 28A) and binary element (Fig. 28B) plots. The box plots show that samples with elevated Au have elevated abundances for other metals as well (S, As, Mo, Ag, Pb, W), which is also reflected in the binary plots. In these plots (Fig. 28B), As, Mo and Ag, and to a lesser extent S, show similar flat trends with increasing Au until about 0.1 pm Au, after which a stronger correlation between these elements and Au are observed. This correlates with an increase abundance of pyrite and gold in ore zones, suggesting that these elements are tied up in the pyrite.

2.9.3 Element distribution maps of pyrites

Element distribution maps of pyrite generated by LA ICP-MS were completed for Grey Fox (2 grains), Hislop (1 grain) and Black Fox (1 grain). For Grey Fox, the pyrite grains are from chlorite-muscovite altered mafic metavolcanics (Fig. 29) and muscovite altered intermediate

metavolcanics (Fig. 30) of the Contact and 147 zones, respectively. For the Hislop deposit, the chosen pyrite grain is from a sodic-carbonate alteration halo to a quartz vein in felsic metavolcanic rocks (Fig. 31). For the Black Fox deposit, the grain is from an albite and pyrite altered felsic intrusion (Fig. 32).

2.9.3.1 Element maps for pyrite

Pyrite grains from Grey Fox (Figs. 29 and 30) are non-cubic and appear as euhedral, hexagonal cross-sections in thin section. They share some similarities and differences: 1) both have an As-rich overgrowth on earlier corroded cores with the overgrowth having elevated Au, Pb, and Sb and less consistent Mo and Bi; 2) the auriferous zones surround cores with distinctly different metal associations; the mafic-hosted pyrite has a core dominated by Ni, whereas the intermediate-hosted has Bi, Ni, Co, and Cu; 3) the mafic-hosted pyrite has chalcopyrite inclusions in its core, whereas for the intermediate-hosted pyrite the Cu is more uniformly enriched and likely structurally bound; 4) there is a distinct late Ag-Te event in the Contact Zone pyrite; and 5) a late discordant zone enriched in Ti-W cuts the intermediate pyrite. Although the elemental paragenetic diagrams indicate differences between these grains, they show that pyrite in all cases underwent several stages of growth and late Au is associated with As-Pb-Sb.

The pyrite grains mapped from Hislop (Fig. 31) are euhedral to anhedral with cubic habits. Several distinct zones are observed: 1) a Co-rich core with elevated Te and minor Se, which overgrows inclusions of chalcopyrite (Cu) and scheelite (W); 2) an overgrowth and/or cross-cutting zone with further enrichment of Co, Te, and Se, as well as elevated Au, Ag, Pb, Sb, and As; and 3) a late overgrowth with Mo, Zn and Sn with Mo defining the perimeter of the grain.

The pyrite from Black Fox (Fig. 32) is cubic and typical of pyrites in the albitized and pyritized felsic intrusive host. This grain shows several distinct stages of growth: 1) an early core with zones enriched in Co and Ni (with some Te); 2) further pyrite growth enriched in Te-Se; 3) a stage enriched in As accompanied by additional Co-Ni; and 4) late event with Pb and Bi on the grain perimeter and along with Au-Ag-Te (Cu-Zn not shown) also penetrating into the pyrite's interior.

2.9.3.2 Comparative trace-element chemistry of pyrites

The LA ICP-MS trace-element data for Au, Ag, As, Bi, Cu, Mo, Sb, and Te in pyrite are plotted on box and whisker plots in Figure 33 for the three deposits. Important points to note are: 1) pyrite from Grey Fox and Hislop have elevated Au (>100 ppm and >40 ppm, respectively), whereas it is relatively depleted at Black Fox (<10 ppm); 2) although similar patterns for Au are seen for Ag (1-1,000 ppm) and Mo (1-100 ppm), they are most enriched at Hislop and depleted at Black Fox; 3) As (10-1,000 ppm) and Cu (10-10,000 ppm), which overall show the most enrichment, are more enriched in Grey Fox; 4) Bi (0.1-100 ppm) and Sb (0.5-100 ppm) have the lowest overall enrichment and are similar among deposits; and 5) Te (5-1,000 ppm) is most enriched at Hislop and Black Fox.

2.10 DISCUSSION

2.10.1 Chemical and textural features of host metavolcanic rocks at Grey Fox and Hislop deposits

The host metavolcanic rocks in the study area range in composition from ultramafic to felsic using Zr/Ti and REE contents (Fig. 4). Furthermore, although their primary mineralogy is

obscured by alteration and deformation, lithochemistry defines two subgroups among the ultramafic rocks (Fig. 4C, 16, Table 2). In this regard, the talc-carbonate subunit, characterized by low ΣREE , TiO_2 and Al_2O_3 (typically at or below detection limits) but very high MgO , was originally composed dominantly of olivine or orthopyroxene with little to no feldspar and would likely represent an ultramafic rock of cumulate origin (Downes, 2021). In contrast, the chlorite-albite-carbonate subgroup, which exhibits relatively higher ΣREE , TiO_2 , Al_2O_3 and Cr , but lower MgO and Ni , likely represents a komatiitic basalt originally composed of pyroxene, plagioclase, and chromite.

Chemical affinity diagrams (e.g., Zr/Ti ; Fig. 4) show very consistent trends among the various metavolcanic units, particularly for those of mafic to felsic composition. Together with the strong similarities in their REE patterns (Fig. 4C), the geochemical characteristics suggest the units are genetically related. The metavolcanic rocks also define a continuous tholeiitic Fe enrichment trend from mafic through intermediate to felsic on the Jensen Cation Plot (Fig. 4D), further suggesting they are related.

Pillow lobes commonly observed in the mafic metavolcanic rocks, in addition to their massive, fine-grained, and crystalline nature suggest an erupted subaqueous volcanic origin. The intermediate metavolcanics contain an abundance of flow-top volcanic features, such as hyaloclastites and spherulites; spherulites are also present in the felsic metavolcanics with a similar mineralogy and texture. In some cases, the spherulites coalesce and form more massive zones, such as at Hislop deposit (Fig. 5H, I), but the distinct textures are still present in thin section. The spherulites comprise radial lineations of mafic grains within larger domains of albite and/or quartz. In least altered samples, these mafic phases are chlorite or amphibole, likely after pyroxenes (Jones, 1992), whereas in altered samples they are carbonate and/or rutile. Spherulites are

interpreted to have resulted from either undercooling of superheated melt, which would promote rapid disequilibrium crystal growth (Jones, 1992; Fowler et al., 2002; Dinel et al., 2008) or through devitrification of an originally glassy material, which in some cases nucleate along perlitic fractures that develop during cooling (Lofgren, 1971; Dinel et al., 2008).

As discussed by Jones (1992), variolitic (spherulitic) textures typically form in Fe-rich tholeiitic sequences with more differentiated compositions (i.e., higher SiO₂, FeO, TiO₂, P₂O₅). As a result, these Fe-rich tholeiitic rocks with higher Fe/Mg ratios are more favourable for later gold mineralization due to: 1) an increased ability to scavenge Au transported as bisulphide complexes by reacting with the sulphide ligand (e.g., Böhlke, 1988); and 2) higher tendency for brittle failure (Jones, 1992) that enhances permeability and increases the volume of rock the fluids interact with. Thus, for these reasons the spherulitic units at the Grey Fox and Hislop deposits are considered one of the preferential hosts to Au mineralization.

2.10.2 Nature of felsic-intermediate intrusions and lamprophyres at Hislop, Grey Fox, and Black Fox

The felsic-intermediate intrusions can be broadly grouped into 3 types based on their mineralogy and geochemistry: 1) syenites, 2) melanosyenites, and 3) quartz-feldspar porphyries (QFPs), (Fig. 7, Table 3). Although two phases of syenites were identified in this study (Syenite I and Syenite II; Fig. 6), their similar geochemistry suggests that these are part of the same intrusive suite (Fig. 7). On the QAP diagram (Fig. 7D), the syenites along with the melanosyenites define an alkaline trend, whereas the QAP defines a calc alkaline trend (Lameyre and Bowden, 1982; Rahaman et al., 2019). This suggests that these two suites of intrusions are derived from different parental magma sources and is in agreement with the REE profiles, with the QFP showing a

distinctly higher enrichment of LREE (Fig. 7E). The REE profiles for mineralized syenites (Fig. 7E, F) define a slightly different profile than the other alkaline units, having distinctly lower intermediate REEs compared to both the mineralized syenite and melanosyenite groups. As such, the mineralized syenites are thought to be either 1) a distinct intrusion suite specifically associated with mineralization, or 2) heavily altered melanosyenites, where the addition of SiO₂ with alteration and/or veining would dilute the REE concentrations (Fig. 7E) and produce normative quartz in the mineralogy calculations (Table 3; Fig. 7D). Additionally, the altered and weakly mineralized felsic intrusive units from the Black Fox open pit have an overall similar REE profile as the mineralized syenites from Hislop (Fig. 7; dark blue) and may be part of the same intrusion event, although more work is needed to confirm this. It should be noted that as these samples are all altered, mobility of major elements (e.g., SiO₂, Na₂O, and K₂O) is likely present and would affect the normative calculation and therefore the QAP diagram, and these results along with diagrams using mobile elements must be taken with a level of caution. The location of these alkaline units on the Pearce diagram (Fig. 7B), which would be relatively unaffected by alteration, further suggests that the interpreted alkaline nature of these units may be a result of alteration. In fact, these units may represent episyenites as defined by Lacroix (1920), however this study did not go into detail on this aspect. Although rare, the presence has been noted elsewhere in the AGB (Katz, 2016; Jébrak and Doucet, 2002; Arteaga, 2018), and they may in fact be more common than currently recognized (Arteaga, 2018).

Additionally, the lamprophyric intrusions (LAM) are also identified at all three deposits (Fig. 8), with a similar profile to the syenites and melanosyenites and may represent a more primitive version of the same melt (Van Lichtervelde, 2002). At Hislop, where the relations were more studied, the syenites, melanosyenites, and LAMs are relatively early and host to

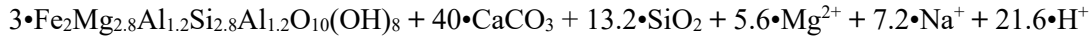
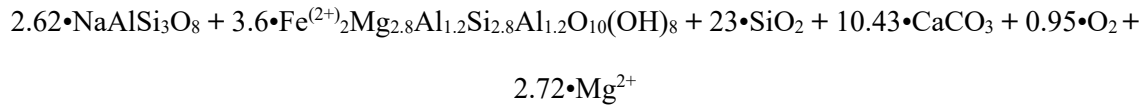
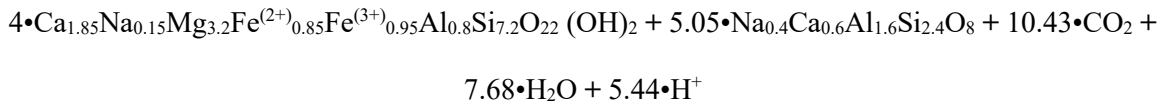
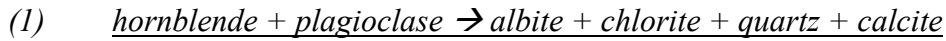
mineralization, with a mineralized syenite xenolith also contained within a LAM, indicating that the LAM intrusions are broadly synchronous with the mineralizing event. Similarly, the lower level of alteration in Syenite II relative to Syenite I, in combination with the similarities in their chemical makeup suggesting formation from the same magma, would suggest this suite also formed broadly synchronous with the mineralizing event. Conversely, the QFP are relatively unmineralized. Similarly, the intrusions analyzed from Black Fox include a QFP hosted within the carbonate-talc altered ultramafic metavolcanics with little mineralization, while the heavily altered and mineralized intrusion samples are more akin to the alkaline suite (melanosyenite and LAM), as determined mainly through the REE profile.

2.10.3 Nature of mineralization at Grey Fox

2.10.3.1 Alteration

The alteration history is broadly similar among the three zones studied and its derived paragenesis is summarized in Figure 34. The assemblages are typically similar, but modal abundances differ and are host rock dependent. For the least altered mafic- and intermediate metavolcanic rocks, the inferred initial metamorphic assemblage consisted of hornblende, likely after pyroxene, and plagioclase with ilmenite, magnetite, and variable leucoxene. However, the composition of the flow-top metavolcanic rocks is ambiguous due to the fine-grained nature of the rock and the high level of alteration. These mineral assemblages are consistent with an amphibolite metamorphic facies, thus a higher metamorphic grade than is typical for the AGB, i.e., greenschist- to subgreenschist-facies (Ayer et al., 2005). This higher metamorphic grade may relate to contact metamorphism associated with local alkaline intrusive magmatism of the later ca. 2680 Ma Timiskaming event. Such contact aureoles are noted in magmatic-sourced, intrusion-related gold

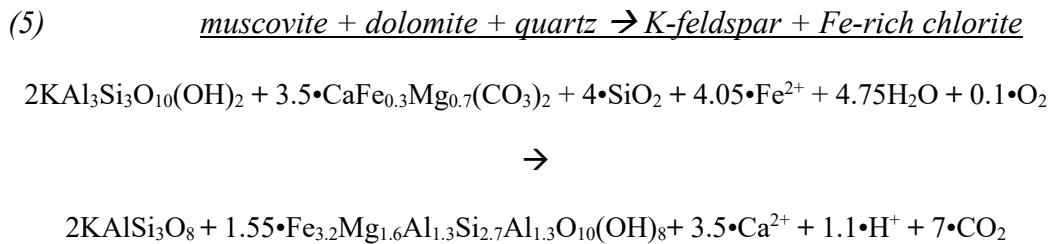
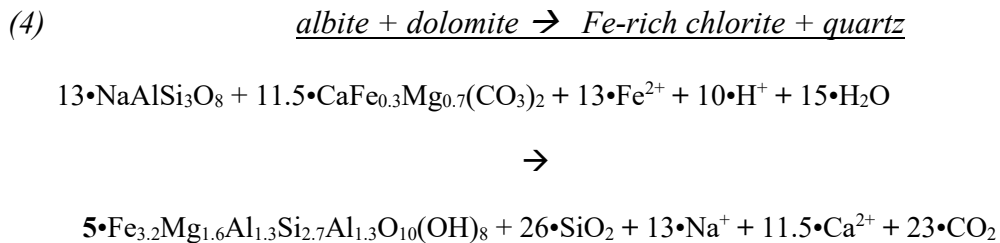
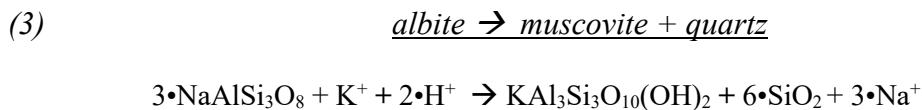
settings (Hart, 2005) where, as magmatic activity waned, hydrothermal activity became more prominent and the earlier metamorphic assemblage is overprinted. Thus, in this context are noted the three distinct alterations documented at Grey Fox - a chlorite-albite-quartz (Type 1), sodic-carbonate (Type 2), and muscovite-chlorite (Type 3) (Figs. 3, 10, 11, and 12). Using mineral chemistry based on SEM-EDS analysis, the following balanced reactions were derived:



Chlorite-albite-quartz and sodic-carbonate alteration: These alterations are considered to represent the same event based on the progressive textural development. The chl-ab-qz (1) event is generally isochemical (Fig. 21) and reflects the addition of CO₂, introduced as part of a typical H₂O-CO₂ fluid, which reacted with Ca liberated from the breakdown of the hornblende + plagioclase assemblage. Although SiO₂ is also liberated, it was likely introduced by the fluid as well. Finally, some Mg²⁺ was also liberated by this reaction, which is consistent with the SEM raster chemistry (Fig. 21D). The Ti-bearing phases present vary depending on the host rock and degree of alteration, in particular addition of CO₂. Thus, rutile observed in the Contact Zone is associated with weakly disseminated dolomite related to the more progressive alteration, whereas

titanite and ilmenite are stable in the 147 Zone, which lacks dolomite. No Ti-bearing phase is noted from the South Zone, reflecting the Ti-poor felsic nature of these metavolcanic rocks.

The sodic-carbonate (2) altered rocks are dominated by albite and Fe-bearing dolomite, with lesser quartz and chlorite, and again reflects addition of CO₂. As already noted, the preferential plucking of carbonate during thin section preparation compromised tracking Ca mobility. However, mass balance calculations indicate a loss of Ca (25-50%; Fig. 25A) during this alteration. Dolomite likely formed during breakdown of chlorite (2), as well as from the liberation of Mg²⁺ in reaction (1). The liberated Al formed albite with Na introduced from the fluid (Figs. 21H and 25A). Although some SEM-EDS raster analyses show an increase in K (Fig. 21I), this is attributed to muscovite-chlorite alteration in minor amounts that was pervasively present through later fracture-controlled alteration and accounts for the increase in K in these samples. The Ti-bearing phase in this alteration was effectively all rutile across all zones.



Muscovite-chlorite and K-feldspar alteration: These alteration types post-date the chlorite-albite-quartz and sodic-carbonate alterations discussed above, which based on textural relationships are considered to reflect ingress of the same fluid. The development of K-feldspar and the muscovite-chlorite assemblages are transitional based on textures, and in the context of mineral stability may relate to equilibration of a K-rich fluid under increasing fluid:rock ratios, as well as higher temperature to develop a proximal versus distal alteration (Fig. 35; Seedorff et al., 2005). As documented in the above reactions (3-5), the modal abundance of muscovite, chlorite, and K-feldspar will be controlled by the availability of K, as well as the stability of muscovite versus K-feldspar. From reaction (5), for a constant K, more chlorite will form with a K-feldspar-stable alteration than muscovite-stable due to the K:Al ratio of the two phases.

The overall addition of K in this alteration stage and the presence of hematite in the assemblage (reflecting the oxidation state of the system) along with introduction of Mo and As with Au as noted in the mass balance (Fig. 25B), suggests a magmatic-hydrothermal fluid possibly derived from the local felsic intrusions. This aspect is explored in more detail below.

2.10.3.2 Veining and source of fluids

The nature of veining is consistent across the three mineralized zones studied. The crustiform and colloform, open-space filling textures and multistage formation of veins strongly resemble similar vein features in low-sulphidation, epithermal settings found at relatively shallow crustal levels (i.e., <1 km depths; Sillitoe, 2015). Previous workers have also suggested such settings for similar mineralization styles in the AGB (e.g., Robert, 2001; Robert et al., 2007; Ropchan et al., 2002; Mériaud and Jébrak, 2017; Fayol and Jébrak, 2017). Additionally, the

association of these veins in units with high permeability (i.e., flow-top metavolcanic facies, rheologic contacts) is noted, as these features preferentially focus fluids into such open spaces.

The initial vein stage was dominated by quartz, which is commonly dark grey due to the presence of fine-grained molybdenite; both white and dark varieties of quartz veins are auriferous. The next vein stage typically has coarse-grained dolomite, with alternating Mg- and Fe-rich growth zones, which is followed by a fine-grained intergrowth of quartz and carbonate. Minor gold was observed in the latter stage in thin section but is rare; it is absent in the intermediate, carbonate only stage. Rare instances of quartz + molybdenite veins cutting the fine-grained quartz-carbonate veins (Fig. 18E) provide evidence for at least 2 injections of auriferous fluid. The nature of this vein forming fluid is considered to be magmatic based on its epizonal setting and the associated metals and is in agreement with the high homogenization temperatures (i.e., ca. 300°C) for primary fluid inclusions in the early quartz stage (G. Tuba, Pers. comm.; Tuba et al., 2021).

2.10.3.3 Auriferous pyrite and its trace-metal chemistry

The auriferous pyrite grains have a very distinct habit and trace-metal chemistry that is consistent across the studied areas. These aspects are explored separately below in the context of their implications for gold mineralization.

The distinct habit of the auriferous pyrite (e.g., hexagonal cross-sections: Figs. 29, 30) reflects its change from cubic to octahedral or pyritohedral forms (Fig. 36, A. McDonald, pers. comm.). As shown by the experimental work of Murowchick and Barnes (1987), low degrees of supersaturation favour cubic pyrite, whereas at increasing degrees of supersaturation octahedral and pyritohedral habits are preferred. The pyrite at Grey Fox may, therefore, indicate a relative high state of supersaturation, which necessitates a sudden change in physiochemical parameters

related to either fluid chemistry or temperature. As this study lacks such relevant information, it is not possible to elaborate further which of these parameters was the controlling factor. However, as Murowchick and Barnes (1987) suggest, pyrite habit may be useful in mapping zones of its supersaturation. Since this habit of pyrite is directly tied to the mineralized zones at Grey Fox, we note that it could be used to map out mineralized zones. Furthermore, the change in pyrite habit may also relate to As substitution in the pyrite (e.g., Sunagawa and Takahashi, 1955; Chouinard et al., 2005) since it enhances the growth of the {111} face. It is likely that both fluctuating fluid conditions and pyrite chemistry contributed to the observed habits of the auriferous pyrite grains.

The noted negative correlation between As versus S in pyrite (Fig. 24B), along with the presence of Au in the As-rich growth zones (Figs. 29 and 30) is important, as As enhances pyrite's ability to incorporate Au (Reich et al., 2005; Lawley et al., 2015; Neyedley et al., 2017; Kerr et al., 2018; Hastie et al., 2020;). Lastly, the prominent inflection point in the whole-rock data (Fig. 28B) mimics trends in aforementioned studies of arsenian pyrite and further emphasizes the importance of As in controlling the uptake of Au in pyrite.

Although the detailed elemental paragenesis for pyrites at the Contact and 147 zones differ, several aspects relevant to mineralization are noted. Firstly, the auriferous zones have a similar metal association of Au-As-Sb-Pb, which mirrors the whole-rock data (Figs. 29 and 30), except for Mo, and also is implied by mass balance calculations (Fig. 25). Secondly, the lack of a Au-W association in the pyrite is reflected by the poor Au-W correlation for whole-rock data. Its absence in the auriferous zones in pyrite may relate, however, to the presence of rutile as a relatively abundant and stable phase in alteration zones as it can sequester W (e.g., Cave et al., 2017) over pyrite. This is seen by the overlap of Ti and W in the elemental maps that suggests rutile inclusions are present in the auriferous pyrites, as is documented in other gold deposits (e.g., Graham and

Morris, 1973). The rare presence of fine-grained scheelite in mineralized samples (Gelinás, 2012) also indicates W was taken up by this phase. Thirdly, Mo, which is common as molybdenite in veins and alteration, was also noted by Gelinás (2012) to be associated with Au in the whole-rock data but lacking in the pyrite. Thus, as with W and rutile, Mo is preferentially sequestered into a competing phase. Lastly, in pyrite grains, Au-rich zones overgrow barren cores. This indicates auriferous pyrite was not an early phase and only when the As was present in the fluid could Au partition into pyrite. Additionally, the Au element map for pyrite from the 147 Zone shows two distinct auriferous zones, thus two distinct gold fluid events, which is in agreement with the previously presented repetition of the auriferous veining events.

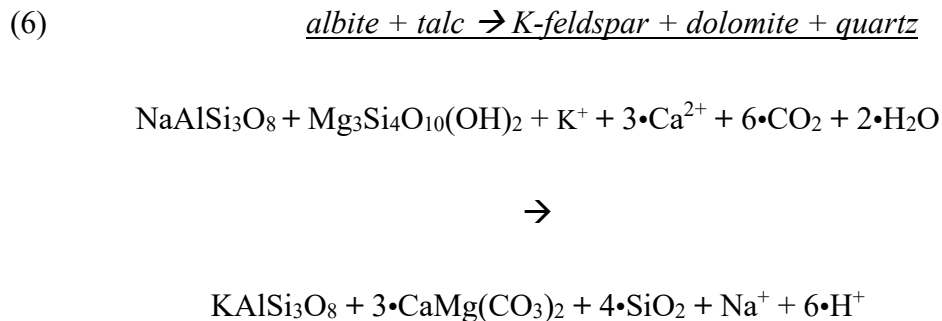
2.10.3.4 Relationship to deformation

The crustiform-textured quartz veins in sheared ultramafic metavolcanic rocks are boudinaged and brecciated at depth (Fig. 18F), whereas away from this zone the host metavolcanic rocks show little evidence of deformation. As veins and mineralization extend throughout the three zones and away from this contact, versus preferentially localized to it, this strongly suggests mineralization pre-dated ductile deformation. That the veins infill brittle features and have textures indicative of a shallow level contrasts with typical ductile features associated with deeper settings of orogenic gold systems (McCuaig and Kerrich, 1998; Groves et al., 1998; Goldfarb et al., 2005). Furthermore, as suggested above and below, the mineralizing fluids are inferred to originate from an underlying felsic magma reservoir interpreted by Berger (2002) to be of Timiskaming age, possibly a temporal equivalent to the 2678 ± 2 Ma nearby Garrison stock (Fig. 2; Corfu et al., 1989). The latter aligns therefore with the recent tectonic model of Bleeker (2015) whereby the Timiskaming basin formed in an extensional regime that was later overprinted by ductile deformation due to its subsequent collapse during contraction.

2.10.4 Nature of mineralization at Hislop

2.10.4.1 Alteration

The alteration is characterized by two distinct events, as summarized paragenetically in Figure 37. The mafic metavolcanic rocks have similar hornblende to that at Grey Fox, which is considered of metamorphic origin. At Grey Fox, this assemblage was first overprinted by a chlorite-albite-quartz and sodic-carbonate alteration and then by muscovite-chlorite, whereas at Hislop the muscovite alteration appears to be in equilibrium with the hornblende. Rare K-feldspar veinlets that cut this assemblage is interpreted to be broadly synchronous with peak metamorphism. A later, vein-associated sodic-carbonate alteration is documented to cut the potassic alteration. Both alteration types have gold associated with them. The following idealized reactions are given below because the chemical composition is not known:

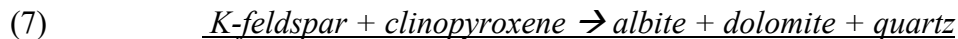


Potassic alteration; Observed in all units, its mineralogy and abundance are dependent on fluid:rock ratio and the host. In the ultramafic metavolcanic rocks, K-feldspar and dolomite are stable in addition to significant carbonate veining and breccia; a later fracture-controlled fuchsite alteration cuts the latter carbonate veining. Mass balance shows this alteration is characterized by gains of K₂O and C with loss of Na₂O and SiO₂ (Fig. 26), which reflects replacement of albite+talc by K-feldspar+dolomite. Gold and related elements, such as As, W, Se, and Te, with lesser Sb,

Mo, U, and minor HREE, were also gained during alteration. Elevated As, W, and Se extend beyond the Au-bearing alteration and is relevant for vectoring.

The mineralogy of the least altered mafic and felsic metavolcanic rocks, along with the syenites, is summarized in Table 5. From this, it is evident that K-feldspar dominates the felsic units along with clinopyroxene and albite, whereas muscovite dominates the more mafic units with hornblende, albite, and plagioclase, as well as the matrix of the syenite. This mineralogy reflects interaction of host rocks with a fluid (i.e., fluid:rock ratio) and its physiochemical conditions, as noted above for Grey Fox (Fig. 35), with the felsic metavolcanics rocks having a higher intrinsic permeability resulting in a greater fluid:rock interaction. In addition to the K-feldspar, abundant hematite is associated with this alteration in the felsic metavolcanics, indicating a relatively oxidized environment.

The significant addition of K in all units, the oxidized nature of the alteration in the felsic metavolcanic rocks, and the association of As and Mo with Au documented in the ultramafic metavolcanic rocks, is similar to the muscovite-chlorite and K-feldspar alteration at Grey Fox and again suggests a magmatic-hydrothermal source fluid.



Sodic-carbonate: This alteration is more restricted than the potassic alteration and is documented as vein halos in the felsic metavolcanic rocks and the syenite at the centre of the deposit. In the former, a progressive alteration was observed associated with the introduction of

gold; distal to the vein (~1 m), K-feldspar is nearly completely replaced by albite, clinopyroxene is replaced by dolomite, titanite by rutile, and hematite remains and is more abundant; from this, the liberated Fe shown in reaction (7) would be forming the hematite. This suggests the interaction of a relatively oxidized fluid, which introduced Na₂O, CO₂, CaO and is supported by mass balance (Fig. 27A). In the more progressed alteration proximal to the veins, quartz becomes more abundant, minor chlorite forms, and hematite is replaced by auriferous pyrite. Albite is still abundant, however, mass balance shows an overall loss of Na₂O (Fig. 27B). This can be attributed to formation of new chlorite, although not well documented, and variation in the abundance of residual K-feldspar, as evidenced by a slightly higher K₂O in the more progressed alteration. Akin to what is observed at Grey Fox, the Fe# of chlorite and carbonate increases in the auriferous samples (Figs. 22 and 23), although this trend is more variable at Hislop, likely due to the lack of chlorite in the earlier alteration. Significant Mo, Te, and Ag were introduced with the gold, with lesser As, and Pb (Fig. 27B).

2.10.4.2 Veining

Veining, present in felsic metavolcanic rocks and to a lesser extent in the syenite, have two dominant orientations that are similar to those at Grey Fox (Fig. 17A). They are interpreted to be conjugate veins, evidenced by their mutual cross-cutting nature (Fig. 18B). Unlike Grey Fox, carbonate is not as abundant and open-space crustiform textures are not present, but zones of breccia veining were observed.

2.10.4.3 Geochemical signature of pyrite and mass balance

The cubic habit of pyrite, its element map, the elemental associations, and the very diffuse element zoning differ compared to Grey Fox. Thus, the cubic shape may indicate a more

equilibrium state for pyrite formation, in contrast to the suggested supersaturation of pyrite at Grey Fox described above. As for the very diffuse element zoning in pyrite (Fig. 31), this strongly suggests the pyrite has undergone substantial modification during growth due to coupled dissolution-precipitation processes, as noted in other similar studies (e.g., Neyedley et al., 2017; Gourcerol et al., 2018b; Hastie et al., 2020). The latter is best exemplified in the stage 4 growth of pyrite by the network of cross-cutting zones enriched in Pb-Bi-Sb-As (Fig. 31).

This pyrite records an early fluid event represented by Cu, Ti, and W, which is overgrown by pyrite enriched in Co-Te-Se. This is followed by a stage of dissolution (stage 3), noted above, with associated precipitation and enrichment of Co-Te-Se-Au-Ag-Pb-Sb-As-Bi. Finally, this is overgrown by pyrite with Mo-Zn-Sn. Lacking in this pyrite is the clear relationship between As and Au that is strongly evident at Grey Fox (Figs. 29 and 30), and which is considered a prerequisite for incorporating Au into pyrite (Reich et al., 2005). The pyrite compares to the mass balance data derived from the isocon plots, which showed that for the potassic alteration there is an enrichment of Au, As, W, Se, Te, Tl, Sb, Mo, Ag, Bi, and Cu and for the sodic-carbonate there is an enrichment of Au, Ag, Mo, As, and Te with variable enrichment of W, Cu, and Pb. Thus, although the two methods reveal a similar element suite associated with mineralization, it is from the pyrite element maps that a related elemental paragenesis can be inferred as the association of Au with these metals can be directly observed.

2.10.4.4 Relationship to magmatism

As LAM dykes both host mineralization and contain xenoliths of mineralized syenites, this indicates that magmatism overlaps with the K-associated mineralization event. Troop (1989) also has noted the presence of felsic intrusive xenoliths in deformed lamprophyric dikes regionally,

such as at the Vimy gold mine ca. 8 km to the southwest, suggesting that a period of felsic magmatic activity occurred on a more regional scale that predates at least some of the lamprophyric intrusions. Similarly, the differing levels of alteration in Syenite I and Syenite II, despite proximity and similar geochemical natures of the two intrusions, would suggest that these intruded during different stages of the mineralization/alteration events. Additionally, the similarities in the REE profiles, along with the potassic-rich nature of the syenite, melanosyenite, and LAM intrusions studied at the Hislop deposit, suggest that these represent a related suite of intrusions with the same parental source (Van Lichtenvelde, 2002). Similar relations of syenites resulting from the evolution of lamprophyric magmas has been demonstrated in studies previously and interpreted to be from a mantle source (Rowins et al., 1993). At present, the only age constraints for syenitic magmatism in the area is provided for the nearby Garrison stock (Fig. 2) dated at 2678 ± 2 Ma (Corfu et al., 1989), which overlaps with the time of Timiskaming magmatism in the region of ca. 2680 Ma (Berger, 2002; Ayer et al., 2005).

QFPs are also present, although are chemically distinct from the K-rich intrusive units and not significantly mineralized. The dominant alteration in this suite is albitization, and they lack the large scale potassic alteration identified in the other units and linked with Au-mineralization (Van Lichtenvelde, 2002).

2.10.4.5 Relationship to deformation

The presence of the mineralized syenite by Van Lichtenvelde (2002) within a deformed LAM dyke suggests that periods of ductile deformation post-dated the potassic mineralizing event. Similarly, the veins at Grey Fox are brecciated and deformed by a ductile deformation event at depth (Fig. 18H) and suggest a relatively early formation. Due to the epizonal nature of the veins

indicating a shallow level of emplacement (i.e., epizonal <1 km; Sillitoe, 2015) and the overprinting ductile deformation, we suggest that the mineralizing event at Hislop and Grey Fox was a relatively early and distinct event, pre-dating much of the ductile deformation that is recorded in the ultramafics.

2.10.5 Mineralization at Black Fox

2.10.5.1 Alteration

Au mineralization associated with quartz-carbonate veining is present in both chlorite-carbonate and fuchsite-altered ultramafic rocks, which represent altered komatiitic basalt protoliths and is distinct from the carbonate-talc altered ultramafic metavolcanic rocks, which represent an olivine cumulate and are generally barren in the shallower portions of the deposit (Mitrofanov et al., 2018). Mineralization is also present in albitized and pyritized boudins of felsic intrusions hosted in deformed ultramafic rocks. Although not studied in depth, the fuchsite alteration identified at Black Fox appears relatively late (Fig. 16D). This, in conjunction with the alteration not being distinctly associated with the presence of gold in the komatiitic basalt, leads us to interpret that the fuchsite alteration may represent a separate event than that which introduced gold in the chlorite-carbonate altered ultramafic rocks. Due to the relatively late timing, it may in fact post-date the gold mineralization entirely, or it may represent a second gold event that is spatially overlapping, however more work is needed on this front.

2.10.5.2 Vein formation and gold mineralization

Gold mineralization is intimately related to the abundance of veins, which includes both fault-fill and en echelon extensional veins (Fig. 20A, B) and is typical of other deposits in the

AGB (e.g. Dubé and Gosselin, 2007; Ispolotov et al., 2008). At Black Fox, their formation is related to a single protracted deformation event involving progressive north-south shortening during collapse of the Timiskaming basin at ca. <2670 Ma (Haugaard et al., 2021; Mitrofanov et al., 2018; Dubé et al., 2017; Bleeker, 2015). Recent work at the Garrison setting (35 km E) by Nassif et al. (2018) constrain emplacement of similar veins within the PDFZ to 2657 ± 15 Ma. The nature and type of veining at Black Fox is similar to quartz-carbonate veins documented in many orogenic gold deposit settings both in the AGB (e.g., Dubé and Gosselin, 2007) and globally (Goldfarb et al., 2005). Of particular relevance to the origin of such veins is the presence of thin septae or laminations of altered and deformed wall rock entrained in the veins, such as seen in this study (Fig. 20A). These features are consistent with the fault-valve model involving cycling of fluid pressure (Sibson et al., 1988; Robert and Poulsen, 2001) whereby over-pressured fluids are focused into fault zones, which leads to their rupture and filling of the dilatant zones by quartz veins, the dominant type (i.e., shear versus en echelon) depending on ambient parameters (e.g., lithostatic versus fluid pressure, anisotropy). The septae in such veins are also important as visible gold is often seen to adhere to such surfaces (Fig. 20C).

2.10.5.3 Auriferous pyrite

The lack of abundant Au in a mapped pyrite grain (i.e., >99 % of data is < 1 ppm; Fig. 33) from an altered felsic intrusive limits the ability to interpret the context of Au mineralization at Black Fox since its relationship to the high-grade veins is ambiguous. Despite this shortcoming, we note that the grain reveals a protracted and complex paragenesis: an early Co-Ni stage followed by Se-Te, a second Co-Ni stage, and lastly a Pb-Bi-Ag-Au(-Zn) stage (Fig. 32). Much of the growth of the pyrite involved dissolution as it evolved, as seen for example by the irregular distribution patterns of elements such as Te, the second stage Ni and the late Pb-Bi-Pb-Ag stage.

It is interesting to note that the late Au event lacks the same Au-As coupled enrichment as seen in pyrite from Grey Fox. As there is no lithogeochemical database, as there is for Grey Fox, it is not possible to compare the elemental associations to the main mineralized zone.

2.10.5.4 Relationship to deformation

The vein related mineralization is interpreted to be synchronous with a D₃ north-south shortening event, which produced south-over-north shears accompanied by north verging folds (Haugaard et al., 2021; Mitrofanov et al., 2018), which is also supported by the recent work of Nassif et al. (2018). This kinetic pattern is seen as folded quartz-carbonate veins with ribbons of entrained foliated wall rock material (Fig. 20A). This deformation event post-dates the deposition of Timiskaming sedimentary rocks and represent a very different deformation regime, as it records contraction versus the earlier extension which led to basin formation (Bleeker, 2015). Furthermore, this syn-deformation style of mineralization with related veining and significant ductile deformation is typically interpreted to form under brittle-ductile conditions at pressures of 2-4 kbars (Robert et al., 1997; Groves et al., 2003; Goldfarb et al., 2005; Dubé and Gosselin, 2007).

2.10.6 Comparison of the deposits in the Hislop township

Based on their temporal relation to deformation and interpreted depth of formation, the Grey Fox, Hislop, and Black Fox deposits are interpreted to have formed during two events. Whereas Grey Fox and Hislop formed at relatively shallow depths, pre-date the local D₃ and D₄ events, and are interpreted to be associated with Timiskaming-aged felsic magmatism (e.g., nearby 2678 ± 2 Ma Garrison stock; Corfu et al., 1989), the Black Fox deposit formed at intermediate depths with veining broadly coeval with D₃ deformation. Therefore, the Black Fox deposit represents a distinctly different and later gold event than that documented at the Grey Fox and

Hislop deposits (Fig. 38) and may consist of gold remobilized from this earlier, intrusion-associated mineralization.

2.10.6.1 Comparison of the intrusion-associated Grey Fox and Hislop deposit settings

The Grey Fox and Hislop deposits are characterized by: 1) an elevated metamorphic grade (amphibole facies); 2) weakly deformed to undeformed host rocks; 3) an auriferous K- and hematite-bearing alteration; 4) similar vein orientations; and 5) a broadly similar metal association. Conversely, some differences also exist: 1) muscovite >> K-feldspar at Grey Fox versus K-feldspar >> muscovite at Hislop; 2) the timing of peak metamorphism versus alteration; the former pre-dating alteration at Grey Fox, whereas at Hislop they are synchronous; 3) timing of sodic-carbonate alteration, which pre-dates main veining at Grey Fox versus syn-veining at Hislop; and 4) the association of Au with sodic-carbonate alteration at Hislop, but generally barren at Grey Fox.

Based on the many similarities between the two deposits, specifically the K-bearing alteration and Au-metal associations, in particular with Mo, the deposits are considered to share a common genesis and represent two parts of a magmatically driven hydrothermal system. The fluids are considered to originate from an alkali magma at depth, from which the intrusions were also sourced at ca. 2680 Ma based on evidence for widespread similar magmatism at this time (Bleeker, 2015; Corfu et al., 1989). The differences listed above between the two deposits are explained below.

2.10.6.2 Controls of depth on fluid migration in relation to deposit formation

The host rocks for intrusion-associated versus typical orogenic mineralization differ, which provides insight into the different mineralizing environments. In epizonal-style mineralization, the shallow level favours brittle behavior and fluids migrate along fracture networks. As the felsic- and intermediate metavolcanic rocks are more competent and have abundant flow-top features and thus higher intrinsic permeability, these units are more likely to fracture during brittle deformation (Cox et al., 2001). Thus, these units were conduits for ascending fluids similar to channeling in porphyry-epithermal systems (Corbett, 2007; Sillitoe, 2010). A similar host rock control has been documented by Dinel et al. (2008) in Timmins for the intermediate- to felsic fragmental rocks of the Vipond Formation that host the McIntyre gold deposit. In contrast is the mesozonal-style mineralization at Black Fox, which formed at greater depth and is commonly interpreted to be in the brittle-ductile transition zone where fluid migration is promoted via induced shearing and periodic fault slips (Sibson et al., 1988; Sibson, 1996; Phillips and Powell, 2010). In this setting, much of the deformation is localized to the ultramafic metavolcanic rocks, which preferentially deform in a ductile manner. Vein formation, however, requires the rock to fail and thus create open space for fluids and this preferentially occurred in the relatively more competent komatiitic basalt. Similarly, the contacts between slivers or boudins of felsic intrusions within the strongly sheared intervals of ultramafic rocks, as well as the intrusions themselves, are preferential sites for fracturing, fluid flow, and vein formation.

2.10.7 Related mineralized zones in the Hislop township

Three deposits in the Hislop township share several similar key features with the Hislop and Grey Fox deposits. They are included in Figure 2 and summarized in Table 7. The Ross Mine

produced over 1 Moz of Au, 1.4 Moz of Ag and significant Cu (ca. 0.6 % Cu) during its mine life (Akande, 1982). Berger (2002) noted the similarities between the Ross mine and epithermal Au-Ag deposits, and further suggested that the mineralization event may be related to an alkali hydrothermal system with shallow levels of emplacements. The rock unit hosting mineralization is variably interpreted as a felsic fragmental (Jones, 1948), a highly altered basalt (Troop, 1985, 1986), and metasedimentary rocks of the Timiskaming assemblage (Berger, 2002). Additionally, Troop (1986) documented a breccia ore with maximum Au grades of 10 g/t and similarly high Ag. The association of alteration and mineralization with fragmental units and brecciation parallels the observations for the Grey Fox and Hislop deposits. Troop (ibid) also noted that there is an increase in Ag content associated with the breccia veins, as well as narrow brittle-type veins, with decreasing depth, and that Fe-rich carbonate (ankerite), muscovite, and hematite are spatially related to Au.

Less information is available for other deposits in the area. The Gibson deposit, which is located less than 1 km west of the Grey Fox Contact Zone, is characterized by high-grade quartz veins at a brecciated contact between basaltic rocks and a syenitic intrusion (Troop, 1989; Mitrofanov et al., 2018). The geologic setting is thus similar to Hislop where mineralization is also focused at the contact between a syenite and metavolcanic rocks, although most auriferous veins at Hislop occurs in the felsic metavolcanic rocks to the north of the contact.

2.10.8 Genetic model for early mineralization in the Hislop township

The aforementioned characteristics of the Grey Fox and Hislop deposits suggest that they are syenite-associated deposits following the earlier classifications (Robert, 2001; Robert et al., 2007) and represent a distinct mineralization event that pre-dates the orogenic mineralization at

the Black Fox deposit. Furthermore, Grey Fox and Hislop represent different zones of a larger magmatic-hydrothermal system and provide insight into how such systems vary in space. Hislop, characterized by a K-feldspar dominant alteration associated with Au mineralization, shows a strong spatial association with the syenite intrusion, which suggests it is a deeper and hotter part of the system. In contrast, Grey Fox represents a shallower and more distal expression of the system and is characterized by abundant crustiform-textured veins intimately associated with Au-mineralization, muscovite and chlorite as the dominant alteration phases, and a strong association with pre-existing structural anisotropies such as the flow-top facies volcanics (i.e., the 147 and South Zones). In this regard, these syenite-associated systems shares similarities with younger (i.e., Phanerozoic) porphyry-epithermal systems (Sillitoe, 2010), and more specifically alkalic systems, which commonly form in areas of extensional tectonics. Interestingly, the latter include some of the highest-grade porphyry-epithermal gold deposits, such as Mount Polley district in British Columbia, Ridgeway in New South Wales, and Lihir in Papua New Guinea (Jensen and Barton, 2000; Chamberlain et al., 2008; Harris and Holcombe, 2014; Zukowski et al., 2014). Additionally, the increased metamorphic grade and metal zonation present at the larger scale resemble key zonation features for intrusion-related gold models (Hart et al., 2002; Hart and Goldfarb, 2005; Hart, 2007). As a result, all three models are taken into consideration to develop the interpretation presented in Figure 39.

Early alkalic intrusions (Hislop, Gibson) intruded into the Tisdale and Timiskaming assemblages during extension at ca. 2680 Ma (Fig. 39B). An early phase of gold mineralization developed that followed, at least in part, the same pathways as the early intrusions, and developed as the K-feldspar dominant alteration that is observed at the Hislop deposit halting the syenite intrusion (Fig. 39C). As the magmatic event was relatively long-lived, it also produced a locally

elevated metamorphic gradient (Fig. 39C) and thus generated a fluid due to local devolatilization of the surrounding rocks that developed the early sodic-carbonate alteration in the peripheries of the system (Grey Fox; Fig. 39D). As the system waned and the magma continued to evolve in the source region, a subsequent fluid was exsolved, followed the same pathways, and resulted in a second, vein-associated, mineralizing event that overprints the initial potassic-rich event (Fig. 39E,F). At Hislop, the veins are associated with a sodic-carbonate alteration, however at Grey Fox the veins are associated with a muscovite-chlorite +/- K-feldspar alteration. As these fluids would be migrating through, and interacting with, the previously potassic-altered rocks (e.g., Hislop), this change in the associated alteration can be attributed to variable levels of wall rock interaction present in the core versus peripheries of the system. In this scenario, the late-stage auriferous fluid would have interacted with the previously potassic-altered rocks, and through this interaction dissolve and advance the potassic alteration. In the Hislop deposit, which is at the core of the system, the vein-associated alteration would be fluid dominated and as such produced a sodic-carbonate alteration. Conversely, at Grey Fox, which is in the more distal parts of the system, the fluid had been modified through its interaction with the potassic altered rocks during migration and has a potassic alteration associated with the mineralization. Magmatic activity, which was long lived and broadly coeval with the mineralization, would have continued and formed relatively late intrusions post-dating the mineralization (e.g., lamprophyres; Fig. 39G;) both pre-dates and post-dates the mineralization, would have continued. Such protracted and overprinting relationships are unusual for many porphyry deposit settings (Sillitoe, 2010). These events could therefore have introduced new gold and other metals or remobilized them from the earlier event, or both.

The associated metals at both deposits are largely similar, but with varying concentrations (Tables 6 and 7). Akin to Hart's intrusion-related model noted previously, these differences relate

to the proximity of the deposits to the core of the system, which in turn is related to temperature (proximal - Hislop, Ross; distal - Grey Fox).

As the tectonic regime reverted to compression and after subsequent burial, another mineralizing event occurred concurrent with the D₃ north-over-south shearing and folding (Black Fox). This event could have remobilized gold from the earlier intrusion-associated event, introduced new gold, or some combination of the two.

2.10.9 Syenite-associated deposits elsewhere in the Abitibi

Robert (2001) assigned a sub-classification, i.e., syenite-associated, for several of the gold deposits in the AGB due to their differences compared to the orogenic deposits in terms of vein types, alteration styles, mineralogy, elemental associations and inferred age of the intrusions and related mineralization (i.e., ca. 2680 Ma). One example is the Lightning Zone of the Holloway deposit (average grade of 5 g/t Au), which is located approximately 17 km west of the Ontario-Quebec border along the PDDZ (Fig. 1B). Similar to Grey Fox and Hislop, it is interpreted to be an intrusion-associated deposit and Ropchan et al. (2002) note the associated enrichment of S, As, and W with Au, the spatial association with alkaline intrusions, which they consider to be related to the mineralization, the coeval emplacement of these intrusions with the formation of the Timiskaming sedimentary basin, and the relatively early timing of mineralization, which is constrained by cross-cutting barren dykes dated at 2672 Ma. The Holloway deposits shares many additional similarities with Grey Fox and Hislop, including: 1) the presence of abundant variolitic, spherulitic, and hyaloclastite and/or autobrecciation textures in the host metavolcanic units; 2) a tholeiitic affinity of the host metavolcanics with an evolved chemistry (basalt to dacite-rhyolite); 3) an associated chlorite, carbonate (dolomite-ferrodolomite), muscovite, albite, and pyrite

alteration assemblage; and 4) a variation in the Fe# of both chlorite and carbonate phases with the host metavolcanic units. Unlike Grey Fox and Hislop, however, there is a strong deformation overprint at Holloway, and Ropchan et al. (2002) identified two mineralizing events - an early event (e.g., the Lightning Zone) that predates the post-Timiskaming return to compression and a syn-late event associated with the post-Timiskaming deformation.

2.10.10 Implications for exploration

The recognition of the Grey Fox and Hislop deposits as a distinct group related to a larger magmatic-hydrothermal system that occurred relatively early in the deformation history of the AGB has important implications for exploration:

1. As they form early in the deformation history and are related to coeval magmatic activity as opposed to structural channeling controlled by regional-scale events, there is potential for discovery of other similar deposits further away from the main breaks (i.e., PDDZ and CLLDZ).
2. Elevated metamorphic facies, particularly where overprinted by alteration, may be evidence of an increased geothermal gradient related to extensive magmatic activity with subsequent hydrothermal activity, akin to younger intrusion-related deposit settings in the Phanerozoic.
3. Competent units, in addition to rheologic contacts, deform in a brittle manner in shallow-level systems and therefore are preferential conduits for fluids; as such, they should be a focus of exploration.
4. Following from the previous point, emphasis should be placed on proper identification of rock types in an area, which may be ambiguous due to formation of chlorite and amphiboles

during metamorphism. Lithogeochemistry can be an excellent tool in these cases for distinguishing rock types, particularly with modern hand-held devices designed for such application.

5. Recognition of alteration and its relative timing (i.e., K-feldspar versus muscovite dominant versus carbonate-albite) can be used to guide exploration on a more general scale and can help vector towards the cores of these systems.
6. When alteration, but not mineralization, is intersected, Fe/Mg ratios (i.e., Fe#) may provide a powerful vectoring tool. This is not only reflected in whole-rock chemistry (present through SEM-EDS raster analyses here), but also through chlorite and carbonate mineral chemistry. Thus, the use of SWIR/XRD technology and chemical staining can be implemented as an immediate tool for exploration, which is already being done at Grey Fox.
7. These systems form multiple, discrete deposits in locally favorable hosts, so the occurrence of one deposit is an indication that more may be present.

2.11 CONCLUSIONS

Intrusion-associated Au deposits represent a distinct class of Au deposits in the AGB that differ from the well-described orogenic or greenstone-hosted quartz-carbonate vein-type deposits. Widespread alkali magmatism coeval with the deposition of the Timiskaming assemblage is involved in this metallogenic event, which represents a distinct setting during the tectonic evolution of the AGB. However, recognition of these deposits is complicated by their relatively early timing and subsequent overprinting by regional deformation during later orogenic events. The Hislop magmatic-hydrothermal system, which formed the Hislop and Grey Fox deposits, represents a rare well-preserved example of this early mineralization style that contrasts markedly

with the more typical orogenic-style Au mineralization, such as the nearby Black Fox deposit. The preservation of this type of mineralization provides the opportunity to further study and update aspects of the “syenite-associated” model. This work shows that different zones with distinct alteration histories and metal associations occur and provide convincing evidence for the variability within the ore system. Several key characteristics are outlined that highlight distinguishing features of this deposit style, most notably the preference for more evolved and competent host units, which reflect the comparatively shallow level of deposit formation. As such, proper identification of host rock units, as well as the identification of lithologic control on mineralization may provide a better constraint on the formation of more cryptic deposits that are masked by deformation (e.g., Holloway’s Lightning Zone). Recognition of this style of mineralization warrants further exploration locally outside of the well-explored regional PDDZ.

2.12 REFERENCES

- Akande, S.O., 1982, Mineralogy and Genesis of Three Vein Systems, Ross Mine, Holtvre, Ontario: Geology of Canadian Gold Deposits, v. Special Vo, p. 94–97.
- Arteaga, L.A., 2018, Spatial and temporal relationship between intrusive rocks and gold mineralisation in the Miller Dyke Complex , Abitibi greenstone belt , Ontario , Canada: Laurentian University, 123 p.
- Ayer, J., Thurston, P.C., Bateman, R., Dubé, B., Gibson, H.L., Hamilton, M.A., Hathway, B., Hocker, S.M., Houlé, M., Hudak, G.J., Ispolatov, V., Lafrance, B., Leshner, C.M., MacDonald, P.J., et al., 2005, Overview of results from the Greenstone Architecture Project: Discover Abitibi Initiative: v. OFR 6154, 146p. p.
- Bateman, R., Ayer, J.A., and Dubé, B., 2008, The Timmins-Porcupine gold camp, Ontario: Anatomy of an Archean greenstone belt and ontogeny of gold mineralization: Economic Geology, v. 103, p. 1285–1308, doi: 10.2113/gsecongeo.103.6.1285.
- Berger, B.R., 2002, Geological Synthesis of the Highway 101 Area, East of Matheson, Ontario 2002: Ontario Geological Survey, v. Open File, p. 124.
- Bleeker, W., 2015, Synorogenic gold mineralization in granite-greenstone terranes: the deep connection between extension, major faults, synorogenic clastic basins, magmatism, thrust inversion, and long-term preservation: Targeted Geoscience Initiative 4: Contributions to the Understanding of Precambrian Lode Gold Deposits and Implications for Exploration, (ed.) B. Dubé and P. Mercier-Langevin; Geological Survey of Canada, Open File 7852, p. 25–47, doi: 10.4095/296624.
- Böhlke, J.K., 1988, Carbonate-sulfide equilibria and “stratabound” disseminated epigenetic gold mineralization: a proposal based on examples from Alleghany, California, U.S.A.: Applied Geochemistry, v. 3, p. 499–516, doi: 10.1016/0883-2927(88)90022-4.
- Brisson, H., 2014, Technical Report on the Mineral Resource and Mineral Reserve Estimates for the Black Fox Complex: Unpublished report addressed to Primero Mining Corp.,.
- Cassidy, K., and Hagemann, S., 2000, Hagemann, S.G. & Cassidy, K.F., 2000, Archean orogenic lode gold deposits, in Gold in 2000, edited by S.G. Hagemann & P.E. Brown: Reviews in Economic Geology 13: 9-68., in p. 9–68.
- Cave, B.J., Large, R.R., White, C.E., and McKnight, S., 2017, Does tungsten availability control the presence of tungsten in turbidite-hosted orogenic gold mineralization? Evidence from the meguma and Bendigo-Ballararat Terranes: Canadian Mineralogist, v. 55, p. 973–999, doi: 10.3749/canmin.1600088.
- Chamberlain, C., Bath, A., Blackwell, J., Cooke, D., Henry, A., Jackson, M., Jago, P., Micko, J., Pass, H., Simpson, K., Tosdal, R., and Zukowski, W., 2008, Towards an integrated model for alkalic

- porphyry and epithermal deposits in British Columbia: Poster presentation, 2007 Exploration Roundup, Vancouver, B.C.,
http://www.geosciencebc.com/i/pdf/Roundup2007/2005-053%0A_2007Roundup.pdf.
- Chouinard, A., Paquette, J., and Williams-Jones, A.E., 2005, Crystallographic controls on trace-element incorporation in Auriferous pyrite from the Pascua epithermal high-sulfidation deposit, Chile-Argentina: *Canadian Mineralogist*, v. 43, p. 951–963, doi: 10.2113/gscanmin.43.3.951.
- Corbett, G., 2007, Controls to Low Sulphidation Epithermal Au-Ag mineralization:, Talk presented at a meeting of the Sydney Mineral Exploration Discussion Group (SMEDG) with powerpoint and text on SMEDG website www.smedg.org.au.
- Corfu, F., Krogh, T.E., Kwok, Y.Y., and Jensen, L.S., 1989, U–Pb zircon geochronology in the southwestern Abitibi greenstone belt, Superior Province: *Canadian Journal of Earth Sciences*, v. 53, p. 1747–1763, doi: 10.1139/e89-148.
- Cox, S.F., Knackstedt, M.A., and Braun, J., 2001, Principles of structural control on permeability and fluid flow in hydrothermal systems: *Economic Geology*, v. 14, p. 1–24.
- Dinel, E., Saumur, B.M., and Fowler, A.D., 2008, Spherulitic aphyric pillow-lobe metatholeiitic dacite lava of the Timmins area, Ontario, Canada: A new Archean facies formed from superheated melts: *Economic Geology*, v. 103, p. 1365–1378, doi: 10.2113/gsecongeo.103.6.1365.
- Downes, H., 2021, *Ultramafic Rocks*: Elsevier Inc., 69–75 p., doi: 10.1016/b978-0-12-409548-9.12478-9.
- Dubé, B., and Gosselin, P., 2007, Greenstone hosted quartz-carbonate vein deposits, in Goodfellow, W.D., ed., *Mineral Deposits of Canada: A synthesis of Major Deposit-Types, District Metallogeny, the Evolution of Geological Provinces, an Exploration Methods*: Geological Association of Canada, Mineral Deposits Division, v. Special Pu, p. 49–73.
- Dubé, B., and Mercier-Langevin, P., 2020, Gold Deposits of the Archean Abitibi Greenstone Belt, Canada: *Geology of the World's Major Gold Deposits and Provinces*, p. 669–708, doi: 10.5382/SP.23.32.
- Dubé, B., Mercier-Langevin, P., Ayer, J., Atkinson, B., and Monecke, T., 2017, Orogenic Greenstone-Hosted Quartz-Carbonate Gold Deposits of the Timmins-Porcupine Camp*: v. 19, 51–79 p., doi: 10.5382/Rev.19.02.
- Fayol, N., and Jébrak, M., 2017, Archean sanukitoid gold porphyry deposits: A new understanding and genetic model from the lac bachelor gold deposit, Abitibi, Canada: *Economic Geology*, v. 112, p. 1913–1936, doi: 10.5382/econgeo.2017.4534.
- Fowler, A.D., Berger, B., Shore, M., Jones, M.I., and Ropchan, J., 2002, Supercooled rocks: Development and significance of varioles, spherulites, dendrites and spinifex in Archaean volcanic rocks, Abitibi Greenstone belt, Canada: *Precambrian Research*, v. 115, p. 311–328, doi:

10.1016/S0301-9268(02)00014-1.

- Gelinas, A., 2012, Characterization and Comparison of Alteration Associated with Gold Mineralization in the Contact and 147 Zones of the Archean Black Fox Complex, Matheson Ontario: Unpublished undergraduate thesis, Laurentian University.
- Goldfarb, R.J., Baker, T., Dubé, B., Groves, D.I., Hart, C.J.R., and Gosselin, P., 2005, Distribution, Character, and Genesis of Gold Deposits in Metamorphic Terranes: Economic Geology 100th Anniversary Volume, v. 100, p. 407–450.
- Gourcerol, B., Kontak, D.J., Thurston, P.C., and Petrus, J.A., 2018a, Application of LA-ICP-MS sulfide analysis and methodology for deciphering elemental paragenesis and associations in addition to multi-stage processes in metamorphic gold settings: Canadian Mineralogist, v. 56, p. 39–64, doi: 10.3749/canmin.1700048.
- Gourcerol, B., Kontak, D.J., Thurston, P.C., and Petrus, J.A., 2018b, Results of LA-ICP-MS sulfide mapping from Algoma-type BIF gold systems with implications for the nature of mineralizing fluids, metal sources, and deposit models: Mineralium Deposita, v. 53, p. 871–894, doi: 10.1007/s00126-017-0788-7.
- Graham, J., and Morris, R.C., 1973, Tungsten- and antimony-substituted rutile: Mineralogical Magazine, v. 39, p. 470–473.
- Grant, J.A., 1986, The isocon diagram—a simple solution to Gresens' equation for metasomatic alteration.: Economic Geology, v. 81, p. 1976–1982, doi: 10.2113/gsecongeo.81.8.1976.
- Groves, D.I., Goldfarb, R.J., Gebre-Mariam, M., Hagemann, S.G., and Robert, F., 1998, Orogenic gold deposits: a proposed classification in the context of their crustal distribution and relationship to other gold deposit types: Ore Geology Reviews, v. 13, p. 7–27, doi: 10.1016/S0169-1368(97)00012-7.
- Groves, D.I., Goldfarb, R.J., Robert, F., and Hart, C.J.R., 2003, Gold deposits in metamorphic belts: Overview of current understanding, outstanding problems, future research, and exploration significance: Economic Geology, v. 98, p. 1–29, doi: 10.2113/gsecongeo.98.1.1.
- Harris, A.C., and Holcombe, R.J., 2014, Quartz vein emplacement mechanisms at the E26 porphyry Cu-Au deposit, New South Wales: Economic Geology, v. 109, p. 1035–1050, doi: 10.2113/econgeo.109.4.1035.
- Hart, C., 2005, Classifying, distinguishing and exploring for intrusion-related gold systems: The Gangue MDD Newsletter, p. 4–9, <https://www.gac.ca/chapters/gangue/Gang87.pdf>.
- Hart, C.J.R., 2007, Reduced Intrusion-related Gold Systems, *in* v. 2703, p. 95–112.
- Hart, C.J.R., and Goldfarb, R., 2005, Distinguishing intrusion-related from orogenic gold systems: New Zealand Minerals Conference Proceedings, p. 125–133, http://www.nzpam.govt.nz/cms/pdf-library/minerals/conferences-1/125_papers_48.pdf.

- Hart, C.J.R., McCoy, D.T., Goldfarb, R.J., Smith, M., Roberts, P., Hulstein, R., Bakke, A. a., and Bundtzen, T.K., 2002, Geology, exploration, and discovery in the Tintina gold province, Alaska and Yukon: *Economic Geology*, v. 9, p. 241–274.
- Hastie, E.C.G., Kontak, D.J., and Lafrance, B., 2020, Gold Remobilization: Insights from Gold Deposits in the Archean Swayze Greenstone Belt, Abitibi Subprovince, Canada: *Economic Geology*, v. 115, p. 241–277, doi: 10.5382/econgeo.4709.
- Haugaard, R., Della Justina, F., Roots, E., Cheraghi, S., Vayavur, R., Hill, G., Snyder, D., Ayer, J., Naghizadeh, M., and Smith, R., 2021, Crustal-Scale Geology and Fault Geometry Along the Gold-Endowed Matheson Transect of the Abitibi Greenstone Belt: *Economic Geology*, doi: 10.5382/econgeo.4813.
- Ispolatov, V., Lafrance, B., Dubé, B., Creaser, R., and Hamilton, M., 2008, Geologic and structural setting of gold mineralization in the Kirkland Lake-Larder Lake gold belt, Ontario: *Economic Geology*, v. 103, p. 1309–1340, doi: 10.2113/gsecongeo.103.6.1309.
- Jébrak, M., and Doucet, P., 2002, Geology and gold–molybdenum porphyry mineralisation of the Archean Taschereau–Launay plutons, Abitibi, Quebec: *Precambrian Research - PRECAMBRIAN RES*, v. 115, p. 329–348, doi: 10.1016/S0301-9268(02)00015-3.
- Jensen, E.P., and Barton, M.D., 2000, Gold Deposits Related to Alkaline Magmatism, *in* *Gold in 2000*, Society of Economic Geologists, doi: 10.5382/Rev.13.08.
- Jones, W.A., 1948, Ross Mine: Structural Geology of Canadian Ore Deposits: A Symposium; Canadian Institute of Mining and Metallurgy. Special Paper., p. 570–579.
- Jones, M.I., 1992, Variolitic Basalts: Relations to Archean Epigenetic Gold Deposits in the Abitibi Greenstone Belt: Unpublished master's thesis, University of Ottawa.
- Katz, L.R., 2016, Geology of the Archean Côté Gold Au (-Cu) intrusion-related deposit, Swayze greenstone belt, Ontario: Laurentian University, 347 p.
- Kerr, M.J., Hanley, J.J., Kontak, D.J., Morrison, G.G., Petrus, J., Fayek, M., and Zajacz, Z., 2018, Evidence of upgrading of gold tenor in an orogenic quartz-carbonate vein system by late magmatic-hydrothermal fluids at the Madrid Deposit, Hope Bay Greenstone Belt, Nunavut, Canada: *Geochimica et Cosmochimica Acta*, v. 241, p. 180–218, doi: 10.1016/j.gca.2018.08.030.
- Kirkland Lake Gold, 2021, Consolidated Mineral Reserve Estimate (Effective December 31, 2020); <https://www.kl.gold/our-business/resources-and-reserves/default.aspx> (accessed March 2021).
- Kontak, D.J., Dubé, B., and Benham, W.R., 2008, The Upper Beaver Project, Kirkland Lake Area: Investigation of a Syenite-Associated Copper-Gold Deposit with Magnetite-Epidote-Feldspar Alteration: Summary of Field Work and Other Activities 2008, Ontario Geological Survey, Open File Report 6226, v. 1, p. 12–1 to 12–12.

- Lacroix, A., 1920, Les Roches Éruptives du Crétacé Pyrénéen et la Nomenclature des Roches Éruptives Modifiées:
- Lafrance, B., 2015a, Geology of the orogenic Cheminis gold deposit along the Larder Lake – Cadillac deformation zone, Ontario: Canadian Journal of Earth Sciences, v. 52, p. 1093–1108, doi: [dx.doi.org/10.1139/cjes-2015-0067](https://doi.org/10.1139/cjes-2015-0067).
- Lafrance, B., 2015b, Structural and lithological controls on gold mineralization at the Cheminis mine : Implications for the formation of gold deposits along the Larder Lake - Cadillac deformation zone , Ontario can be traced from Val D ' Or , Quebec , to Matachewan , The ear: Geological Survey of Canada, v. Open File, p. 51–54.
- Lameyre, J., and Bowden, P., 1982, Plutonic rock types series: discrimination of various granitoid series and related rocks: Journal of Volcanology and Geothermal Research, v. 14, p. 169–186, doi: [10.1016/0377-0273\(82\)90047-6](https://doi.org/10.1016/0377-0273(82)90047-6).
- Lawley, C.J.M., Creaser, R.A., Jackson, S.E., Yang, Z., Davis, B.J., Pehrsson, S.J., Dubé, B., Mercier-Langevin, P., and Vaillancourt, D., 2015, Unraveling the Western Churchill Province Paleoproterozoic Gold Metallotect: Constraints from Re-Os Arsenopyrite and U-Pb Xenotime Geochronology and LA-ICP-MS Arsenopyrite Trace Element Chemistry at the BIF-Hosted Meliadine Gold District, Nunavut, Canada*: Economic Geology, v. 110, p. 1425–1454, doi: [10.2113/econgeo.110.6.1425](https://doi.org/10.2113/econgeo.110.6.1425).
- Van Lichtervelde, M., 2002, A syenite-hosted intrusion-related gold deposit at the Hislop mine: Unpublished undergraduate thesis, University of Waterloo.
- Lofgren, G., 1971, Spherulitic textures in glassy and crystalline rocks: Journal of Geophysical Research, v. 76, p. 5635–5648, doi: [10.1029/JB076i023p05635](https://doi.org/10.1029/JB076i023p05635).
- McCuaig, T.C., and Kerrich, R., 1998, P-T-t-deformation-fluid characteristics of lode gold deposits: Ore Geology Reviews, v. 12, p. 381–453, doi: [10.1016/S0169-1368\(98\)80002-4](https://doi.org/10.1016/S0169-1368(98)80002-4).
- McDivitt, J.A., Kontak, D.J., Lafrance, B., and Robichaud, L., 2018, Contrasting Fluid Chemistries, Alteration Characteristics, and Metamorphic Timing Relationships Recorded in Hybridized Orebodies of the Missanabie-Renabie Gold District, Archean Wawa Subprovince, Ontario, Canada: Economic Geology, v. 113, p. 397–420, doi: [10.5382/econgeo.2018.4555](https://doi.org/10.5382/econgeo.2018.4555).
- McEwen Mining, 2021a, ABOUT THE FOX COMPLEX:, <https://www.mcewenmining.com/operations/black-fox-complex/default.aspx> (accessed March 2021).
- McEwen Mining, 2021b, McEwen Mining: 2019 Full Year and Q4 Production Results:, https://s21.q4cdn.com/390685383/files/doc_news/archive/2021/20210311_q4_Operating_and_Financial_Results.pdf.

- Mériaud, N., and Jébrak, M., 2017, From intrusion-related to orogenic mineralization: The Wasamac deposit, Abitibi Greenstone Belt, Canada: *Ore Geology Reviews*, v. 84, p. 289–308, doi: 10.1016/j.oregeorev.2017.01.021.
- Mitrofanov, A., Selby, M., Martin, J., Machuca, D., Stubina, N., Fung, N., and Alexander, E., 2018, The Black Fox Complex, Canada: McEwen Mining Inc., NI 43-101 Technical Report, 268 p., https://s21.q4cdn.com/390685383/files/technical_reports/Ontario/20180406_tech_report_McEwen_BlackFox.pdf.
- Monecke, T., Mercier-Langevin, P., Dubé, B., and Hannington, M., 2017, Introduction: Archean Base and Precious Metal Deposits, Southern Abitibi Greenstone Belt, Canada (T. Monecke, P. Mercier-Langevin, & B. Dubé, Eds.): *Archean Base and Precious Metal Deposits, Southern Abitibi Greenstone Belt, Canada*, v. 19, p. 0.
- Murowchick, J.B., and Barnes, H.L., 1987, Effects of temperature and degree of supersaturation on pyrite morphology: *American Mineralogist*, v. 72, p. 24–1250, http://www.minsocam.org/ammin/AM72/AM72_1241.pdf.
- Nassif, M.T., Kuiper, Y.D., Goldfarb, R.J., Monecke, T., and Holm-Denoma, C.S., 2018, Structural evolution of a gold-bearing transtensional zone within the Archean Porcupine-Destor deformation zone, southern Abitibi greenstone belt, eastern Ontario, Canada: *Journal of Structural Geology*, v. 117, p. 203–218, doi: 10.1016/j.jsg.2018.09.012.
- Neyedley, K., Hanley, J.J., Fayek, M., and Kontak, D.J., 2017, Textural, fluid inclusion, and stable oxygen isotope constraints on vein formation and gold precipitation at the 007 deposit: , p. 629–660, doi: 10.2113/econgeo.112.3.629.
- Phillips, G.N., and Powell, R., 2010, Formation of gold deposits: A metamorphic devolatilization model: *Journal of Metamorphic Geology*, v. 28, p. 689–718, doi: 10.1111/j.1525-1314.2010.00887.x.
- Poulsen, K.H., Robert, F., and Dube, B., 2000, Geological classification of Canadian gold deposits: 1–106 p., doi: 10.1126/science.ns-6.149S.521-a.
- Rahaman, S., Mondal, M.E.A., Ahmad, I., Bhutani, R., and Choudhary, A.K., 2019, Geological Evolution of the Precambrian Indian Shield: Springer International Publishing, 327–350 p., doi: 10.1007/978-3-319-89698-4.
- Reich, M., Kesler, S.E., Utsunomiya, S., Palenik, C.S., Chryssoulis, S.L., and Ewing, R.C., 2005, Solubility of gold in arsenian pyrite: *Geochimica et Cosmochimica Acta*, v. 69, p. 2781–2796, doi: 10.1016/j.gca.2005.01.011.
- Ridley, J.R., and Diamond, L., 2000, Fluid chemistry of orogenic gold lode deposits and implications for genetic models: *Rev Econ Geol*, v. 13, p. 146–162.
- Robert, F., 2001, Syenite-associated disseminated gold deposits in the Abitibi greenstone belt, Canada:

- Mineralium Deposita, v. 36, p. 503–516, doi: 10.1007/s001260100186.
- Robert, F., Brommecker, R., Bourne, B., Dobak, P., McEwan, C., Rowe, R., and Zhou, X., 2007, Models and Exploration Methods for Major Gold Deposit Types: Proceedings of Exploration 07: Fifth Decennial International Conference on Mineral Exploration, v. 48, p. 691–711.
- Robert, F., and Poulsen, K.H., 2001, Vein Formation and Deformation in Greenstone Gold Deposits: Reviews in Economic Geology vol. 14; Structural Controls on ore genesis, p. 111–155.
- Robert, F., Poulsen, K.H., and Dube, B., 1997, Gold Deposits and Their Geological Classification: Proceedings of Exploration 97: Fourth Decennial International Conference on Mineral Exploration, p. 209–220.
- Rocque, P., Eng, P., Cater, D., and Geo, P., 2016, Hislop Property, Ontario, Canada Updated NI 43-101 Technical Report: Unpublished report addressed to Kirkland Lake Gold Inc., p. 78.
- Ropchan, J.R., Luinstra, B., Fowler, A.D., Benn, K., Ayer, J., Berger, B., Dahn, R., Labine, R., and Amelin, Y., 2002, Host-rock and structural controls on the nature and timing of gold mineralization at the Holloway mine, Abitibi subprovince, Ontario: Economic Geology, v. 97, p. 291–309, doi: 10.2113/gsecongeo.97.2.291.
- Rowins, S., Cameron, E.M., Lalonde, A.E., and Ernst, R.E., 1993, Petrogenesis of the late Archean syenitic Murdock Creek pluton, Kirkland Lake, Ontario: evidence for an extensional tectonic setting: Canadian Mineralogist, v. 31, p. 219–244.
- Seedorff, E., Dilles, J.H., Proffett John M., J., Einaudi, M.T., Zurcher, L., Stavast, W.J.A., Johnson, D.A., and Barton, M.D., 2005, Porphyry Deposits: Characteristics and Origin of Hypogene Features, *in* One Hundredth Anniversary Volume, Society of Economic Geologists, doi: 10.5382/AV100.10.
- Sibson, R.H., 1996, Structural permeability of fluid-driven fault-fracture meshes: Journal of Structural Geology, v. 18, p. 1031–1042, doi: 10.1016/0191-8141(96)00032-6.
- Sibson, R.H., Robert, F., and Poulsen, K.H., 1988, High-angle reverse faults, fluid-pressure cycling, and mesothermal gold-quartz deposits: Geology, v. 16, p. 551–555, doi: 10.1130/0091-7613(1988)016<0551:HARFFP>2.3.CO;2.
- Sillitoe, R.H., 2015, Epithermal paleosurfaces: Mineralium Deposita, v. 50, p. 767–793, doi: 10.1007/s00126-015-0614-z.
- Sillitoe, R.H., 2010, Porphyry copper systems: Economic Geology, v. 105, p. 3–41, doi: 10.2113/gsecongeo.105.1.3.
- Sunagawa, I., and Takahashi, K., 1955, Preliminary report on the relation between the 0(111) face of the pyrite crystals and its minor contents of arsenic: Geological Society of Japan, v. Bull. 6, p. 1–10.
- Troop, D.G., 1989, Geological Investigations of the Destor-Porcupine Deformation Zone East of Matheson: Summary of Field Work and Other Activities 1989, Ontario Geological Survey,

- Miscellaneous Paper 146, p. 136–143.
- Troop, D.G., 1986, Multiple orebody types and vein morphologies, Ross Mine, District of Cochrane: Summary of Field Work and Other Activities 1986, Ontario Geological Survey, Miscellaneous Paper 132, p. 413–420.
- Troop, D.G., 1985, Preliminary Report on Geology and Metasomatism at the Ross Mine and Vicinity, District of Cochrane: Summary of Field Work and Other Activities 1985, Ontario Geological Survey, Miscellaneous Paper 126, p. 320–325.
- Tuba, G., Kontak, D.J., Choquette, B.G., Pfister, J., Hastie, E.C.G., and van Hees, E.H.P., 2021, Fluid diversity in the gold-endowed Archean orogenic systems of the Abitibi greenstone belt (Canada) I: Constraining the PTX of prolonged hydrothermal systems: *Ore Geology Reviews*, p. 104221, doi: <https://doi.org/10.1016/j.oregeorev.2021.104221>.
- Whitney, D.L., and Evans, B.W., 2010, Abbreviations for names of rock-forming minerals: *American Mineralogist*, v. 95, p. 185–187, doi: 10.2138/am.2010.3371.
- Zukowski, W., Cooke, D.R., Deyell, C.L., McInnes, P., and Simpson, K., 2014, Genesis and exploration implications of epithermal gold mineralization and porphyry-style alteration at the endeavour 41 prospect, Cowal District, New South Wales, Australia: *Economic Geology*, v. 109, p. 1079–1115, doi: 10.2113/econgeo.109.4.1079.

2.13 TABLES

Mineral abbreviations after Whitney (2010)					
Albite	ab	Fuchsite	fuch	Nepheline	nph
Amphibole	amp	Gold	Au	Orthopyroxene	opx
Bastnäsité	bst	Hematite	hem	Plagioclase	pl
Calcite	cal	Hornblende	hbl	Pyrite	py
Carbonate	cb	K-feldspar	ksp	Quartz	qz
Chlorite	chl	Magnesite	mgs	Rutile	rt
Chromite	chr	Magnetite	mag	Talc	tlc
Clinopyroxene	cpx	Molybdenite	mol	Thorite	thr
Dolomite	dol	Monazite	mon	Titanite	ttn
Feldspar	fsp	Muscovite	ms	Xenotime	xtn

Table 1: Mineral abbreviations used to label microscope and SEM-EDS photomicrographs (Fig. 10-16, 18).

	wt%										
	SiO ₂	Al ₂ O ₃	Fe ₂ O ₃ *	FeO	CaO	MgO	Na ₂ O	K ₂ O	TiO ₂	MnO	LOI
Talc-carbonate	28.6	0.1	8.84	6.58	0.15	34.5	0.01	0.005	0.01	0.11	27.3
Chlorite-albite-carbonate	36.7	6.77	10.65	6.5	7.07	19.2	1.88	0.05	0.39	0.17	16.7
Fuchsite	38.4	4.94	7.81	6.43	3.64	17.75	1.04	0.81	0.23	0.11	24.5

	wt%		ppm							
	Total	C	Cr	Ni	Y	Zr	∑LREE	∑HREE	Au	Pb
Talc-carbonate	99.74	7.1	574	2850	0.23	0.7	0.983	0.11	0.002	0.29
Chlorite-albite-carbonate	99.9	3.76	1540	969	2.84	17.3	14.65	4.06	0.103	1.59
Fuchsite	99.53	6.51	1470	908	2.38	10.6	6.233	2.61	0.005	11.5

Table 2: Whole-rock lithochemistry for the three ultramafic samples from the Black Fox deposit. The chlorite-albite-carbonate and fuchsite altered samples have similar Al₂O₃, MgO, Cr, Ni, Y, and REE concentrations, which are vastly different from those of the talc-carbonate altered sample.

Sample	Deposit	Database	Rock	Comment
HP-020	Hislop	This Study	Intrusive - Syenite II	Phaneritic, red brick color
HPSW-007	Hislop	This Study	Intrusive - Syenite II	Phaneritic, red-pink
HPSW-011	Hislop	This Study	Intrusive - Syenite I	Porphyritic, purple color
HPSW-011Dup	Hislop	This Study	Intrusive - Syenite I	Duplicate
HPSW-013	Hislop	This Study	Intrusive - Syenite I	Porphyritic, purple color
883527	Hislop	Van Lichtervelde	Intrusive - Syenite I	
883539	Hislop	Van Lichtervelde	Intrusive - Syenite I	
883509	Hislop	Van Lichtervelde	Intrusive - Min Syenite	Mineralized
883510	Hislop	Van Lichtervelde	Intrusive - Min Syenite	Mineralized
883511	Hislop	Van Lichtervelde	Intrusive - Min Syenite	Mineralized
883532	Hislop	Van Lichtervelde	Intrusive - Min Syenite	Weakly mineralized
883533	Hislop	Van Lichtervelde	Intrusive - Min Syenite	Weakly mineralized
883524	Hislop	Van Lichtervelde	Intrusive - Syenite Clast	Clast in UM talc-chl-schist
883501	Hislop	Van Lichtervelde	Intrusive - Melanosyenite	
883502	Hislop	Van Lichtervelde	Intrusive - Melanosyenite	
883503	Hislop	Van Lichtervelde	Intrusive - Melanosyenite	
883528	Hislop	Van Lichtervelde	Intrusive - Melanosyenite	
883529	Hislop	Van Lichtervelde	Intrusive - Melanosyenite	
883530	Hislop	Van Lichtervelde	Intrusive - Melanosyenite	
883531	Hislop	Van Lichtervelde	Intrusive - Melanosyenite	
883535	Hislop	Van Lichtervelde	Intrusive - Melanosyenite	
883543	Hislop	Van Lichtervelde	Intrusive - Melanosyenite	
883544	Hislop	Van Lichtervelde	Intrusive - Melanosyenite	
883545	Hislop	Van Lichtervelde	Intrusive - Melanosyenite	
883502B	Hislop	Van Lichtervelde	Intrusive - Melanosyenite	
883528 rep	Hislop	Van Lichtervelde	Intrusive - Melanosyenite	Replicate
50481G	GFS	McEwan	Intrusive - Melanosyenite	Pervasive hem
50504G	GFS	McEwan	Intrusive - Melanosyenite	Pervasive hem
BFP-015	Black Fox	This Study	Intrusive - QFP	QFP in deformed UM (grey)
883515	Hislop	Van Lichtervelde	Intrusive - QFP	
883516	Hislop	Van Lichtervelde	Intrusive - QFP	
883517	Hislop	Van Lichtervelde	Intrusive - QFP	
883534	Hislop	Van Lichtervelde	Intrusive - QFP	Altered
883515 PD	Hislop	Van Lichtervelde	Intrusive - QFP	Duplicate
883534 rep	Hislop	Van Lichtervelde	Intrusive - QFP	Replicate
BFP-004	Black Fox	This Study	Intrusive - Albitized	Strongly altered intrusive
BFP-010L	Black Fox	This Study	Intrusive - Altered	Strongly altered intrusive
50567G	GFS	McEwan	Intrusive - Other	Described as "tonalite"
163298	147 Zone	McEwan	Intrusive - Other	Described as "felsic"

Table 3: (continued on next page)

Sample	LOI %	C %	Au ppm	SiO ₂ %	Norm. Quartz	Norm. Orthoclase	Norm. Albite	Norm. Anorthite	Norm. Nepheline	Σ qz, fsp, nph
HP-020	1.27	0.36	0.16	63	1.87	55.93	32.80	4.50	0.00	95%
HPSW-007	1.93	0.48	0.141	63.3	0.00	35.34	54.93	2.60	0.79	94%
HPSW-011	1.01	0.12	0.09	64.8	0.00	31.31	56.20	1.17	1.28	90%
HPSW-011Dup	1.28	0.21	0.109	64.5	0.00	35.06	52.15	2.03	1.39	91%
HPSW-013	2	0.07	0.116	59.6	0.00	65.76	26.48	0.93	0.00	93%
883527	1.24	NA	0.068	64.97	0.00	5.16	86.87	3.60	0.40	96%
883539	3.18	NA	0.04	64.08	0.00	3.08	85.11	0.24	1.61	90%
883509	7.02	NA	11.2	58.97	1.79	4.99	70.68	0.45	0.00	78%
883510	9.78	NA	27.1	56.64	6.67	3.21	58.84	0.00	0.00	69%
883511	8.66	NA	8.65	63.87	25.94	1.17	45.60	0.22	0.00	73%
883532	4.51	NA	0.752	59.12	0.00	42.52	40.08	3.24	1.96	88%
883533	5.95	NA	0.562	62.36	7.02	11.52	63.77	0.72	0.00	83%
883524	14.46	NA	0.001	40.86	0.00	4.28	17.57	2.30	22.39	47%
883501	4.74	NA	0.082	55.5	0.00	22.85	50.29	4.97	5.09	83%
883502	5.93	NA	0.282	52.41	0.00	24.86	37.89	5.47	8.55	77%
883503	4.83	NA	0.015	54.49	0.00	36.19	32.38	5.94	6.75	81%
883528	6.76	NA	0.219	51.19	0.00	38.95	22.10	3.38	10.32	75%
883529	9.01	NA	1.22	49.1	0.00	21.91	28.28	2.03	15.18	67%
883530	6.84	NA	0.81	52.59	0.00	33.78	28.42	4.06	9.95	76%
883531	7.13	NA	0.382	53.37	0.00	34.25	31.85	2.78	6.59	75%
883535	5.97	NA	0.166	49.24	0.00	48.53	7.09	8.88	9.86	74%
883543	4.46	NA	0.011	54.68	0.00	32.80	37.08	6.05	5.58	82%
883544	4.94	NA	0.1	54.05	0.00	26.80	37.80	5.63	8.66	79%
883545	3.84	NA	0.02	54.54	0.00	37.29	33.03	5.29	6.29	82%
883502B	7.09	NA	0.975	52.8	0.00	15.97	45.85	1.81	10.89	75%
883528 rep	6.76	NA	NA	51.28	0.00	39.33	21.73	3.22	10.62	75%
50481G	3.75	1.29	0.02	53	0.00	19.97	40.93	7.35	9.28	78%
50504G	3.34	1.03	0.01	53.8	0.00	11.31	52.19	10.39	8.08	82%
BFP-015	1.23	0.06	0.081	72.6	24.89	9.23	61.18	0.71	0.00	96%
883515	2.3	NA	0.008	71.91	21.67	1.85	69.29	0.70	0.00	94%
883516	2.35	NA	0.001	71.55	20.61	1.98	70.24	0.16	0.00	93%
883517	2.77	NA	0.028	73.72	23.97	1.93	56.81	6.26	0.00	89%
883534	2.11	NA	0.071	71.59	18.66	2.27	72.92	0.37	0.00	94%
883515 PD	2.25	NA	0.011	71.37	21.26	1.73	69.22	0.70	0.00	93%
883534 rep	2.52	NA	0.127	67.59	8.78	2.89	80.16	0.23	0.00	92%
BFP-004	11.55	3.31	0.449	54.8	1.57	1.47	57.41	1.08	0.00	62%
BFP-010L	8.38	2.85	0.032	52.3	0.00	0.78	51.68	0.91	12.26	62%
50567G	3.02	1.03	0.19	48.1	4.43	9.86	23.52	24.89	0.00	63%
163298	13.8	3.24	0.06	44.3	0.00	7.65	37.44	14.15	0.00	59%

Table 3: (Description on next page)

Table 3: Sample information for felsic intrusions at Hislop, Grey Fox, and Black Fox. Results for normative mineralogy calculations shown for select phases.

A Major minerals				
	<i>Contact Zone Mafics</i>	<i>Contact Zone Sediments</i>	<i>147 Zone mafic-intermediates</i>	<i>South Zone felsics</i>
Interpreted protolith	Cpx/opx, pl, Ti-mag/ilm	Clay, qz, py	Pl, cpx/opx, ilm and mag	Qz, feldspr (ab-pl or ksp?)>>mafic phases
Least Altered	Amp, pl +/- ab, lcx, mag, ap	N/A	Amp, pl, mag, ilm, qz, ab, ap, rt, ttn	N/A
Chlorite-albite-quartz	Chl, qz, ab, pl, rt, ap, mag	Ab, qz, py1, chl, cal, rt, ap	Chl, qz, ab, mag, ap, ttn	Ab, qz, chl, bst
Albite-carbonate	Ab, cb, chl, rt, ap	Ab, cb, qz, py2, rt	Ab, cb, qz, rt, sid?, ap +/- Au-py	Ab, qz>cb, >>>rt +/- Au-py
Muscovite-quartz	Ms, hem, qz, cb, chl, ab, ap, rt, brt, +/- Au-py	Ms, chl, qz, cb, ap, rt, brt, hem, +/- Au-py(3)	Ms>chl, qz, rt, ap, sid?, mag?, hem? +/- Au-py	Ms, chl, rt, qz, mol, xtm, mon +/- sid, mon, Au-py,
Fe-rich chlorite	Chl, cb, hem, qz, ms, ab, rt, aug? +/- Au-py			
Ksp		Ksp, qz, py(3) (clast in CK-078B)	Ksp, cal, chl, ab +/- Au, Au-py	

B Sulfides and trace minerals				
	<i>Contact Zone Mafics</i>	<i>Contact Zone Sediments</i>	<i>147 Zone</i>	<i>South Zone</i>
Chlorite-albite-quartz	+/- py, ccp, po	py +/- ccp	py	py, bst, xtm (1), Cu (1)
Albite-carbonate	py +/- ccp, po, mon	py +/- ccp po, gld, mon	py, ccp, mon,	mon (alt not well expressed)
Muscovite-quartz	py, cob, gal, ccp, mon, xtm	py, ccp, po, mol, sph, gal, gld, mon	py, mol, cob, all, sph, apy, sch (1) xtm, mon?, gld	py, xtm, mon, xtm, zrn?, ccp, mol (ass/w vein?), gld, min gal-sph
Fe-rich chlorite	py, cob, gal, ccp, po, mon			
Ksp		py, ccp, mol, sph, mon?	py, sch, sph, gal, apy, xtm	

Table 4: Summary of major minerals (A) and sulphides/trace minerals (B) present in each alteration assemblage in the different zones of the Grey Fox deposit. The dominant minerals in each alteration assemblage are bolded.

	Felsic Metavolcanics	Mafic Metavolcanics	Ultramafic Metavolcanics	Syenite (I)	Syenite (II)
Interpreted protolith	Cpx, fsp, Ti-Fe oxide	Cpx, opx, pl, Ti-mag/ilm	Cpx/opx, pl, chr	Ksp, pl, bt?	Ksp, pl, bt?
Potassic	Cpx, ksp, hem, chl, ap, ttn, ms, bt	Hbl, chl, ep, pl, ms, mag, ab, ksp, mag, ilm, ap, ep	Ksp, cb, fuch	Ksp, ser, bt, cb, ap, qz	Ksp, ab, cb, chl, qz, py, mnz, rt, hem, thr
Sodic-carbonate	Ab, cb, qz, py, chl, rt, ap, mnz, xtm,	N/A	N/A	Ab, qz, cb	N/A

Table 5: Summary of minerals present in the different alteration assemblages of the main units at the Hislop deposit. The dominant minerals in each alteration assemblage are bolded. Please note that the syenites and ultramafic metavolcanics were not studied in the same detail as the felsic and mafic metavolcanics.

	<u>Major metal additions</u>	<u>Minor Metal Additions</u>
Grey Fox - muscovite	Au, As, Mo, W, Pb, Sb, Be, Cs, In	U, Ag, Re (?), Cu, Ba, Tl
Grey Fox - Fe-rich chlorite	Au, As, Mo, W, Pb, Re (?), Se, Bi, Li, Zn, LREE	U, Ag, Cu, V, Ga, Sn, Th
Hislop - K-feldspar	Au, As, W, Pb, U, Be, Tl, Te	Mo, Ag, Ba, Sb, Se, V, Ga, Y, HREE
Hislop - Albite	Au, Mo, W, Ag	U, As, Pb, Re (?), Bi

Table 6: Metal additions determined through isocon diagrams for each alteration assemblage at Grey Fox and Hislop, which is consistent with the pyrite laser ablation maps. Elements in bold are consistent between all the deposits.

	Mineralization Type	Host	Veining	Alteration minerals	Au:Ag	Additional metals	Source(s)
Hislop	Intrusion halo	ultramafic, mafic, and felsic metavolcanics syenite intrusive	Carbonate	K-feldspar, carbonate, muscovite, hematite	1:0.85*	Mo	present study Rocque (2016)
	Vein-associated: breccia, conjugate sets	Felsic flow-top metavolcanics, syenite intrusion	Quartz>>carbonate	Albite, quartz, carbonate, hematite, rutile, pyrite, chlorite	1 : 5.9*	Mo, Ag, Te	present study Rocque (2016)
Grey Fox	Vein-associated: breccia and crustiform; conjugate sets	Felsic and intermediate flow-top metavolcanics; contact between mafic metavolcanics and metasedimentary rocks	Quartz, carbonate, quartz-carbonate	Sericite, chlorite (Fe-rich), carbonate (Fe-rich), quartz pyrite, hematite>>barite, thorite. Albite, Mg-carbonate in barren zones	1 : 0.2-0.44* ~1 : 0.1-0.4†	Mo	present study Brisson (2014)
Ross	Vein-associated: breccia and crustiform (?)	Andesitic tuff, syenite stock (margin). Debated if it is a felsic fragmental rock(?), mafic volcanic, or sedimentary.	Dolomite, ankerite, calcite, and quartz. Carb>>quartz	Sericite, carbonate (Fe-rich?), silica, chlorite, hematite, anhydrite, gypsum, pyrite, albite, epidote	1 : 1.2 1 : 1.94	Ag, Cu Te?	Jones (1948) Akande (1982) Troop (1985 and 1986) Berger (2002)
Gibson	Vein-associated (breccia?)	Brecciated contact between syenite and basaltic rocks	Quartz	N/A	N/A	N/A	Troop (1989)
Royal Oak	Vein-associated	Variolitic flows	Quartz?	Carbonate, sericite, silicification, pyrite	N/A	N/A	Brisson (2014) Osisko Mining website

Table 7: Summary of mineral deposits in the Hislop Township that may have formed as part of the Hislop magmatic-hydrothermal event. *Au:Ag ratio from whole-rock analysis, this study †Au:Ag ratio from whole-rock analysis, McEwan Mining, with the 1 : 0.1 determined from the lower limit of the Au : Ag trend on the bivariate plot (Fig. 22), and the 1 : 0.4 from the average ratio of Au : Ag, for grades greater than ~ 1 gpt Au.

2.14 FIGURES

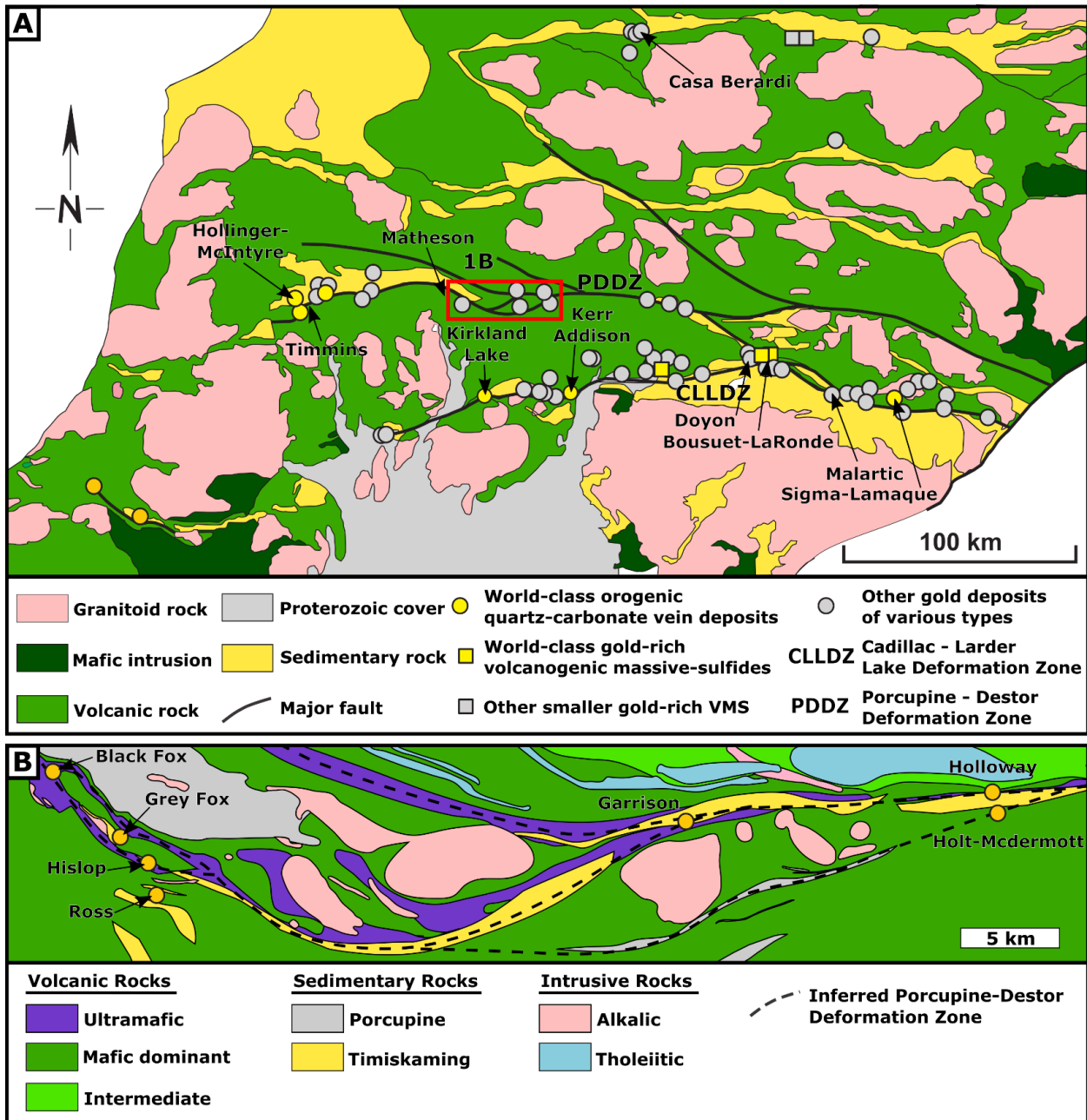


Figure 1: Geology and distribution of gold deposits in the southern Abitibi greenstone belt. **A.** Simplified geology modified from Dubé and Gosselin (2007). Note the spatial correlation between significant gold deposits and major structural corridors, e.g., the Porcupine-Destor (PDDZ) and Cadillac-Larder Lake Deformation (CLLDZ) zones. **B.** Simplified geology of the study area (modified after Berger et al., 2001). Locations of mines and advanced exploration projects indicated.

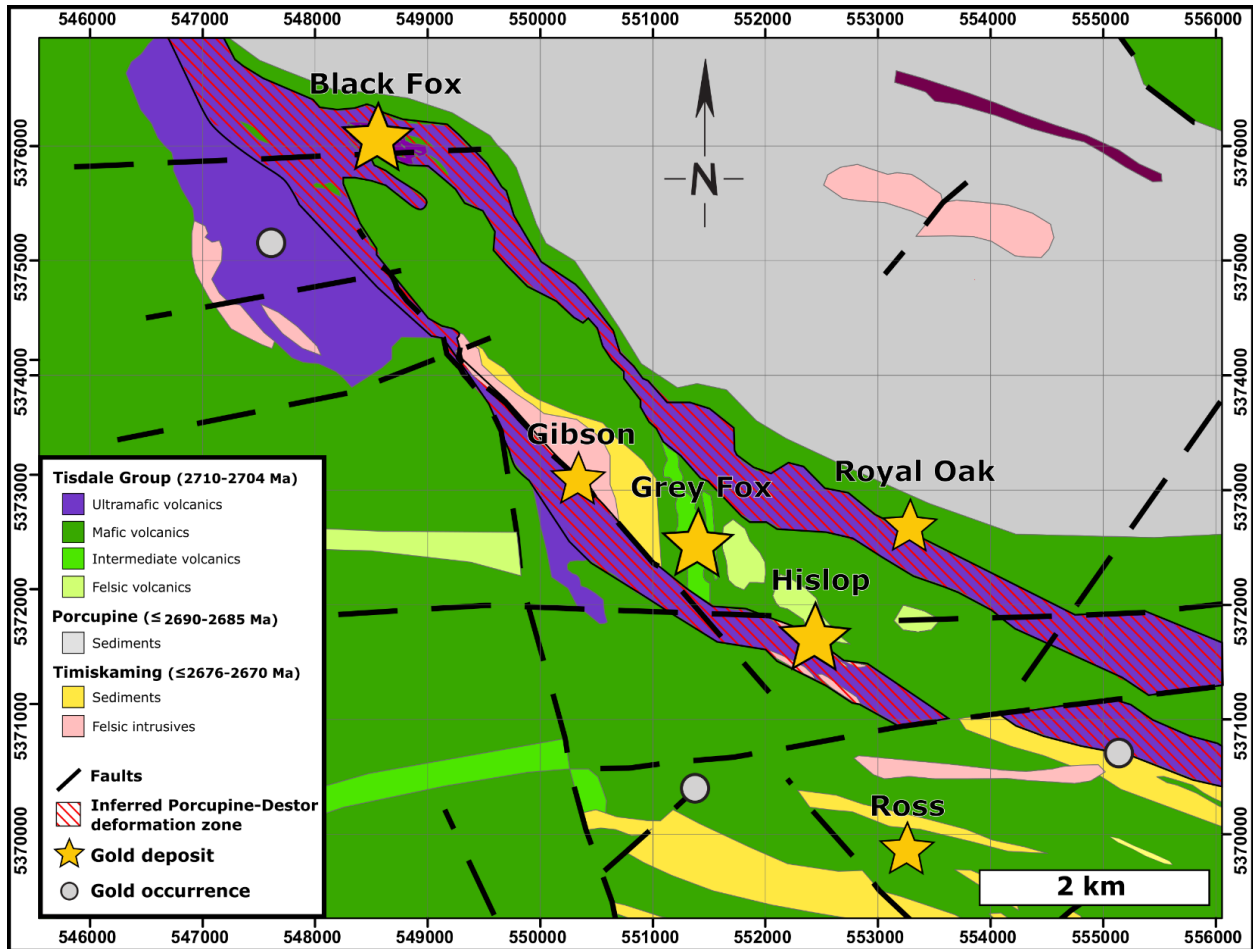


Figure 2: Simplified geology of the Hislop Township with locations of the studied deposits (Hislop, Grey Fox, Black Fox) as well as historical gold mines and occurrences in the vicinity (Ross, Royal Oak, Gibson). Note that three mineralized zones are present at Grey Fox, Contact, 147, and South, which are described schematically in Fig. 3. Geographic coordinate system is NAD 83 – UTM Zone 17. (Modified after Berger et al., 2001.)

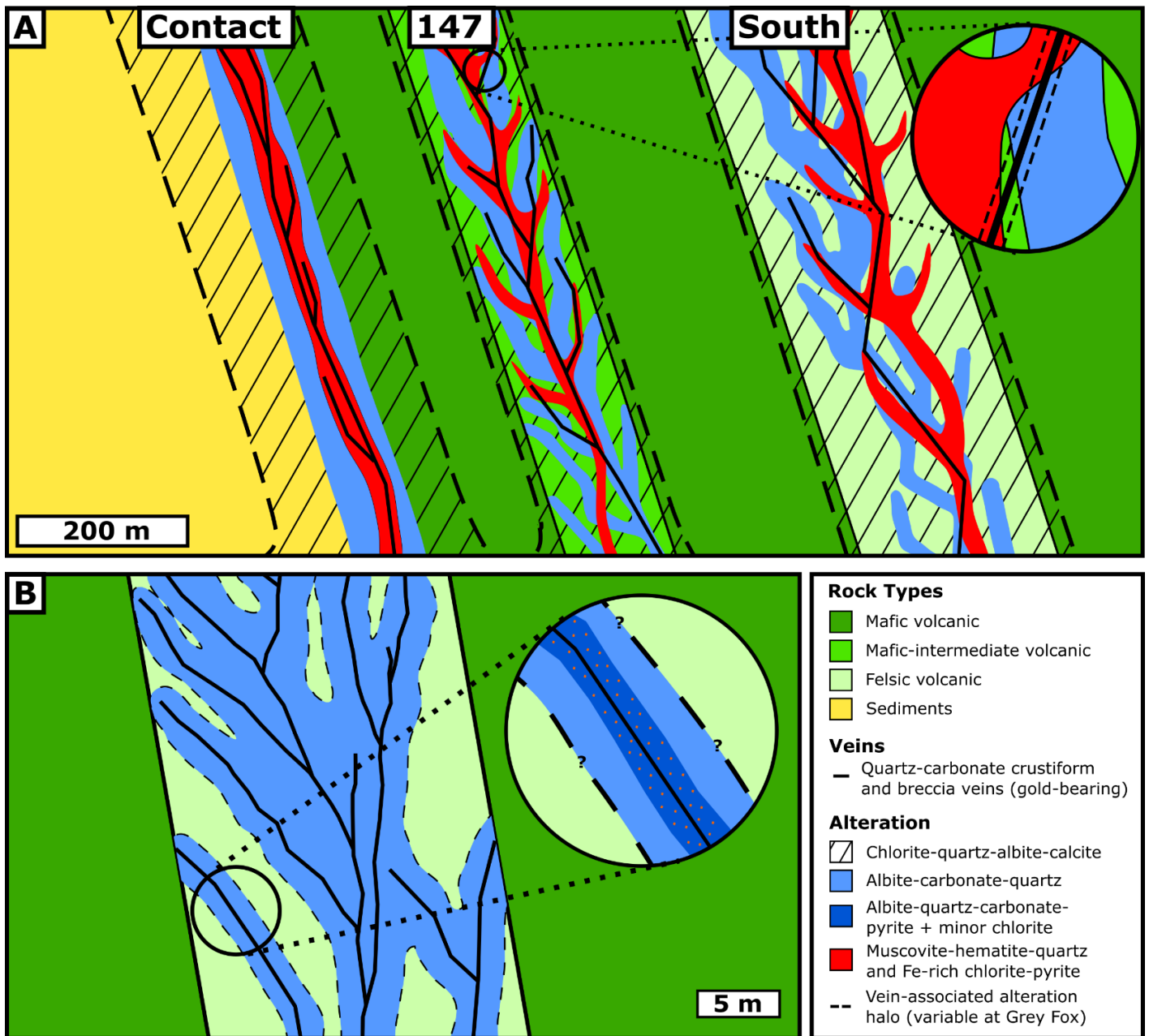


Figure 3: General geology and mineralization features of the Grey Fox and Hislop deposits – not to scale. **A.** Generalized cross-section of the Grey Fox deposit showing the three main mineralized zones (Contact, 147, and South) which reflects three distinct pathways during mineralization. The inset demonstrates the temporal and spatial relationship between the alteration assemblages and veining at the deposit. **B.** Schematic representation of the observed mineralization in the north wall of the Hislop open pit, where auriferous veins preferentially occur in the felsic metavolcanics unit. The inset shows the progressive alteration halo to the vein with pyrite related to the gold deposition developed proximal to the vein.

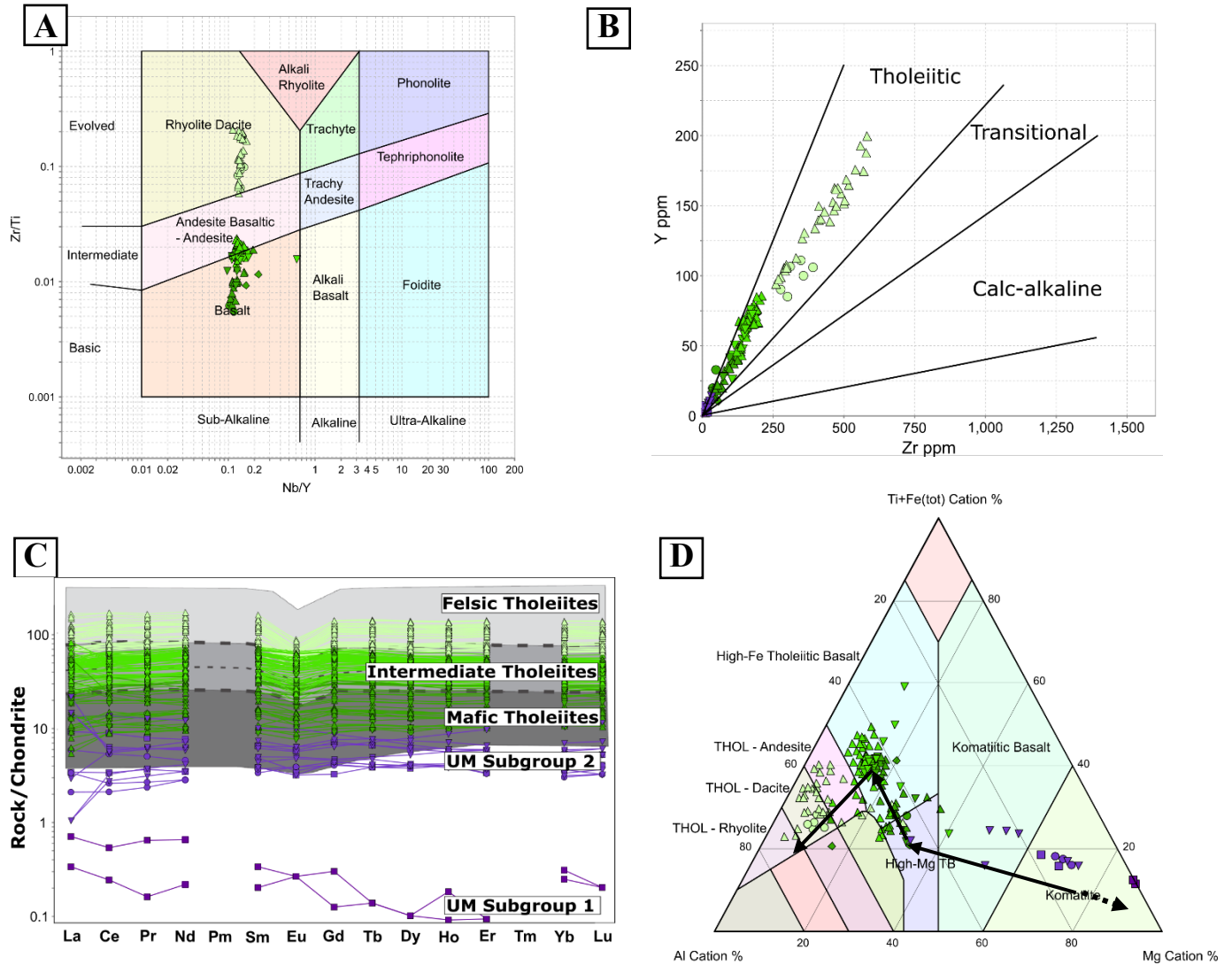


Figure 4: Discrimination diagrams of metavolcanic units from Hislop, Grey Fox, and Black Fox; note the clustering of the data. **A.** Pearce diagram showing all metavolcanic units plotting as sub-alkaline and defining a linear trend. **B.** A magmatic affinity diagram by Barrett and MacLean (1994) showing that all samples plot within the tholeiitic field along a linear trend. **C.** Chondrite-normalized REE diagram (using normalizing values of Sun and McDonough, 1989) of Dinel (2008) for Tisdale metavolcanics; note the conformity for the felsic, intermediate, and mafic metavolcanics, as well as the distinct separation for the ultramafic metavolcanics subgroups 1 and 2. **D.** Jensen Cation Plot with samples showing typical tholeiitic trend.

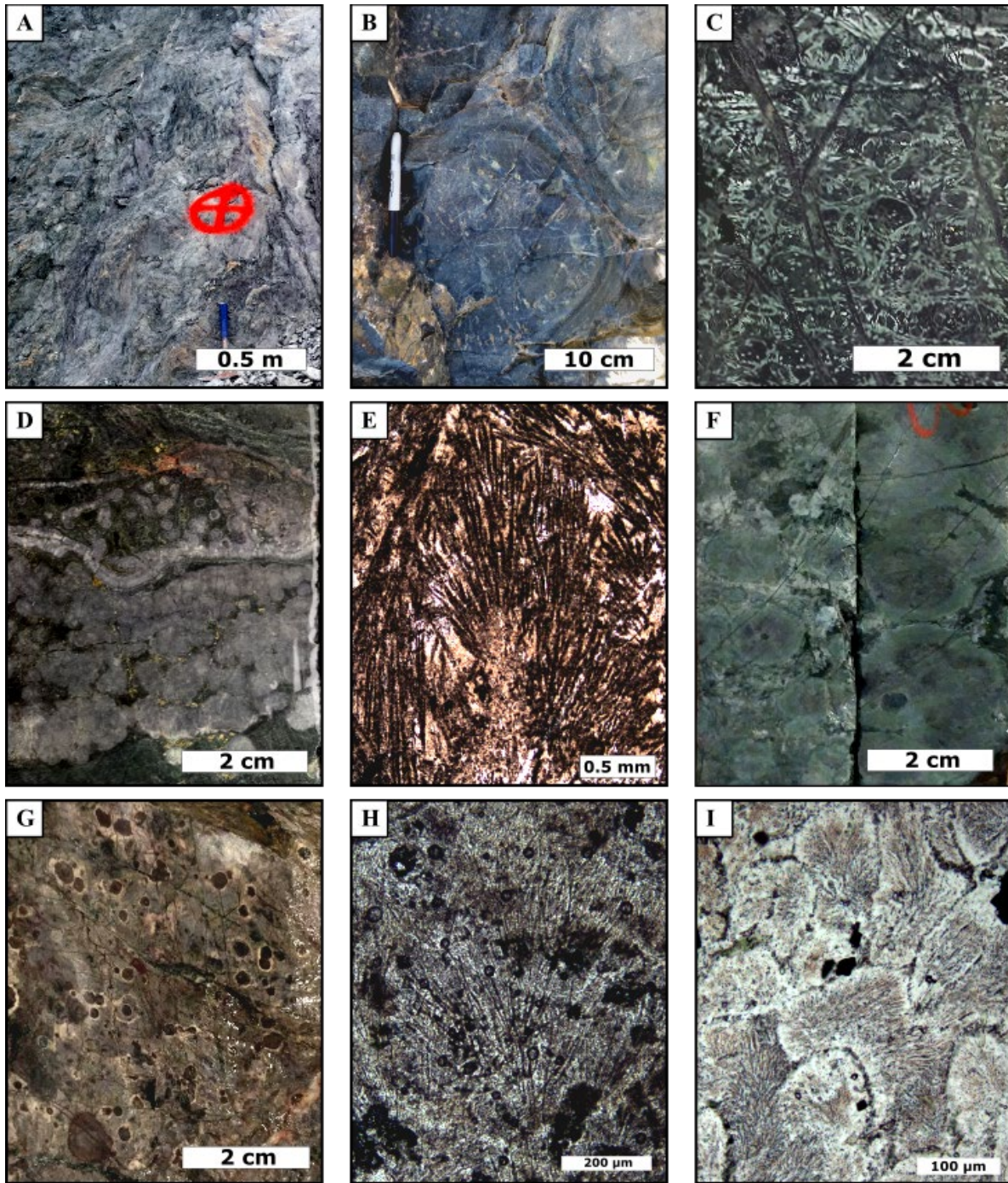


Figure 5: Macro- and micro-textural features of metavolcanic units at Grey Fox and Hislop seen in outcrop (A, B), core (C, D, E), cut hand sample (H), and photomicrographs in plane polarized light (E, H, I). **A.** Sheared ultramafic unit from Hislop. **B.** Pillowed mafic metavolcanic unit from Hislop. **C.** Hyaloclastite from intermediate metavolcanics, Grey Fox 147 Zone. **D.** Spherulites in the intermediate metavolcanics, Grey Fox 147 Zone. **E.** Residual spherulitic micro-textures of altered intermediate metavolcanics, Grey Fox 147 Zone. **F.** Spherulites in the felsic metavolcanics, Grey Fox South Zone **G.** Amygdules in a spherulitic matrix from the felsic metavolcanics, Hislop. **H.** Spherulitic micro-texture in altered felsic metavolcanics, Grey Fox South Zone. **I.** Spherulitic micro-texture in the matrix of the Hislop felsic metavolcanics; sample corresponds to G.

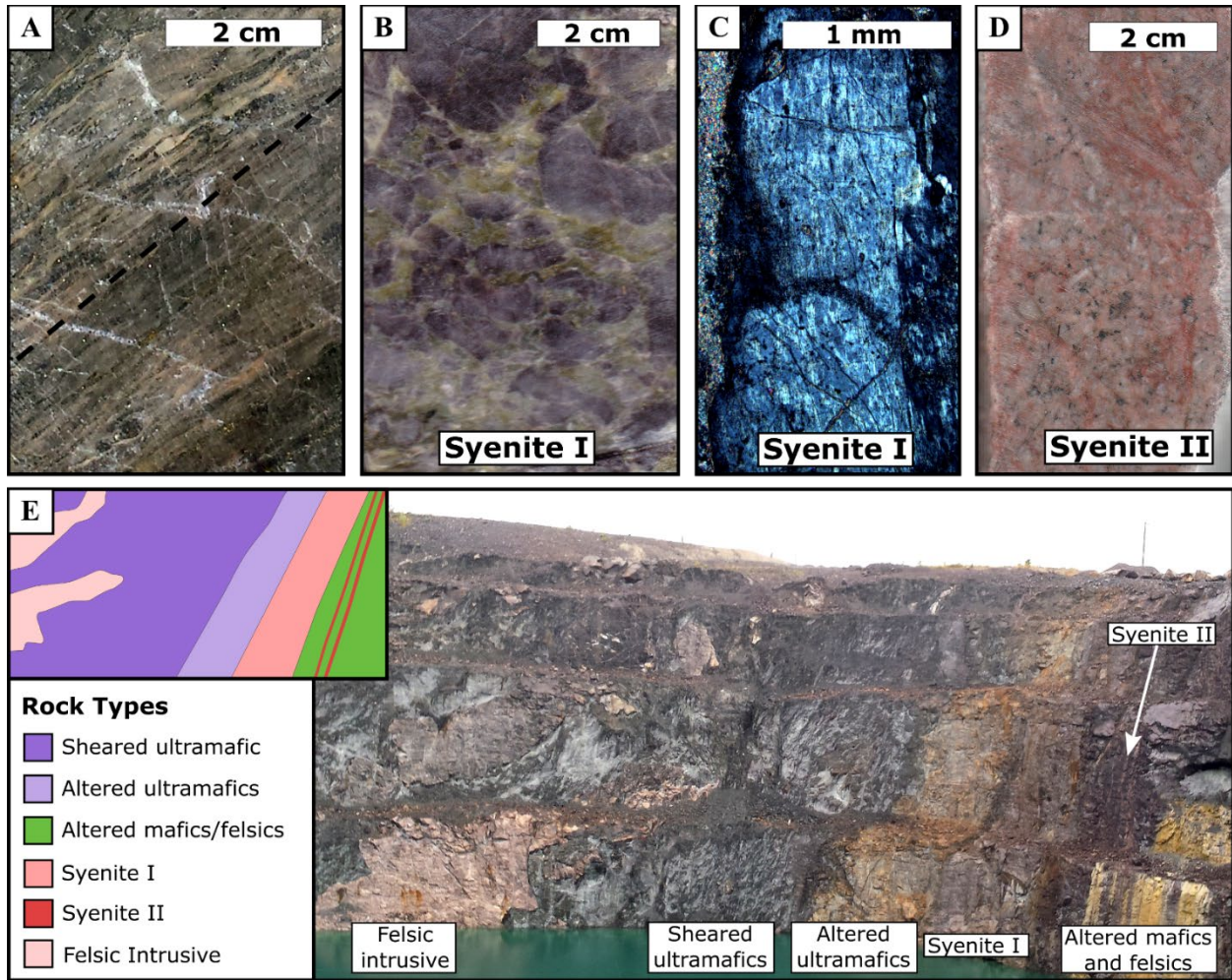


Figure 6: Additional rock units from the Grey Fox and Hislop deposits. **A.** Altered sediments from the Grey Fox Contact Zone with bedding parallel to a strong foliation (dashed line). **B.** Porphyritic syenite intrusion, as seen at the center of the Hislop deposit, with coarse, purple K-feldspar and muscovite-altered matrix. **C.** Photomicrograph in crossed nicols of perthitic feldspar from Hislop. **D.** Equigranular, moderately altered syenite with K-feldspar and hematite-stained albite from Hislop. **E.** The SW wall of the Hislop pit with mafic and felsic metavolcanics to the N (right on image), ultramafics to the S, and the Syenite I intrusive along the contact with a strong alteration visible in the ultramafics. Schematic inset in the upper left shows the distribution of the rock types.

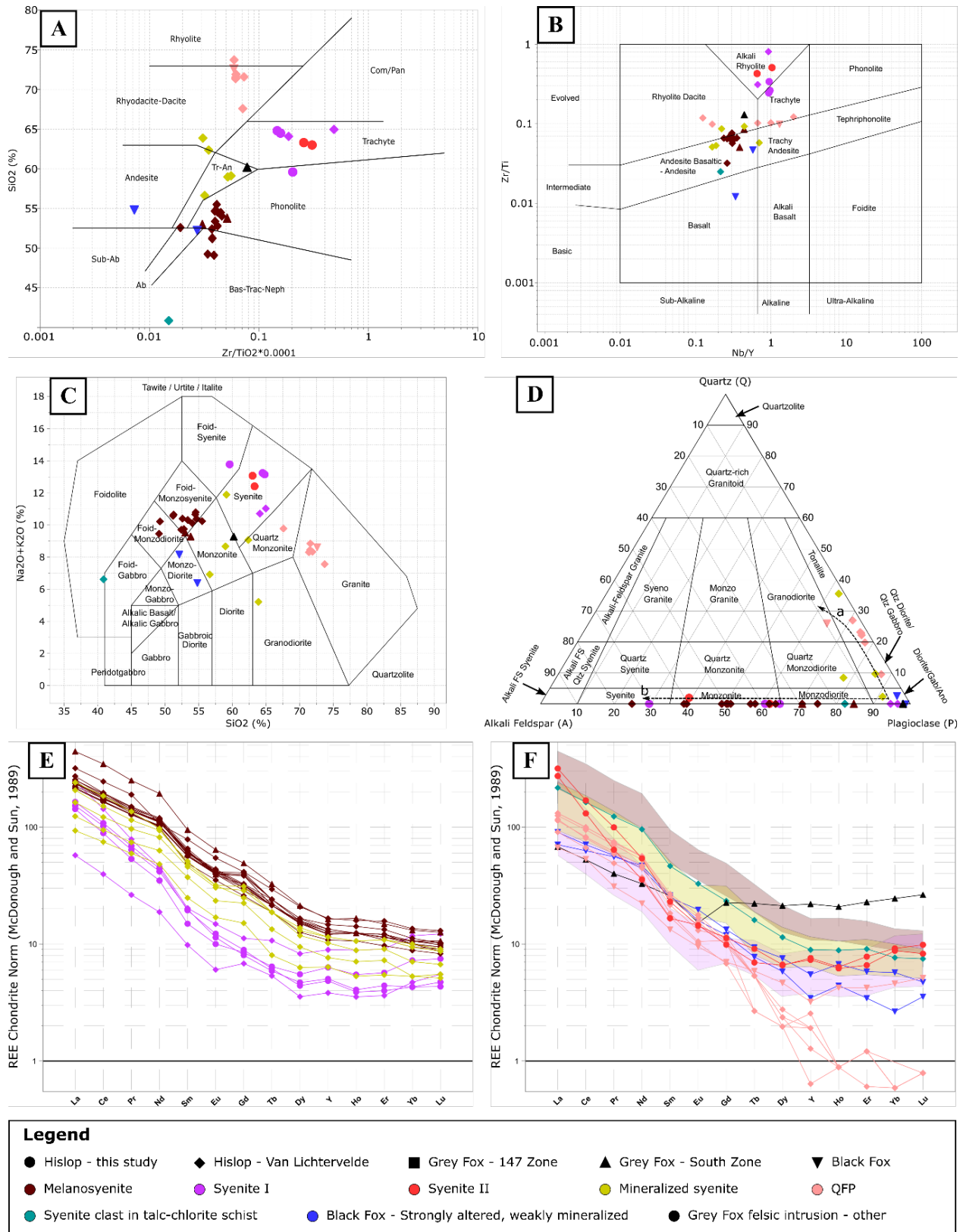


Figure 7: (Description on next page)

Figure 7: Chemical discrimination diagrams for felsic intrusions at Hislop, Grey Fox, and Black Fox. **A.** Zr/TiO₂ after Winchester & Floyd (1977) showing the low silica nature of the syenite and melanosyenite relative to the QFP. **B.** Pearce diagram exhibiting evolved nature of syenite intrusions. **C.** Total alkali versus silica diagram after Middlemost (1994). **D.** QAP diagram based on calculated normative mineralogy; note the distinct trends of the QFP and syenite/melanosyenite suites, which reflect calc alkaline (a) and alkaline/peralkaline (b) trends respectively (Lameyre and Bowden, 1982; Rahaman et al., 2019). **E.** REE diagram for the syenites and melanosyenites; note the overall similar profiles but the relatively lower intermediate REE for the non-mineralized syenites **F.** REE plot for remaining felsic intrusive units with fields for groups in E. Note the similar profile for the Syenite II as Syenite I and the similar profiles for the mineralized intrusions from Black Fox to the mineralized syenites. Additionally, note the stronger slope of the QFP units.

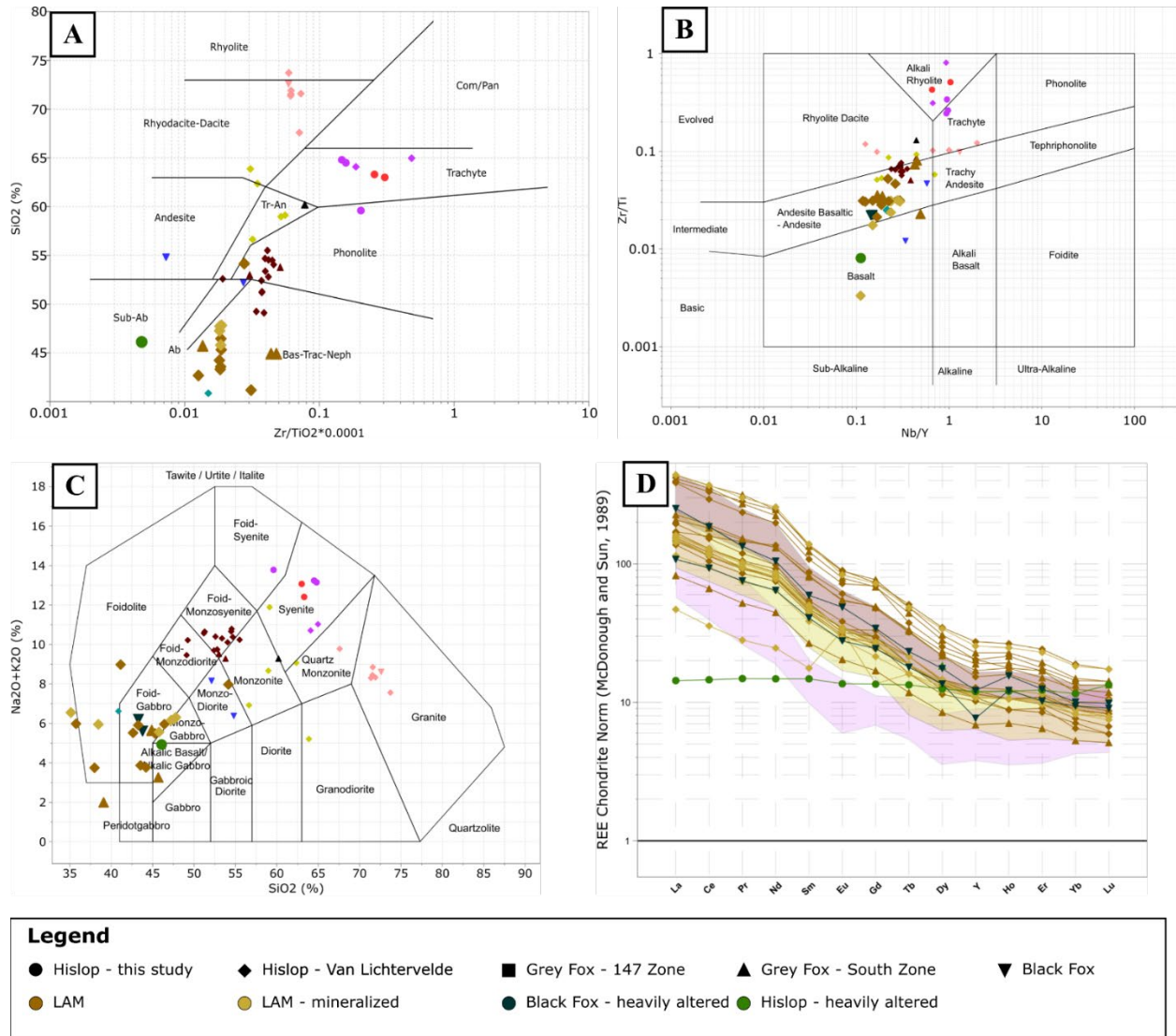


Figure 8: Chemical discrimination diagrams for lamprophyres (LAM). Data from Figure 7 are included for references as smaller points in A-C, see Figure 7 for legend. **A.** Zr/TiO₂ after Winchester & Floyd (1977) showing the lower silica and Zr/TiO₂ nature of the LAM relative to the felsic intrusions. **B.** Pearce diagram exhibiting less evolved nature of LAMs. **C.** Total alkali versus silica diagram after Middlemost (1994). **D.** REE diagram; note similar profile of LAM to the melanosyenite field.

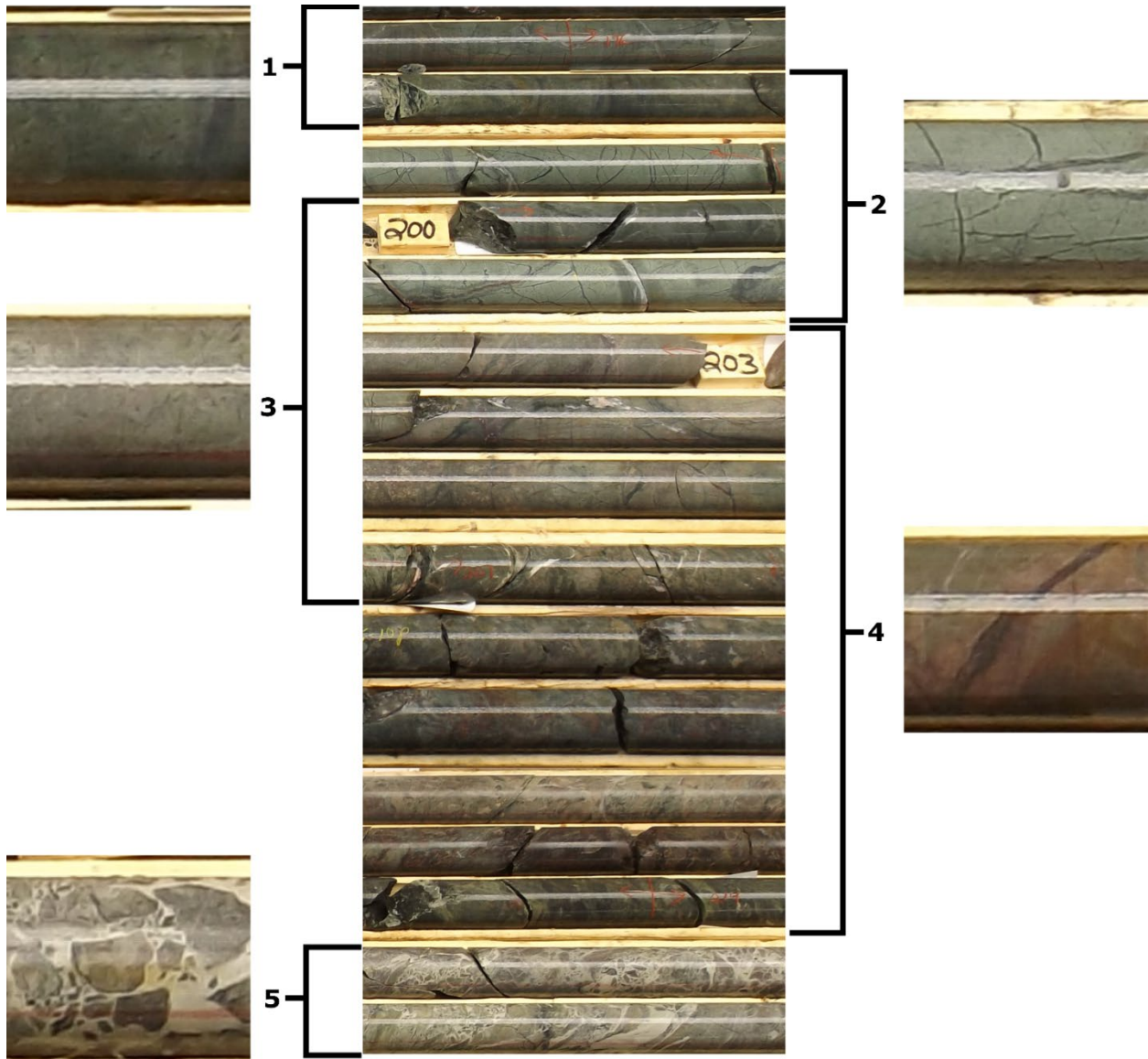


Figure 9: Core photos showing the Grey Fox Contact Zone with different zones of alteration and veining outlined as follows: **1.** Least altered; **2.** Chlorite-albite-quartz alteration; **3.** Sodic-carbonate alteration; **4.** Muscovite-chlorite alteration; and **5.** The breccia vein zone, which is present at the contact between the mafic metavolcanic (above) and metasedimentary (below) rocks. A gradational contact is observed between alteration 2 and 3, whereas alteration 4 overprints the precursor alteration with significant spatial overlap. Note that similar features are present in the three zones at the Grey Fox deposit.

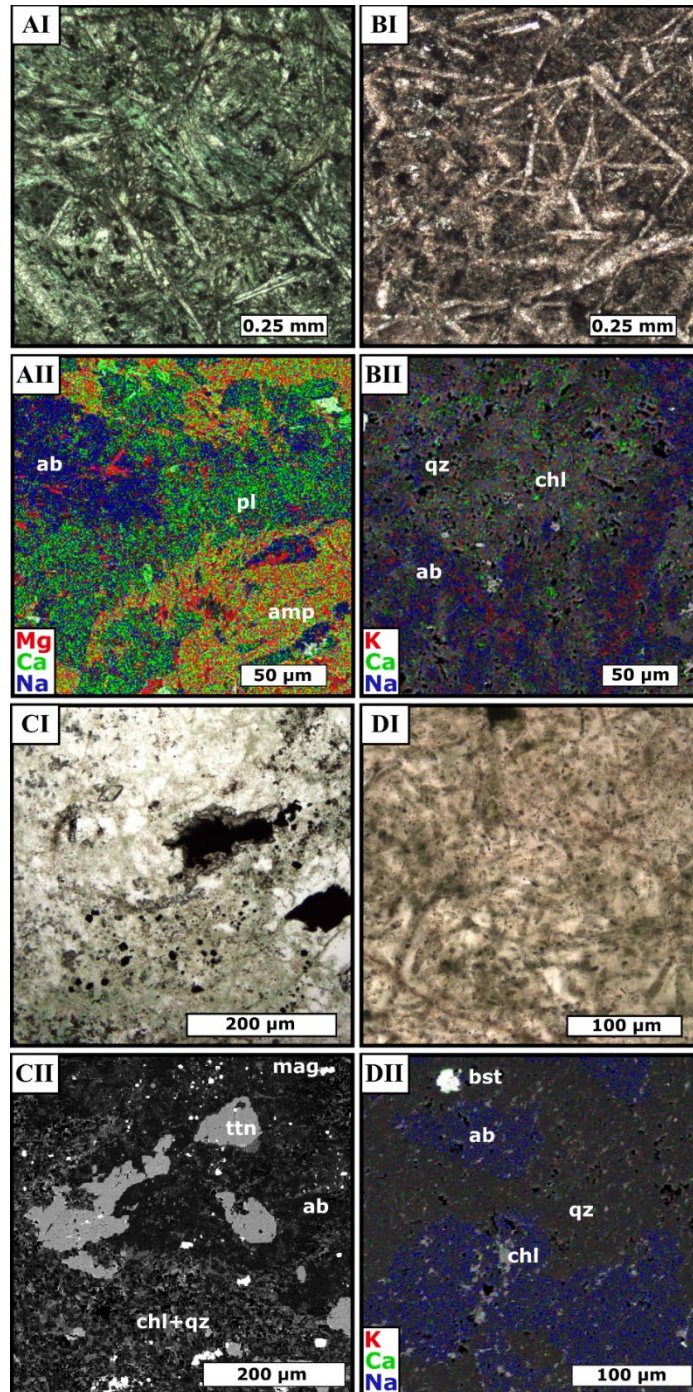


Figure 10: Examples of the chlorite-albite-quartz alteration from the different zones at Grey Fox, (except for A). Images are photomicrographs of thin sections in plane light (I) versus SEM X-Ray maps (II) of the same sample at higher magnification. Note the colour coding for X-ray images as indicated. **A.** Least altered sample of mafic metavolcanic rock from the Contact Zone. **B.** Mafic metavolcanic rock of the Contact Zone. **C** Intermediate metavolcanic rock of the 147 Zone. **D.** Felsic metavolcanic rock of the South Zone. Mineral abbreviations are given in Table 1.

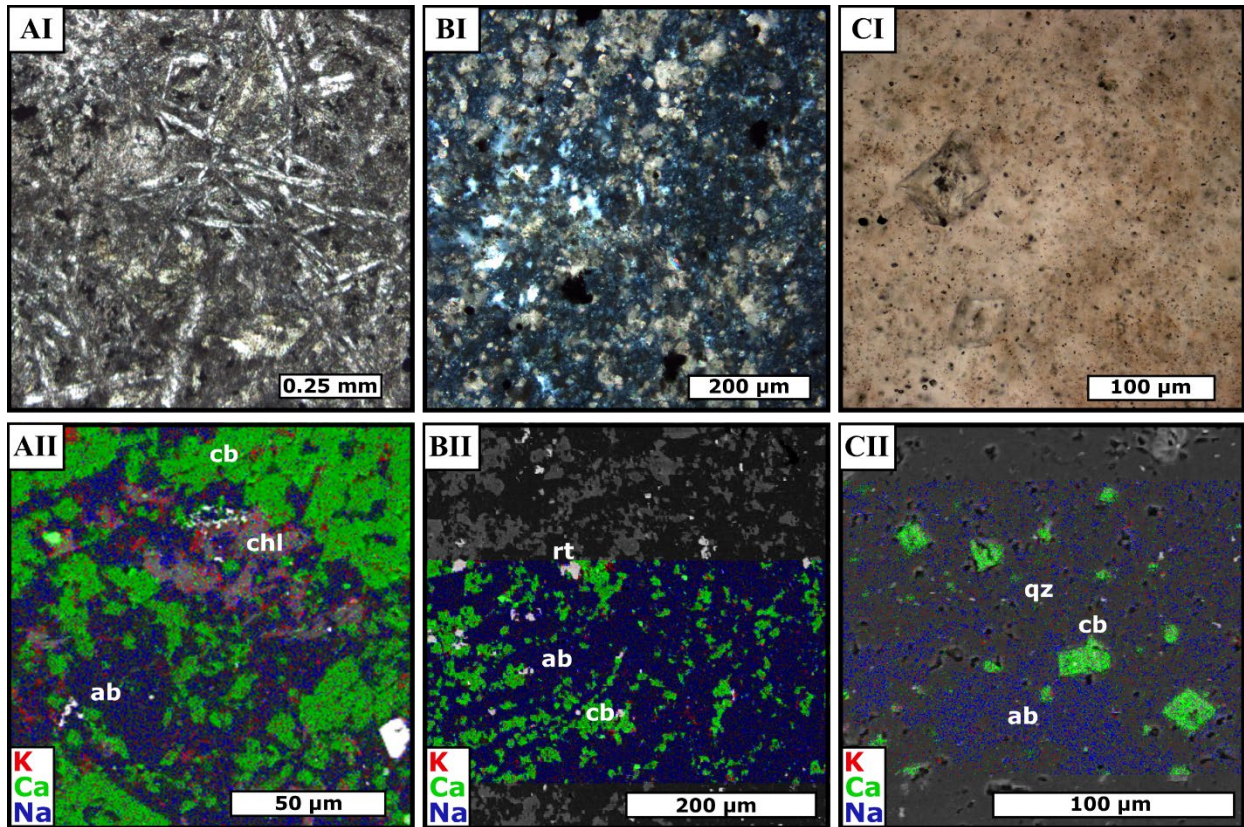


Figure 11: Examples of the sodic-carbonate alteration at Grey Fox in (I) photomicrographs of thin sections in plane light (A, C) and crossed nicols (B) and (II) SEM X-Ray maps of the same sample at higher magnification. Note the color coding for X-ray images as indicated. **A.** Mafic metavolcanic rock from the Contact Zone. **B.** Intermediate metavolcanic rock of the 147 Zone. **C.** Felsic metavolcanic rock of the South Zone. Mineral abbreviations are given in Table 1.

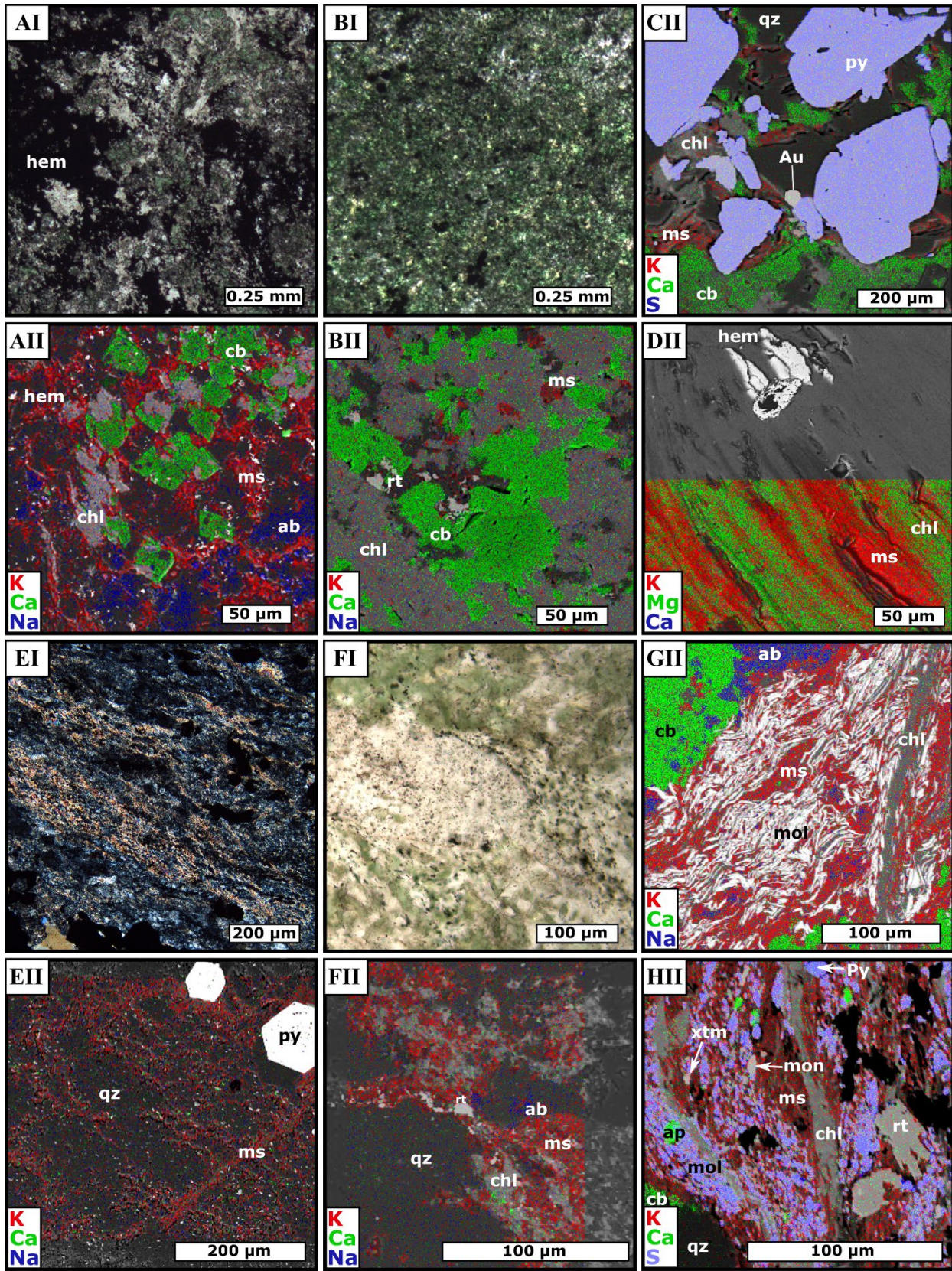


Figure 12: (Description on next page)

Figure 12: Examples of the muscovite-chlorite alteration at Grey Fox in (I) photomicrographs of thin sections in plane light (A, B, F) and crossed nicols (E) and (II) SEM X-Ray maps of the same sample at higher magnification. Note the color coding for X-ray images as indicated. **A-D.** Mafic metavolcanic rocks of the Contact Zone, note the replacement of carbonate by chlorite in A and the intergrown nature of muscovite, chlorite, and hematite association in D; **E** Intermediate metavolcanic rock of the 147 Zone. **F-H.** Felsic metavolcanic rocks of the South Zone. Mineral abbreviations are given in Table 1.

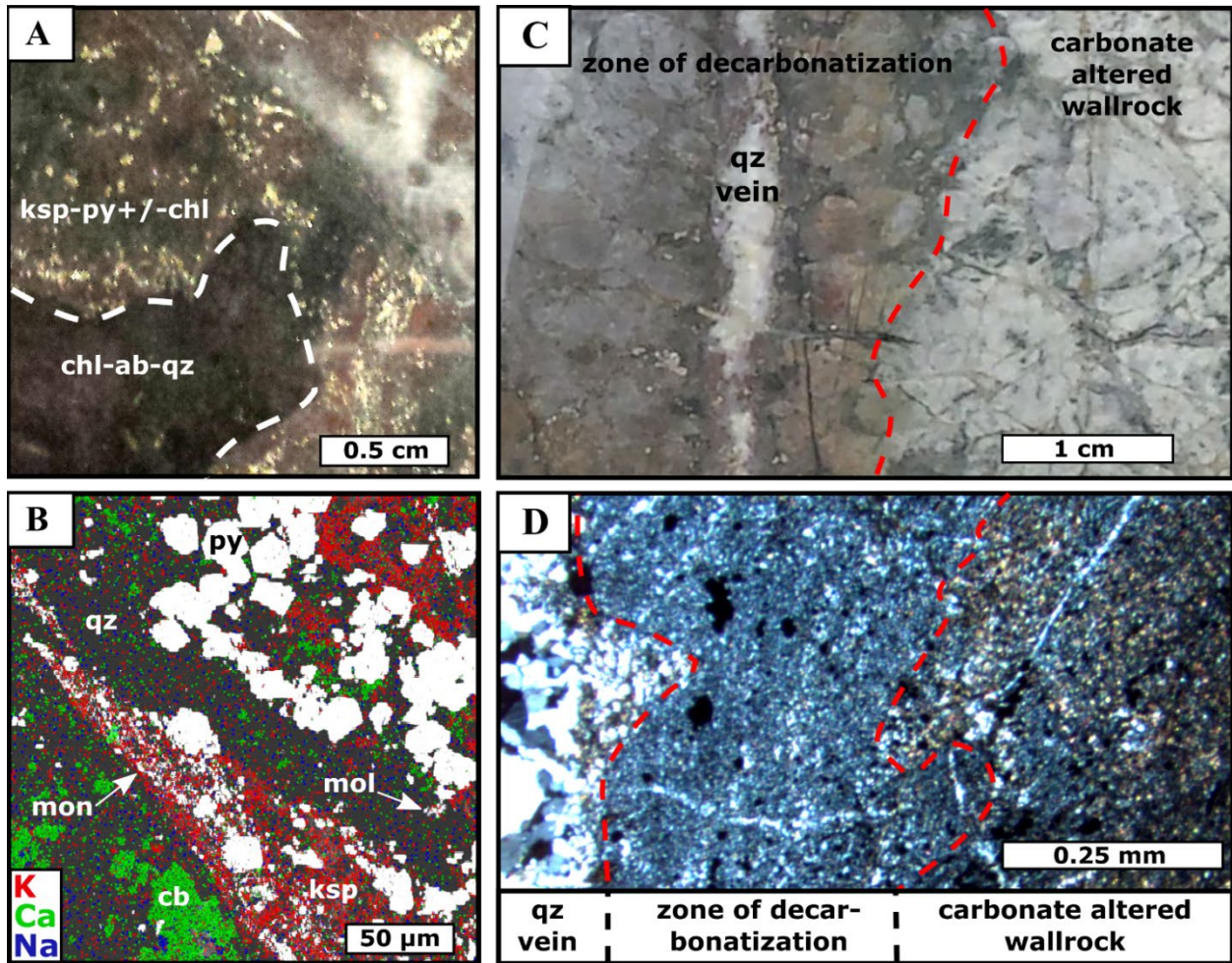


Figure 13: Vein-associated K-feldspar alteration (A, B) and decarbonatization (C, D) at Grey Fox. **A** Core showing sharp alteration contacts in the 147 Zone intermediate metavolcanics; note the red, K-feldspar and hematite altered clasts contained within the quartz vein. **B** SEM photomicrograph with false colors indicated of K-Feldspar alteration from the Contact Zone mafic metavolcanics with abundant pyrite (auriferous) and accessory phases such as molybdenite and monazite. **C** Core showing purple to red alteration halo around a quartz vein. **D** Photomicrograph in XPL showing the loss of carbonate in the alteration halo adjacent to a quartz vein (loss of high birefringence phase). Mineral abbreviations are given in Table 1.

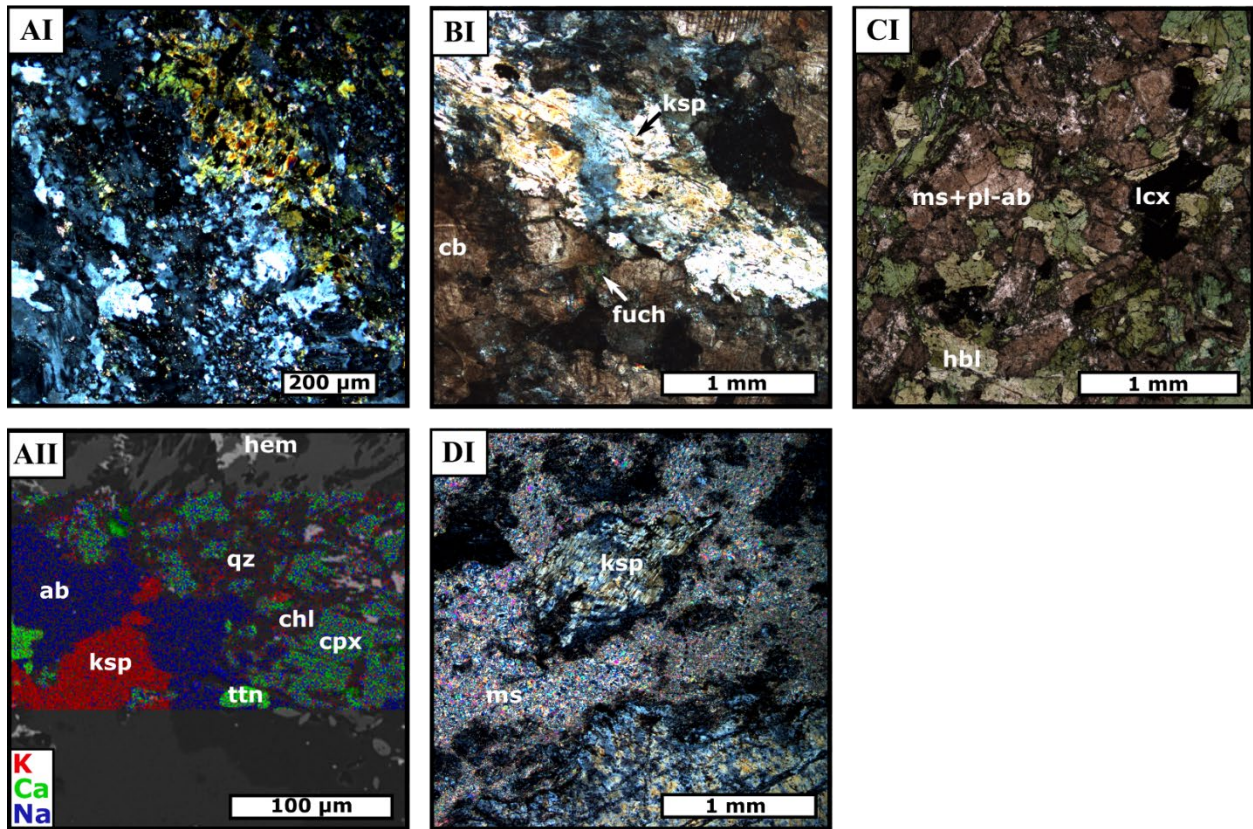


Figure 14: Examples of potassic alteration at Hislop in (I) photomicrographs in crossed nicols (A, C, D) and plane light (B) and (II) SEM X-ray map at higher magnification. Note the color coding for X-ray images as indicated. **A** Least altered felsic metavolcanic rock. Note the replacement of clinopyroxene by chlorite in AII. **B** Ultramafic metavolcanic rock adjacent to the central syenite. **C** Least altered mafic metavolcanic rock. **D** Least altered syenite (I), around which Au-mineralization is focused. Mineral abbreviations are given in Table 1.

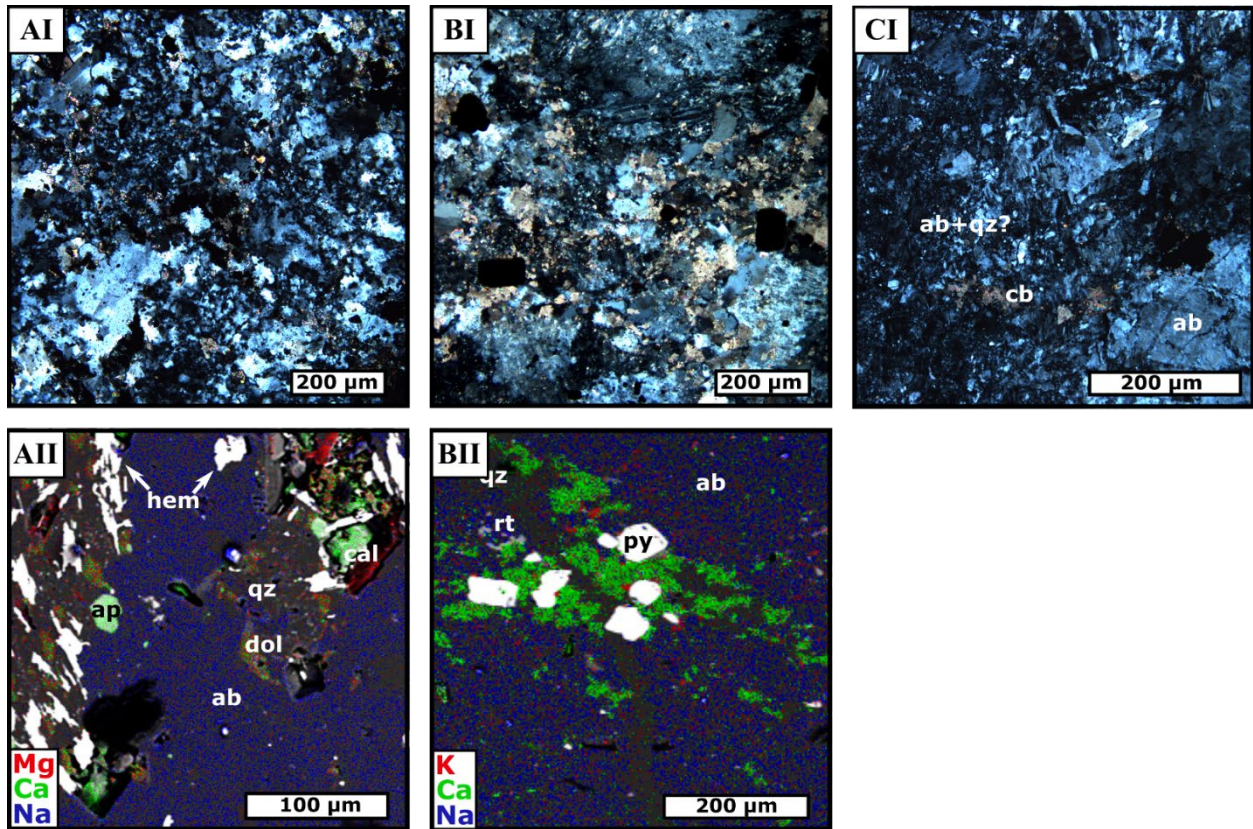


Figure 15: Examples of sodic-carbonate alteration at Hislop in (I) photomicrographs in crossed nicols and (II) SEM X-ray map at higher magnification. Note the color coding for X-ray images as indicated. **A** Distal alteration footprint in the felsic metavolcanics (~ 1 m away from the veins). **B** Proximal alteration in the felsic metavolcanics (<10 cm from vein); note the increased carbonate relative to the distal sample and the auriferous pyrite. **C** Syenite (I) from the centre of the pit. Mineral abbreviations are given in Table 1.

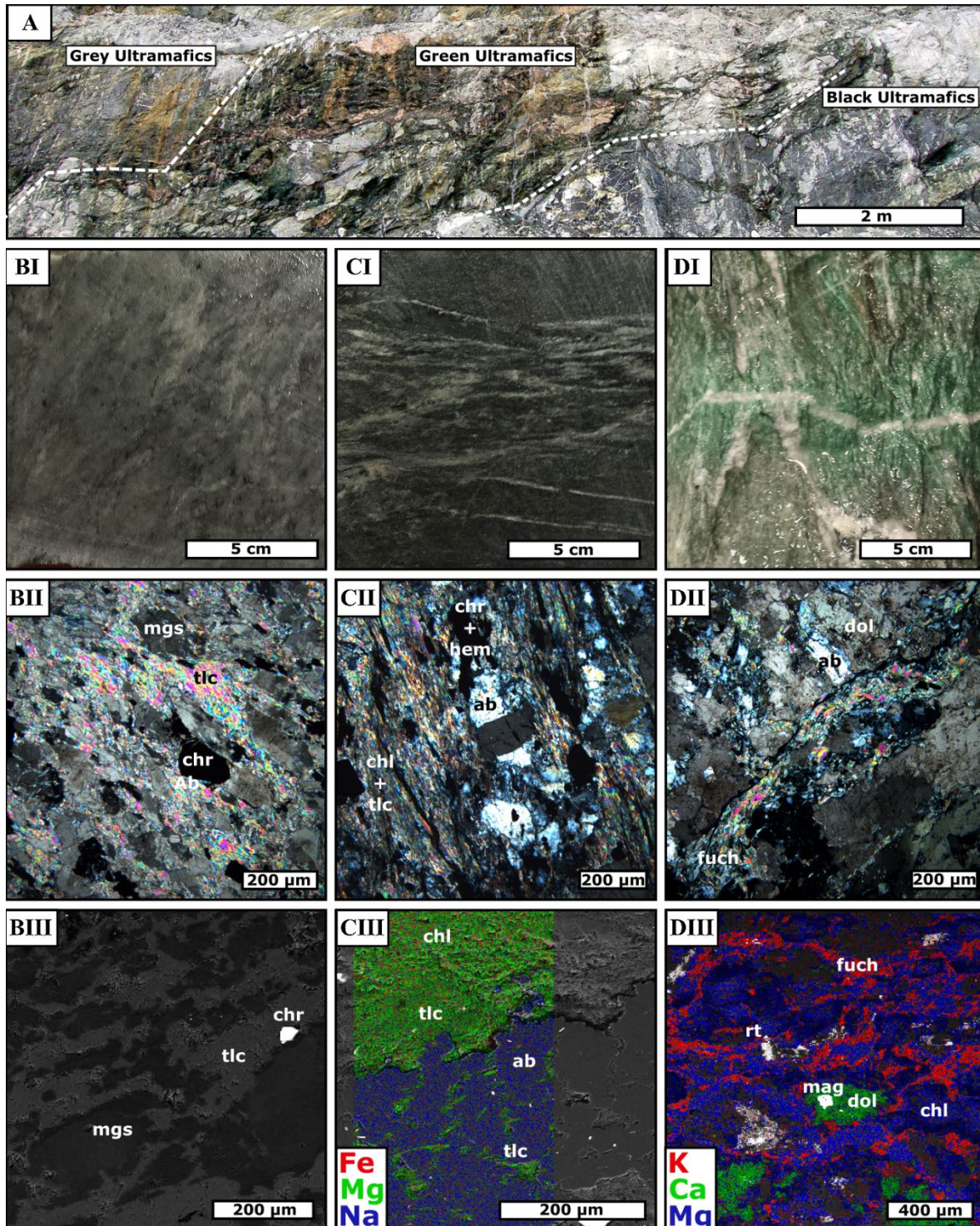


Figure 16: Alteration in the ultramafic metavolcanics at the Black Fox deposit. **A** is a photograph of the Black Fox open pit showing the relationship of the three ultramafic units as described in section 6.1. The **(B)** grey ultramafic metavolcanics, **(C)** black ultramafic metavolcanics, and **(D)** green ultramafic metavolcanic are shown in **(I)** hand sample, **(II)** photomicrographs in crossed nicols, and **(III)** SEM X-ray map at higher magnification. Note the color coding for X-ray images as indicated. Mineral abbreviations are given in Table 1.

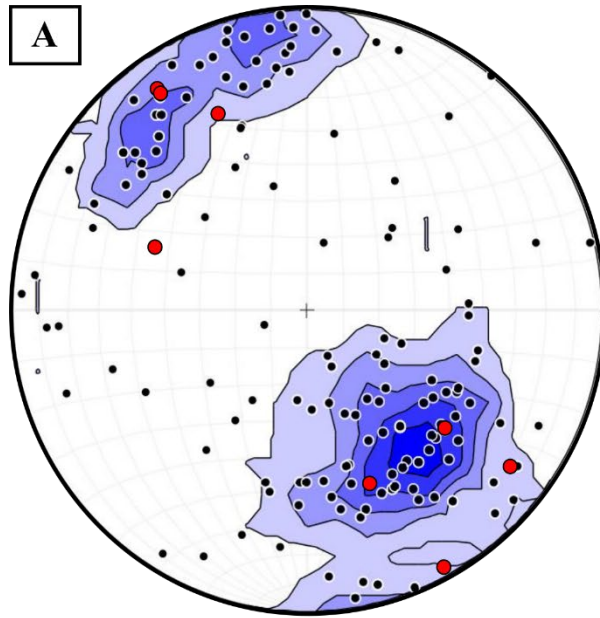


Figure 17: Orientations and conjugate features of vein sets. **A** Stereonet of vein orientations at Grey Fox (black circles, $n=155$, Kamb contouring in blue with intervals of 2 sigma, Chappell, pers. comm) and Hislop (red circles, $n=8$) with 2 distinct populations shared between the two deposits. **B** Mutually cross-cutting conjugate veins from the Hislop deposit.

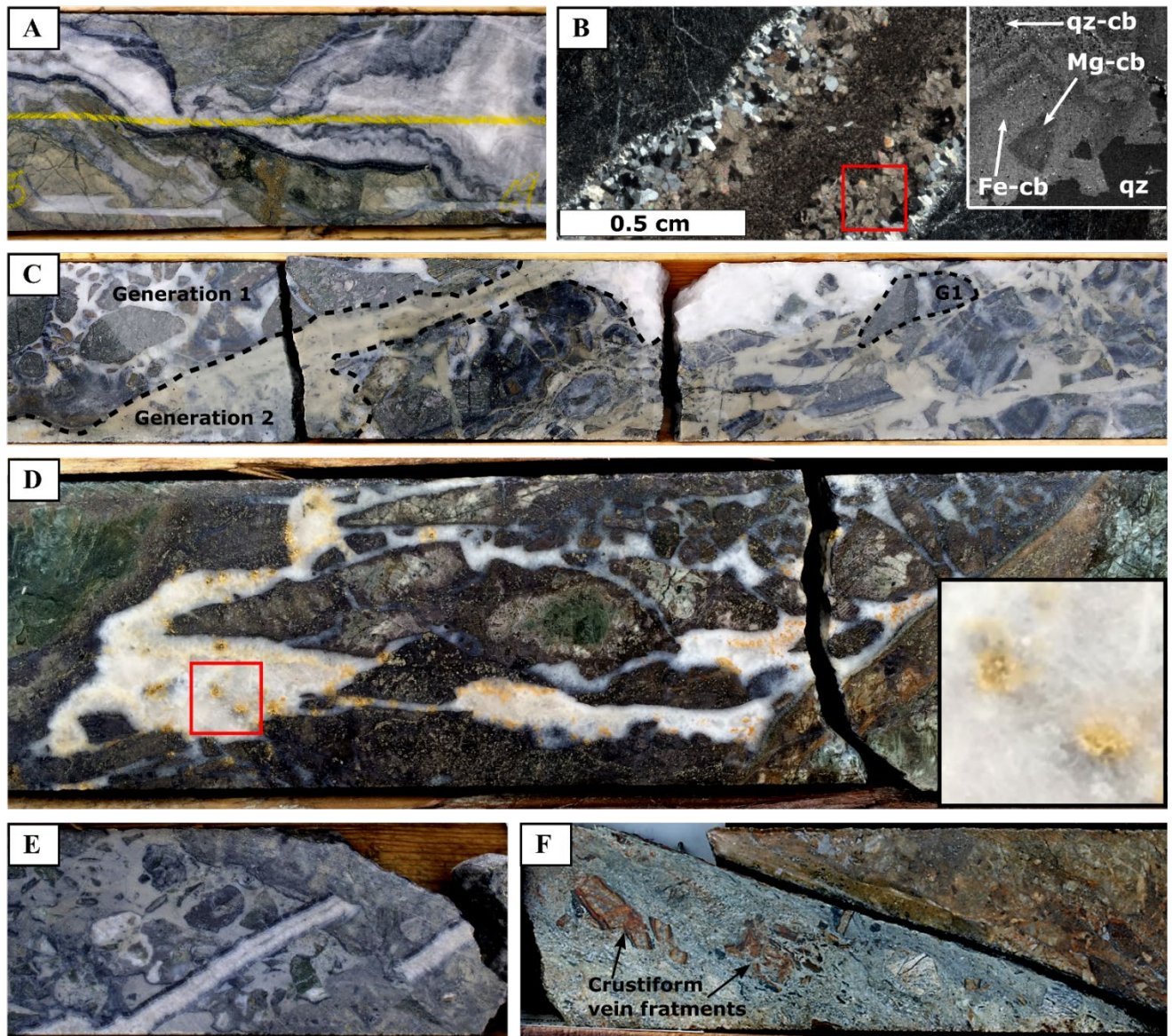


Figure 18: Vein samples from the Grey Fox deposit; note core ~4.7 cm wide. **A** Crustiform vein with dark grey margins due to molybdenite. **B.** XPL photomicrograph of crustiform vein exhibiting comb-texture quartz margins, overgrown by coarse carbonate crystals with a fine-grained carbonate-quartz interior; inset is a SEM backscattered electron image displaying chemical zonation in carbonate crystals. **C.** Breccia vein showing multiple stages of development with early dark grey to white quartz brecciating metavolcanic wall rock that is subsequently cross-cut and brecciated by a later carbonate-quartz vein. **D.** Breccia vein with abundant visible gold seen in the inset. Note the series of alteration zones in the clasts. **E.** A breccia-style carbonate-quartz vein cross-cut by a crustiform quartz vein with a dark grey rim and similar to earliest vein style observed in images C and D. **F.** Deformed crustiform veins that cut metavolcanic rocks seen in the deepest extent of the mineralization drilled at the deposit. Mineral abbreviations are given in Table 1.

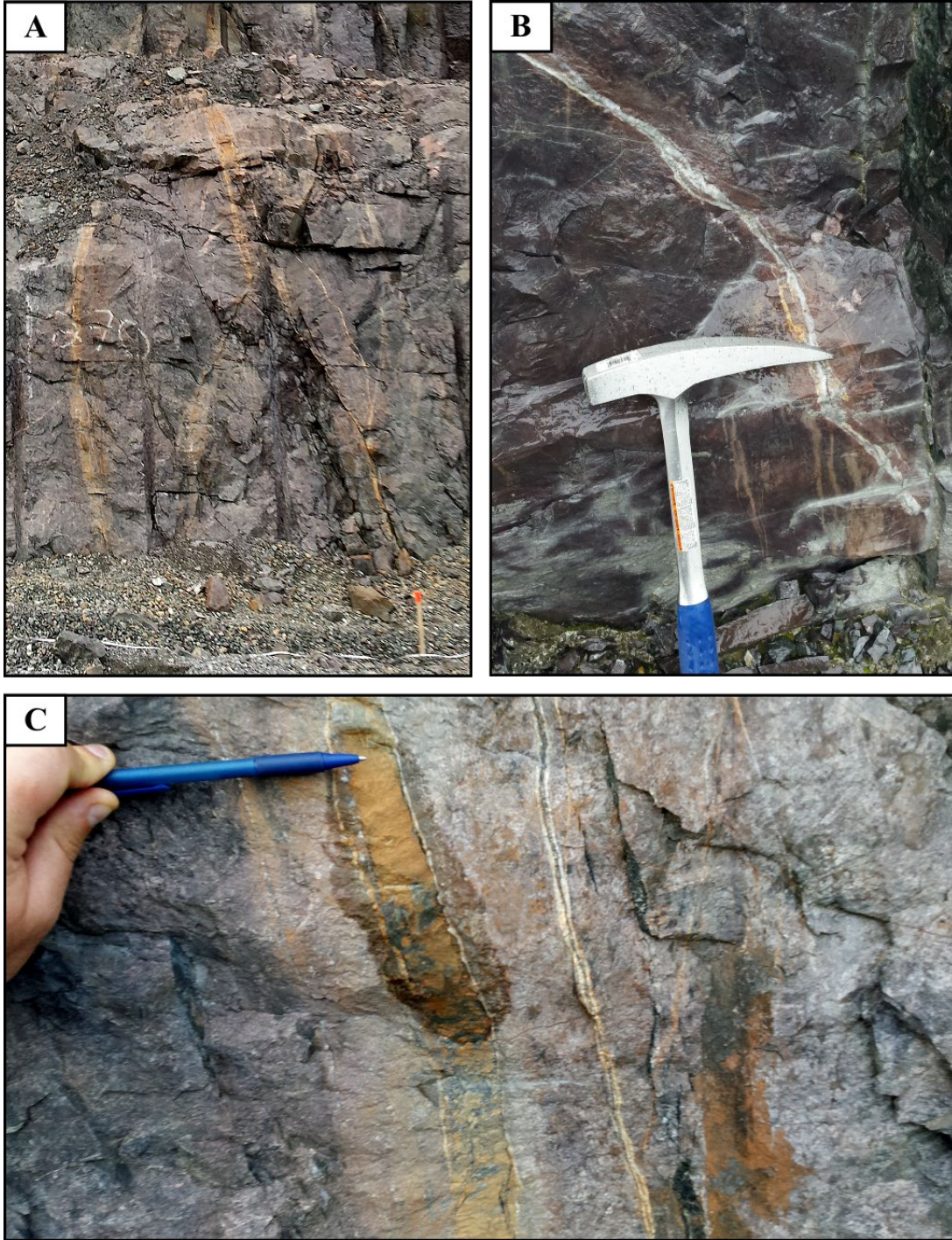


Figure 19: Au-associated veins present in the pit wall at Hislop. **A** Bleach and rusted halos surrounding vein sets in the felsic metavolcanics– bench height is approximately 8 feet. **B** Close up of auriferous veins. **C** Brecciated fragments of host felsic metavolcanics contained within a vein.

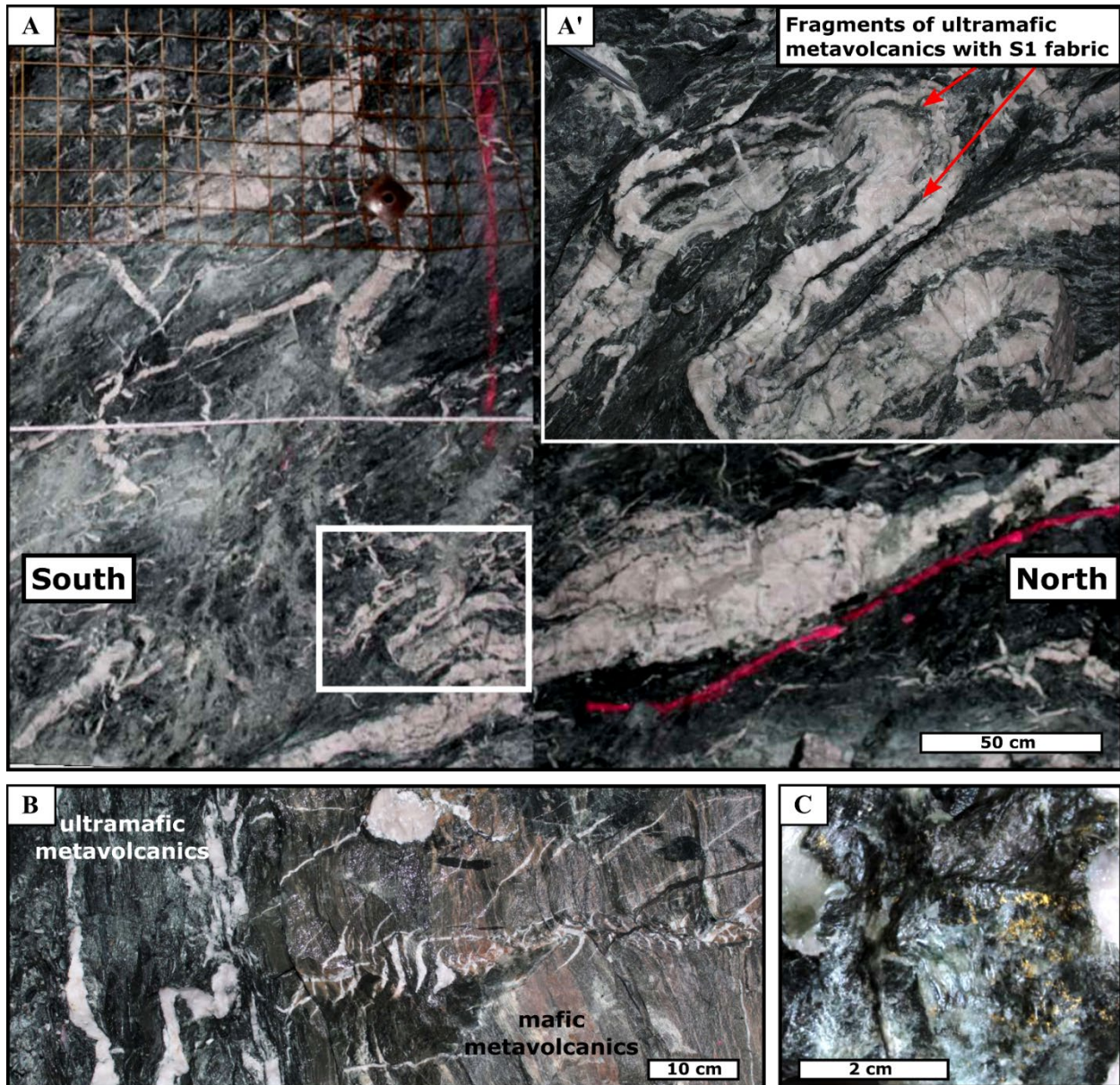
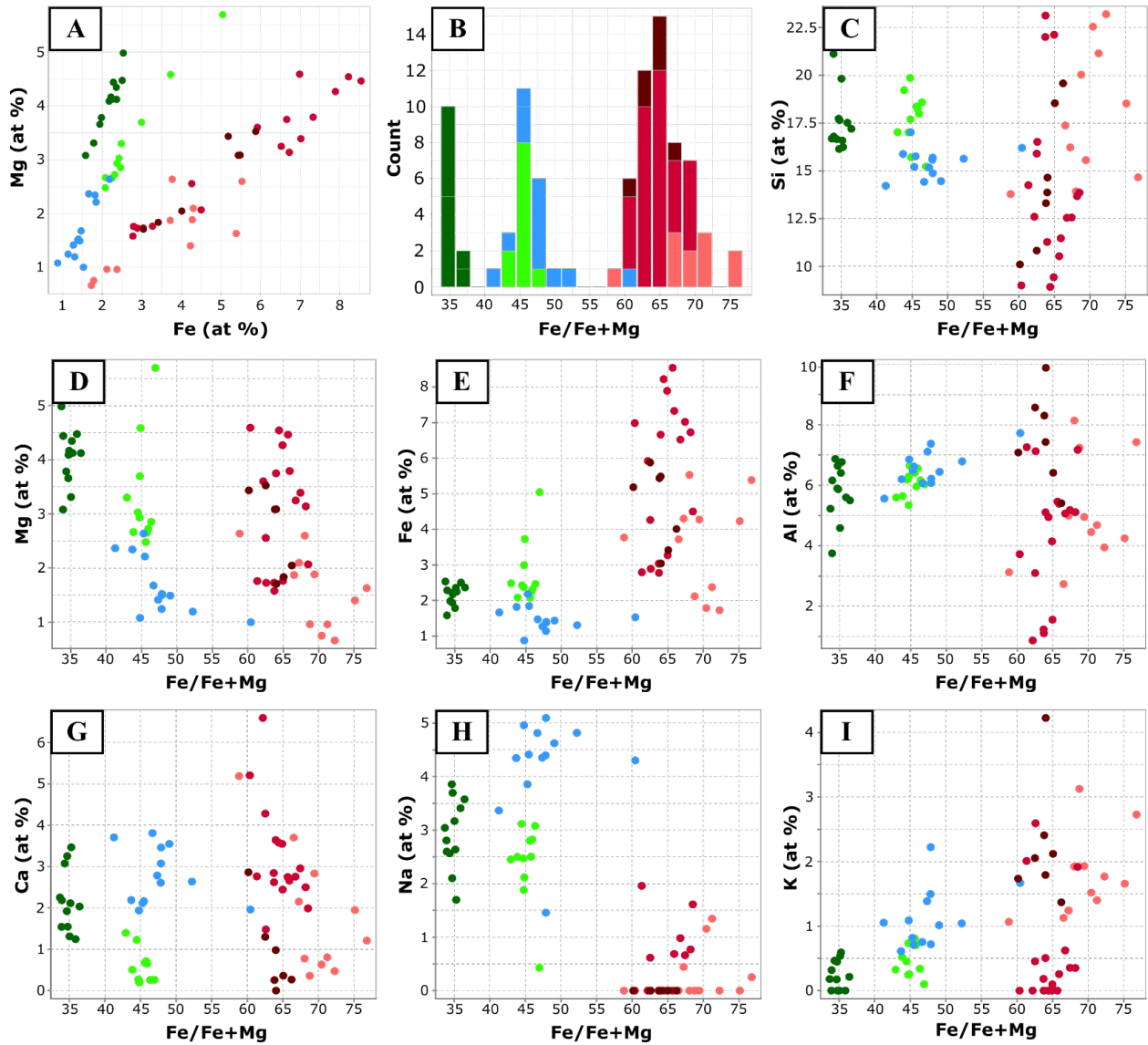


Figure 20: Veins at the Black Fox deposit. **A.** Shear veins within the ultramafic metabasaltic rocks. Inset image **A'** highlights the folded nature of the veins with the folding consistent with the D_3 deformation. These veins also contain fragments of the foliated ultramafic wall rock. **B.** An en echelon sigmoidal vein array within mafic metabasaltic rocks that overprint the earlier fabric. **C.** Gold mineralization along the contact between a fault-fill vein and altered ultramafic host rock.



Alteration Types

- Least Altered
- Type 1: chl-ab-qz
- Type 2: Sodic-carbonate
- Type 3: ms-dominant
- Type 3: chl-dominant
- Type 3: chl-ms with veining

Figure 21: Semi-quantitative SEM-EDS raster analysis of different alteration types, identified by color, from mafic metavolcanic rocks of the Grey Fox Contact Zone. Note that the Fe:Mg ratios (atomic) vary systematically with alteration (A, B) and is thus used to track alteration in the plots shown in C to F.

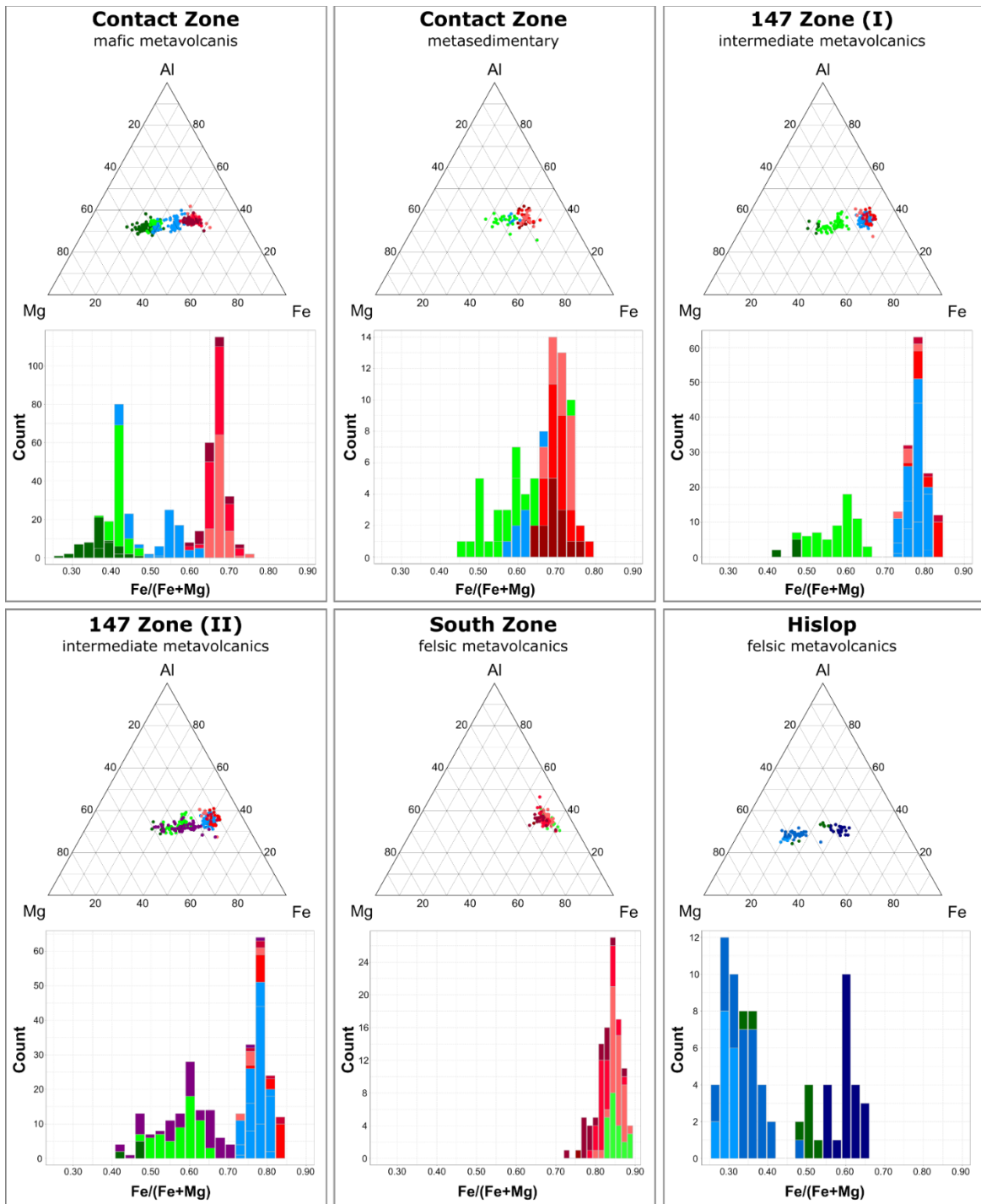


Figure 22: Chlorite chemistry (in atomic %), as determined from SEM-EDS analysis, for different alteration types and host rocks. Note that for the 147 Zone (II) there is the addition of a sample containing an auriferous vein with a K-feldspar halo (in purple) which is not present in 147 Zone (I). Colors match legend in Figure 21. Different shades of blue show the strength of sodic-carbonate alteration (light = weak, dark = strong). Each color represents one to two samples analyzed. At Grey Fox, gold mineralization is associated with red hued samples and at Hislop with blue.

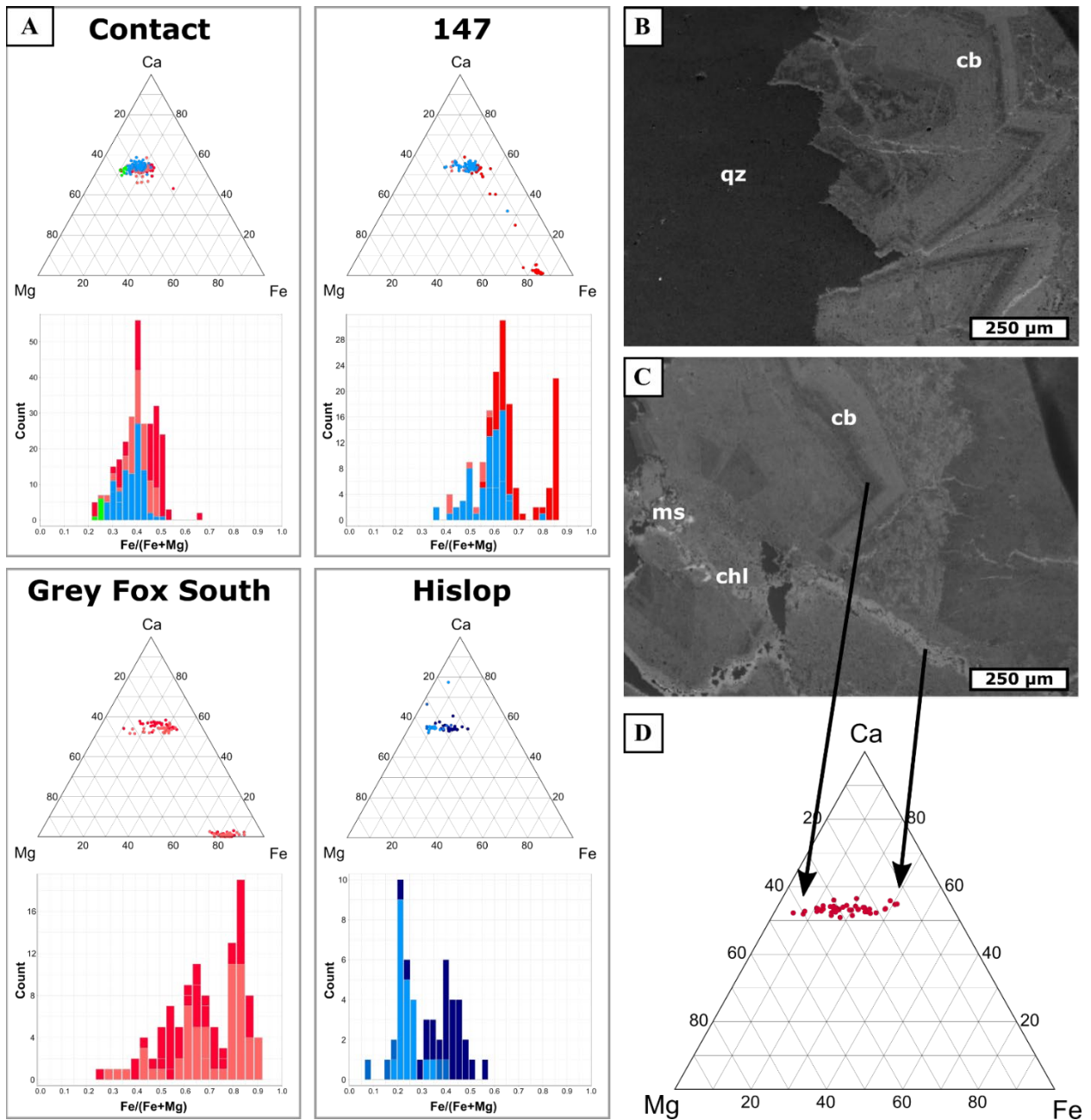


Figure 23: A. Dolomite chemistry (in at %), as determined from SEM-EDS analysis, for different alteration types; see Figure 20 for color legend. B. SEM backscattered electron image of Fe- and Mg- rich zonation in vein-carbonate. C. SEM backscattered electron image showing Fe-enrichment in vein-carbonate surrounding a fracture associated with muscovite alteration. D. Vein analysis graphed separately as the dolomite is commonly strongly zoned in these samples.

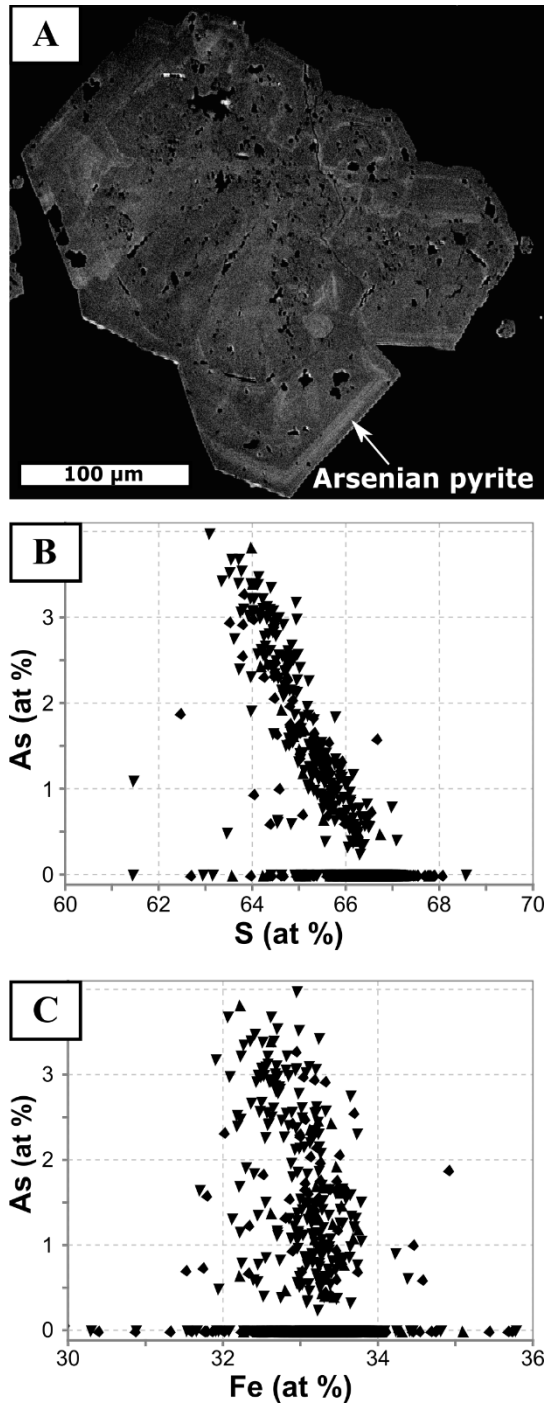


Figure 24: Diagrams showing the chemistry of pyrite from SEM-EDS analysis. **A.** SEM back scattered electron image, with brighter areas corresponding to higher abundances of As. Two stages of pyrite growth can be observed – an earlier stage that now has irregularly distributed As-rich areas, as well as pits, due to fluid reworking, which is overgrown by fresher pyrite that has oscillatory zoning best observed in the lower portion of the pyrite. **B.** Plot of S versus As contents. **C.** Plot of Fe versus As.

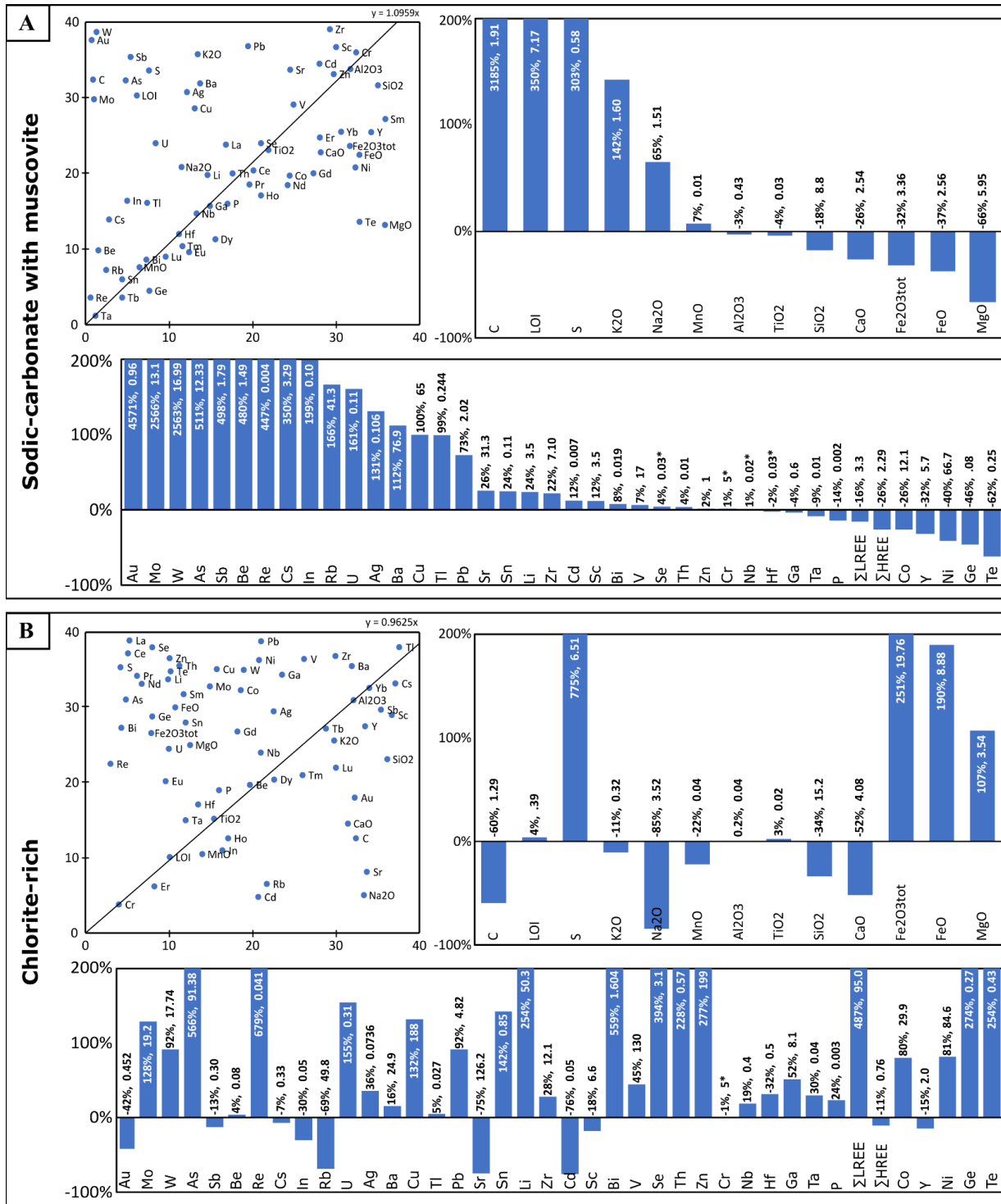


Figure 25: Isocon diagrams constructed after Grant (1986) for the sodic-carbonate alteration (with some muscovite contamination) in (A) and the chlorite-rich alteration in (B) at the Grey Fox deposit. The corresponding bar graphs are constructed for major elements (wt.%) and trace elements (ppm) with % change and absolute change given for each element. Elements near or below detection limits are denoted with asterisks.

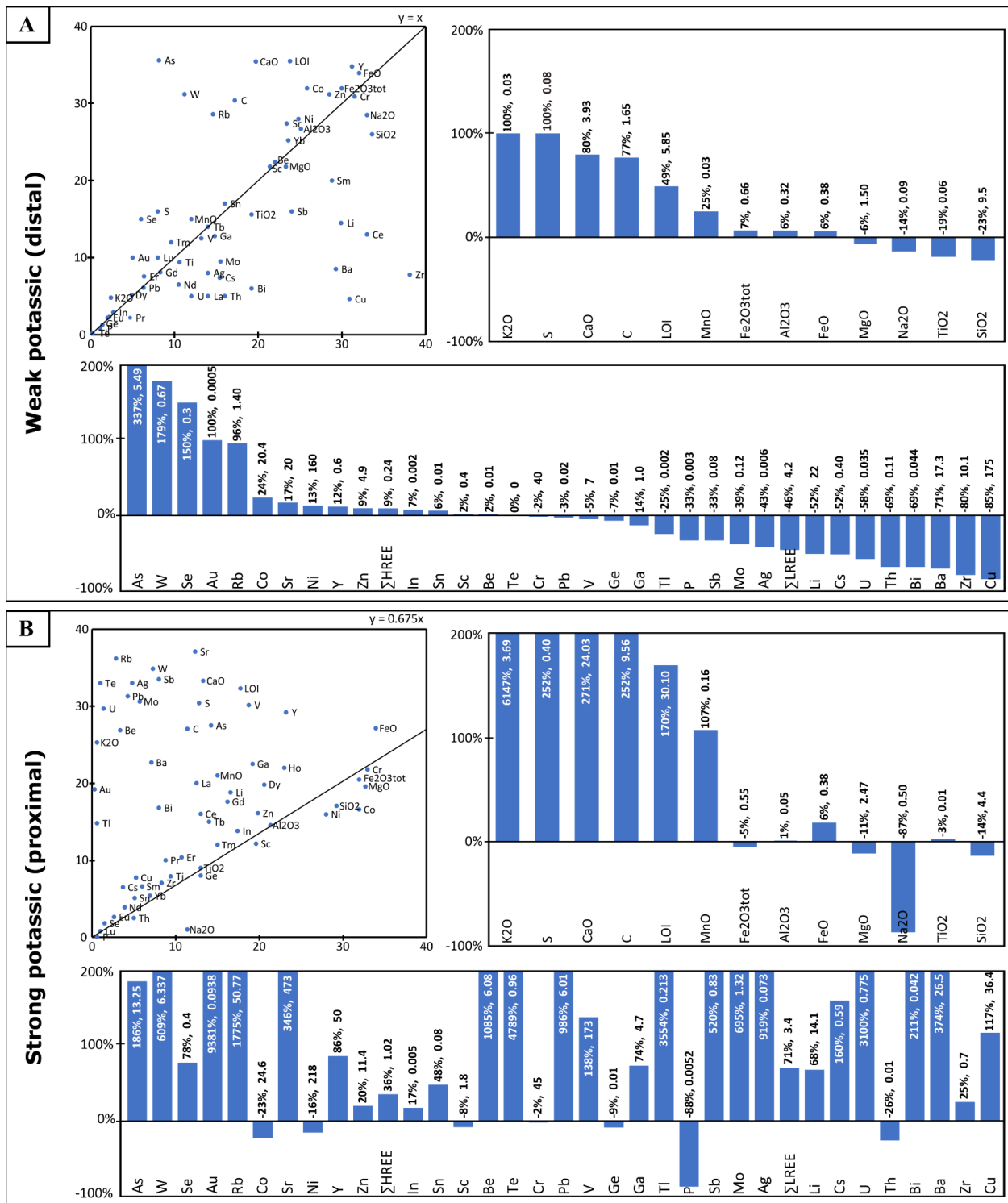


Figure 26: Isocon diagrams constructed after Grant (1986) for the K-feldspar-carbonate alteration at Hislop. Plot **A** is for the weaker distal alteration and plot **B** is of the gold-bearing alteration next to the syenite intrusion. Note that for **B**, the isocon shows significant dilution due to the intense carbonate breccia veining present in the sample that could not be removed. Set up is the same as Figure 25.

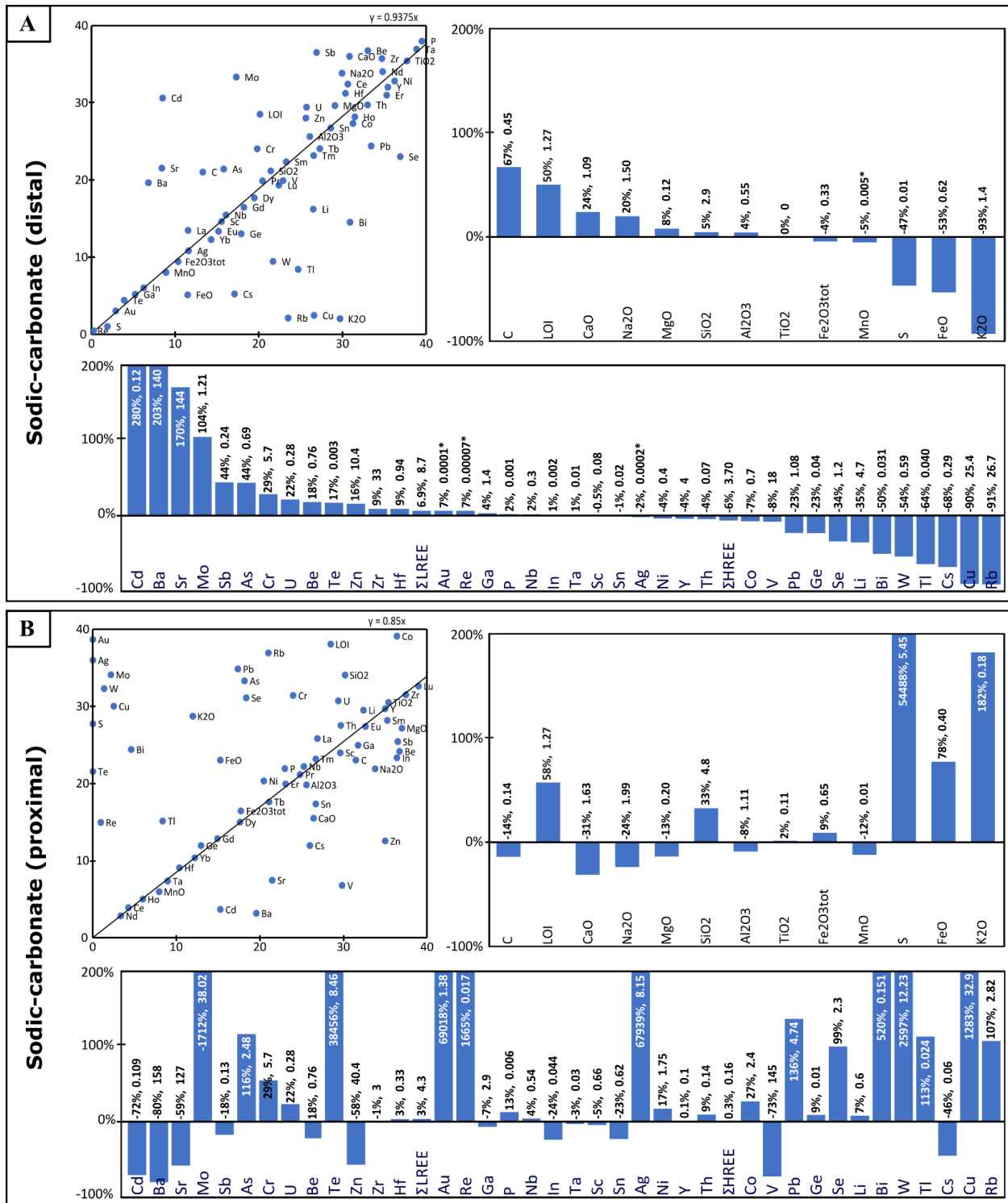


Figure 27: Isocon diagrams constructed after Grant (1986) for the sodic-carbonate alteration at Hislop. Plot **A** is of the weaker distal alteration with hematite still present and plot **B** is for the stronger, proximal alteration adjacent to quartz veins with pyrite present compared to the distal sodic-carbonate alteration. Set up is the same as Figure 25.

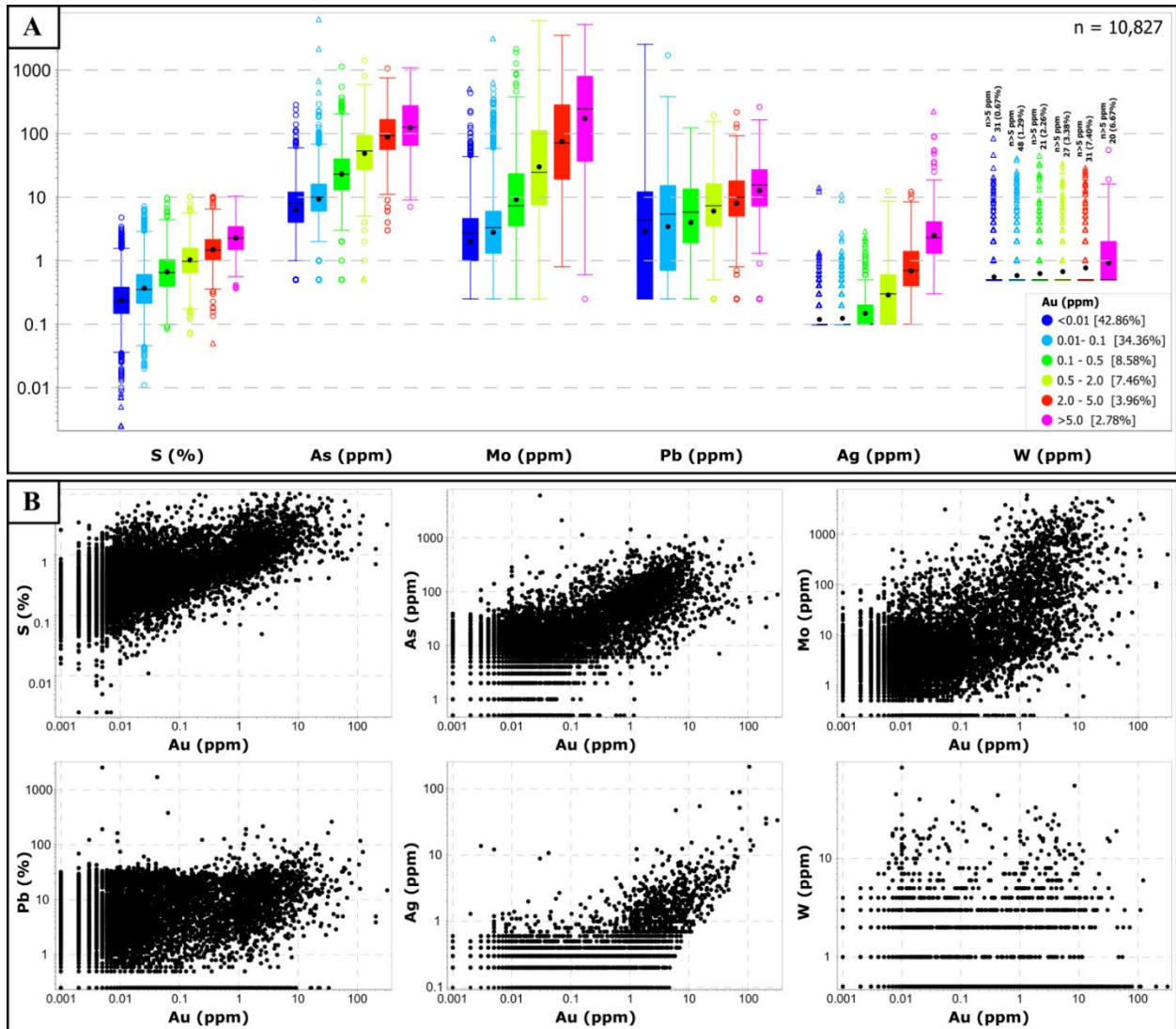


Figure 28: Plot of metal associations from whole-rock lithochemical data for variably altered and mineralized samples (n=10,827) from Grey Fox. **A.** Box and whisker plots with the data subcategorized by gold grade. **B.** Bivariate plots of the same elements versus Au. As the associations are similar for all rock types (mafic, intermediate, and felsic metavolcanic rocks) the results are all shown together.

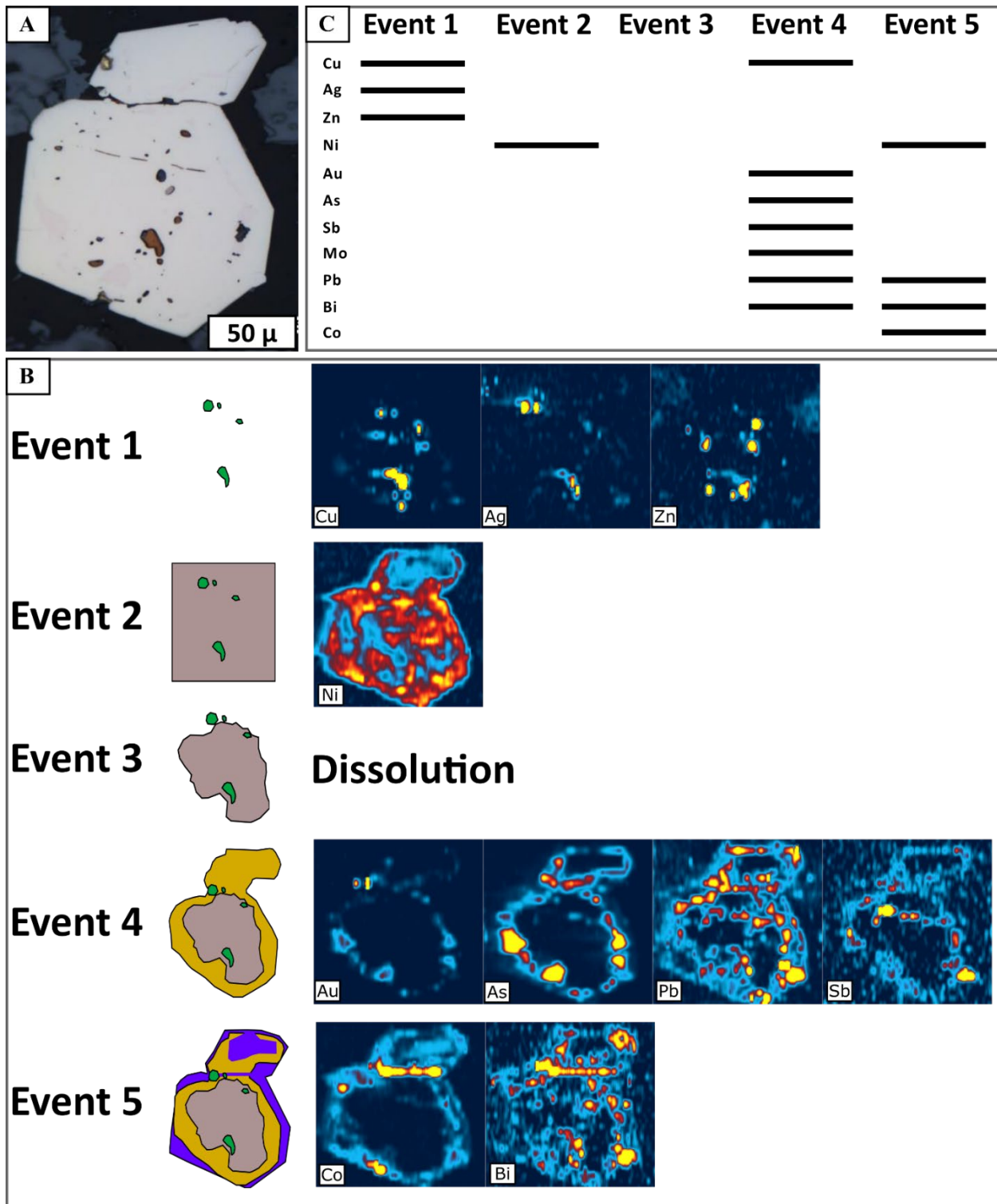


Figure 29: Auriferous pyrite from the mafic metavolcanics in the Grey Fox Contact Zone. **A.** Reflected light photomicrograph in plane polarized light. **B.** Select element maps from LA ICP-MS analysis of pyrite with results subdivided into different stages in the formation of the pyrite. **C.** An elemental paragenesis of the pyrite corresponding to the different stages interpreted in B.

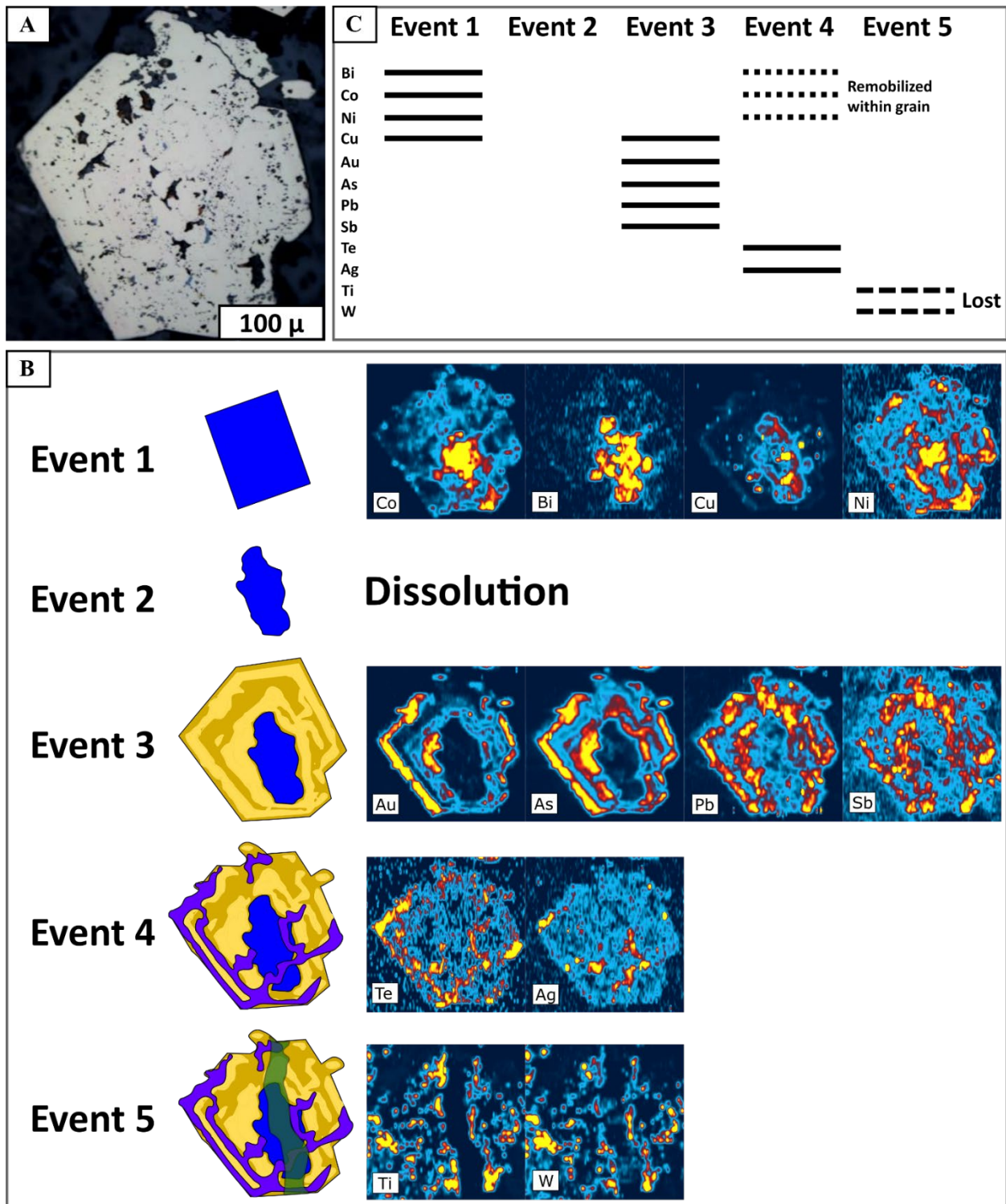


Figure 30: Auriferous pyrite from the intermediate metavolcanics in the Grey Fox 147 Zone. **A.** Reflected light photomicrograph in plane polarized light. **B.** Select element maps from LA ICP-MS analysis of pyrite with results subdivided into different stages in the formation of the pyrite. **C.** An elemental paragenesis of the pyrite corresponding to the different stages interpreted in B.

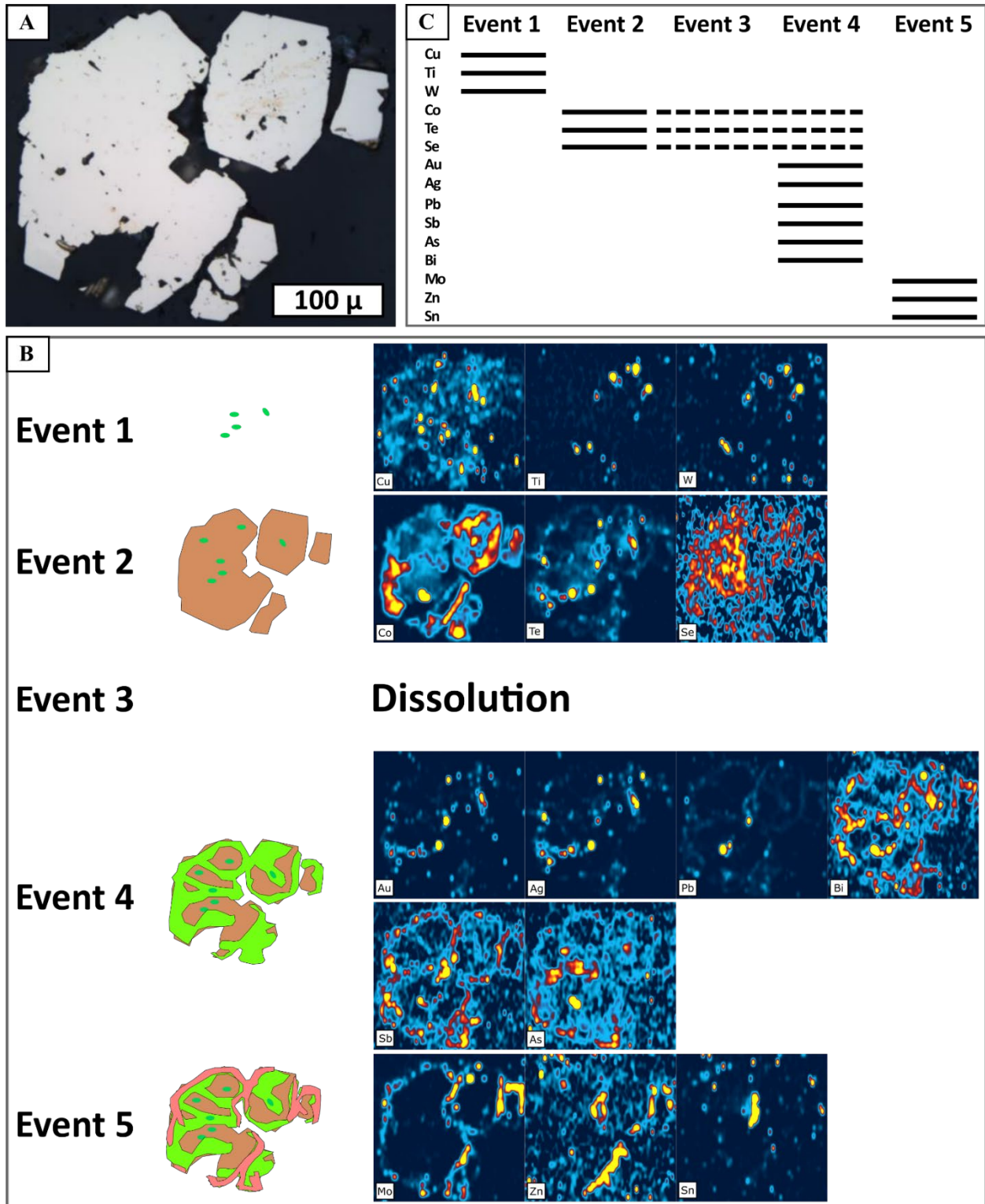


Figure 31: Auriferous pyrite from the felsic metavolcanics in the Hislop deposit. **A.** Reflected light photomicrograph in plane polarized light. **B.** Select element maps from LA ICP-MS analysis of pyrite with results subdivided into different stages in the formation of the pyrite. **C.** An elemental paragenesis of the pyrite corresponding to the different stages interpreted in B.

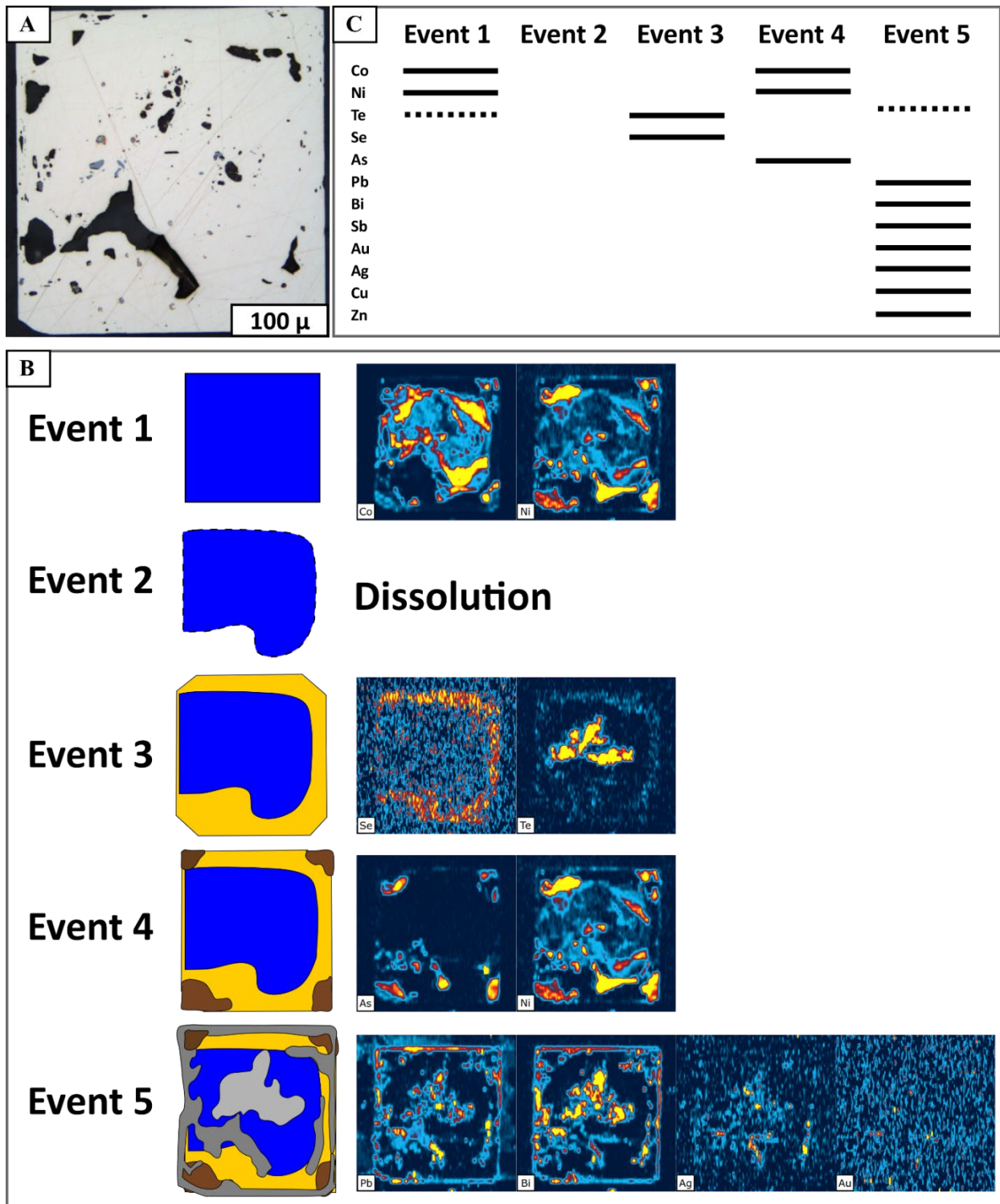


Figure 32: Cubic pyrite from the mineralized felsic intrusion from the Black Fox deposit. **A.** Reflected light photomicrograph in plane polarized light. **B.** Select element maps from LA ICP-MS analysis of pyrite with results subdivided into different stages in the formation of the pyrite. **C.** An elemental paragenesis of the pyrite corresponding to the different stages interpreted in B.

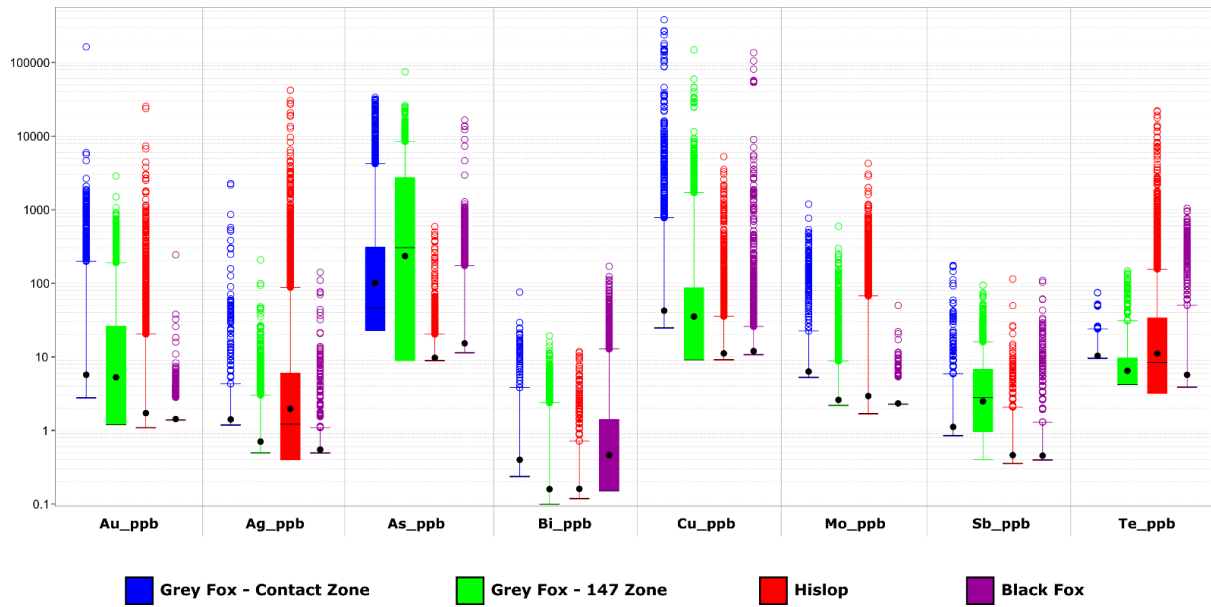


Figure 33: Box and whisker plots for metals in pyrite, as determined from LA ICP-MS analysis, from the Grey Fox (Contact and 147 Zones), Hislop, and Black Fox deposits.

	Metamorphic Assemblage	Retrograde Alteration	Sodic-Carbonate Alteration	Potassic Alteration	Muscovite-Chlorite Alteration
Plagioclase (res?)	—————			
Hornblende	—————			
Leucoxene (mag, ilm, ttn)	—————			
Albite I	—————			
Calcite		—————			
Chlorite (Mg>Fe)		—————		
Quartz		—————	—————	—————	—————
Rutile			—————	—————	—————
Albite II			—————	
Dolomite-Ankerite		Mg>Fe	—————		Fe~Mg
Hematite			-----	-----	
Siderite					-----
Muscovite					—————
Chlorite (Fe>Mg)				 —————
K-feldspar				—————	
Pyrite			—————	—————	—————
Gold				—————	—————
Veining				—————	

Figure 34: Paragenesis of alteration and mineralization for the three ore zones at the Grey Fox deposit. Solid lines denote dominant minerals for each alteration group, dotted lines denote minerals that visually appear to be remnant from previous mineral assemblages and are metastable or related to the onset of later alteration, and dashed lines denote minerals that were not present in all the zones, but which could still be constrained chronologically through textural relations and overprinting features.

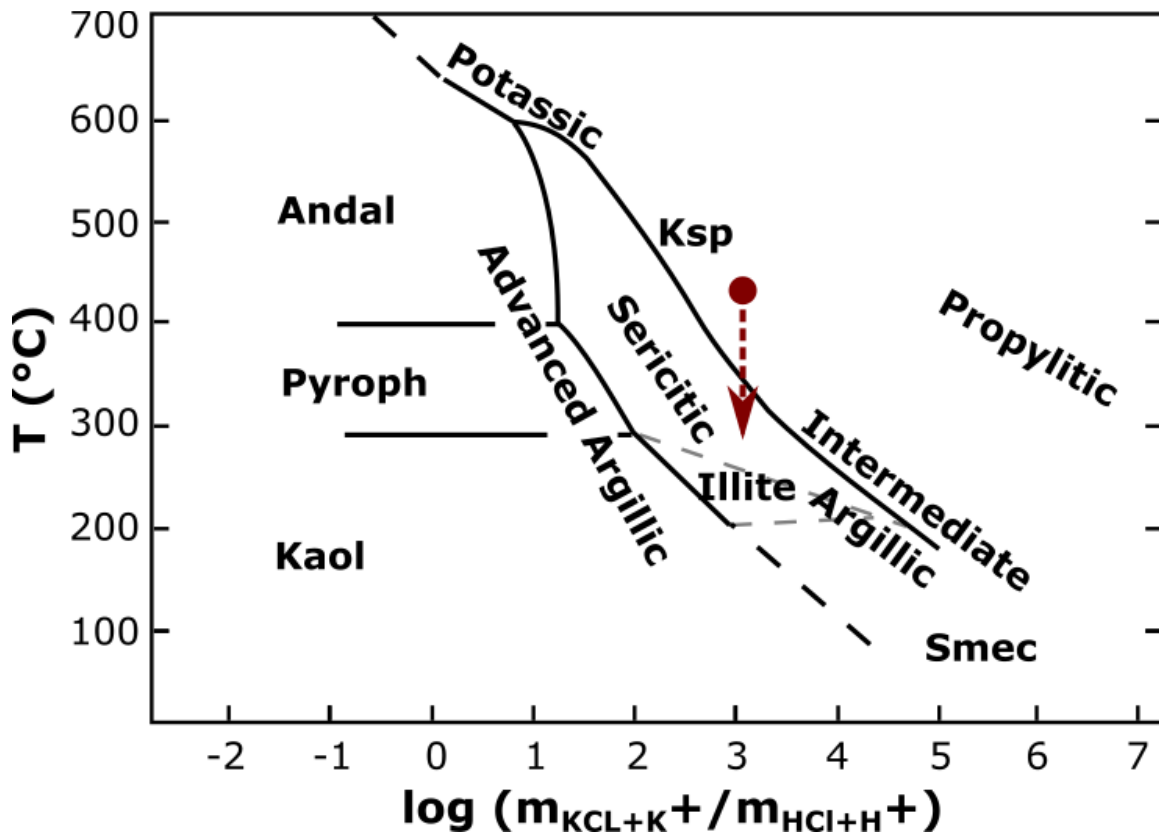


Figure 35: A plot of $\log(m_{KCL+K+} / m_{HCl+H+})$ versus temperature showing the stability fields for K-bearing alteration phases with the trace of a cooling fluid at a constant fluid chemistry shown in red (Seedorff et al., 2005). See text for discussion.

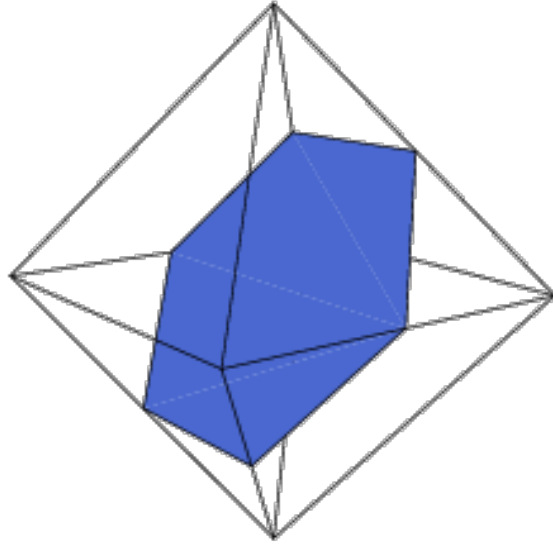


Figure 36: Octahedral pyrite with the cross-section displayed to produce a hexagonal shape (pers. comm. A. McDonald).

	Potassic-Phyllic Alteration	? Metamorphic assemblage	Sodic-Carbonate Alteration
K-feldspar	—————	
Muscovite	—————	
Hematite	—————	—————
Plagioclase/albite I		—————	
Hornblende		—————	
Leucoxene (mag, ilm, ttn)		—————	
Dolomite	—————		
Rutile			—————
Albite II			—————
Dolomite-Ankerite			Mg>Fe Fe~Mg
Chlorite			- - - - -
Pyrite			—————
Gold	—————		—————
Quartz veining			—————

Figure 37: Alteration paragenesis for the Hislop deposit. Solid lines denote dominant minerals for each alteration group, dotted lines denote uncertainty in timing of alteration/metamorphism, and dashed line for chlorite reflects the low abundance of chlorite in the early stages of the sodic-carbonate alteration.

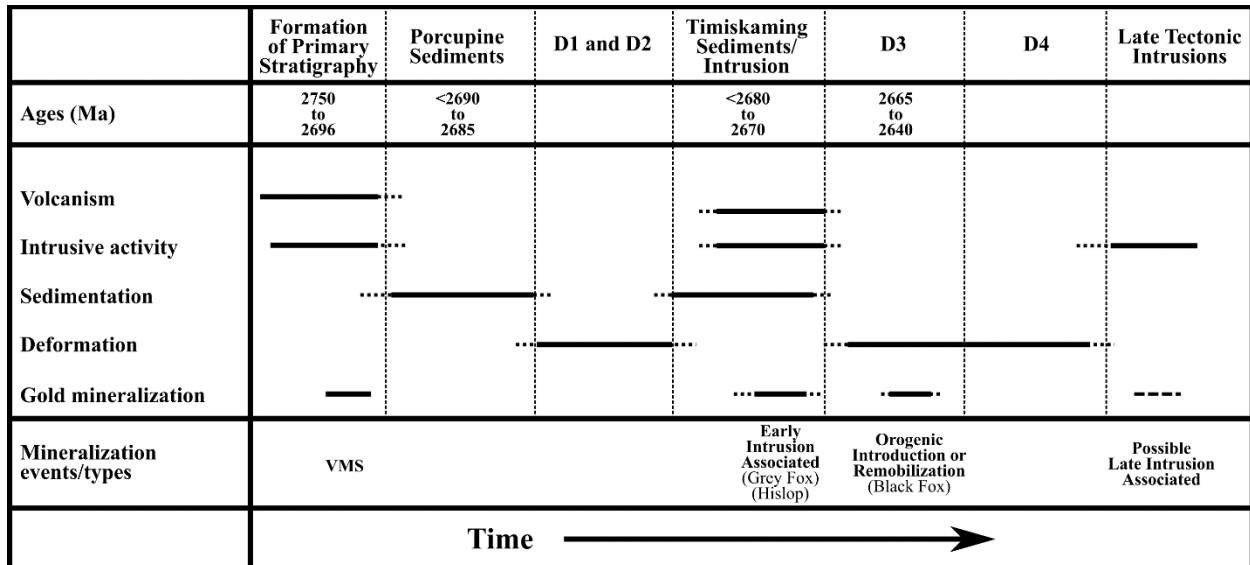


Figure 38: A simplified summary of the different geological events inferred to have constructed the AGB, with interpreted intervals of gold emplacement. Diagram is modified after Robert (2001) with dates from Ayer et al. (2005).

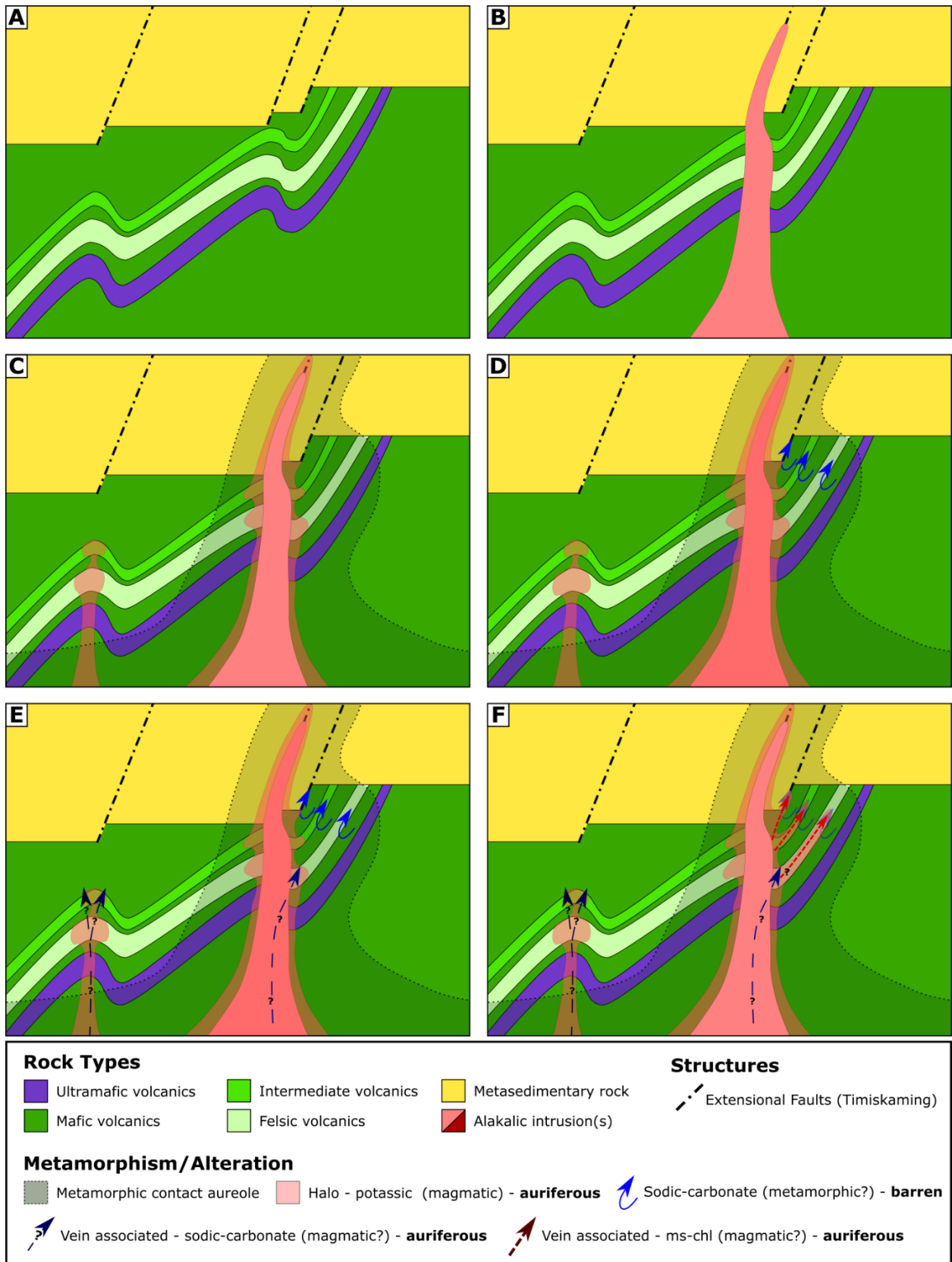


Figure 39: (continued on next page)

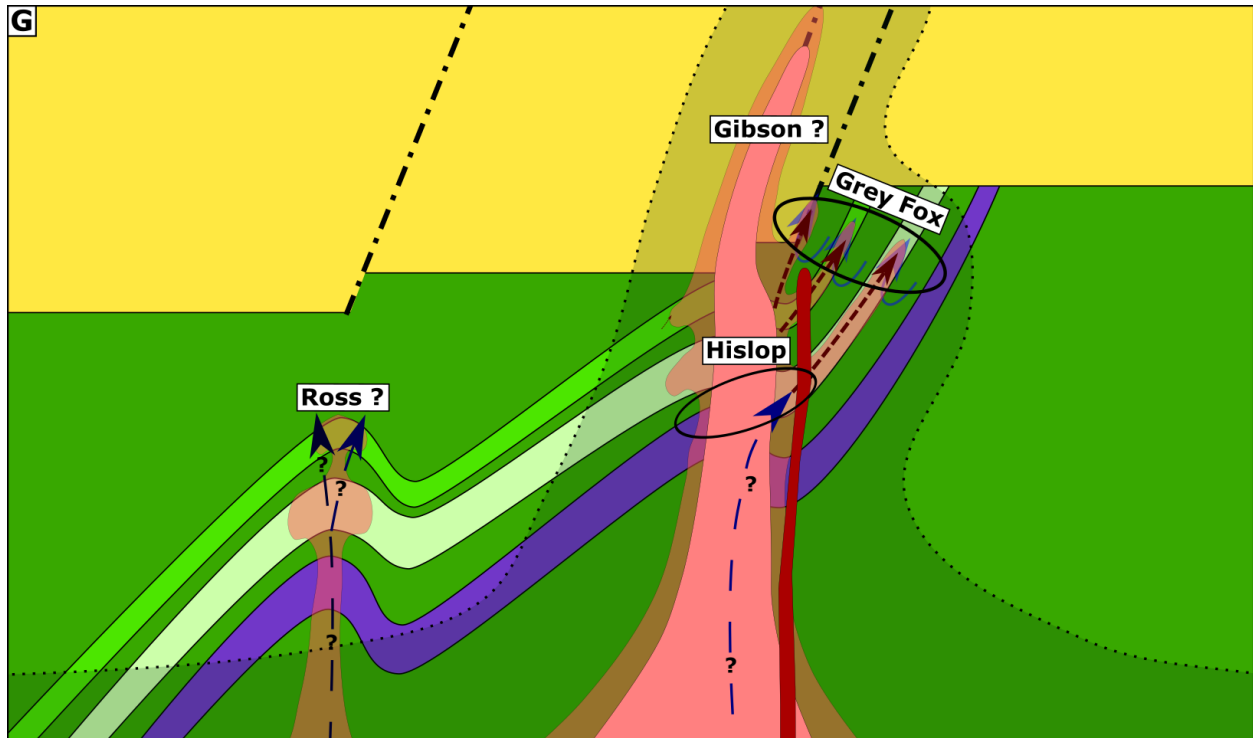


Figure 39: Schematic interpretation of the Hislop magmatic-hydrothermal system as sequential time slices from A-G. **A.** Geology pre-intrusive activity but after the onset of the Timiskaming basin formation; folding of the early volcanic units would be related to the D₁ and D₂ deformation events discussed in the texts. **B.** Initial alkalic intrusive activity. **C.** Initial introduction of gold associated with potassic alteration (K-feldspar + muscovite), which is observed at Hislop haloing the central syenite. Synchronous with or post-dating this event is the development of an inferred contact metamorphism related to intrusive activity. **D.** Initial formation of sodic-carbonate alteration, as seen at Grey Fox, which may relate to fluids generated via devolatilization of the wall rocks associated with intrusive activity. Note the preferential development of this alteration in the flow-tops of volcanic rocks and along rheologic contacts. **E.** Formation of later vein-associated mineralization with sodic-carbonate alteration, as observed at Hislop, which overprints the earlier potassic alteration. **F.** As the auriferous fluid in E interacts with previously potassic-altered rocks, it is buffered by the altered rocks, which advances the potassic alteration further into the more permeable units and forms the late-stage mineralization associated with potassic alteration at Grey Fox. **G.** Final time slice post-Timiskaming intrusive activity, but before the return to compressional tectonics, with the relative distribution of deposits in the Hislop township labelled (see text for discussion). Note that since the intrusive activity is broadly coeval with the mineralization, alkalic intrusions would form throughout the progressive events, including some that post-date the mineralizing events.

APPENDIX A: WHOLE-ROCK LITHOGEOCHEMISTRY RESULTS

Sample	Deposit	Rock	Comments	Certificate
BFP-002	Black Fox	Intrusive - Melanosyenite?		SD16070421
BFP-004	Black Fox	Intrusive - Albitized		SD16070421
BFP-006	Black Fox	Volcanic - Ultramafic	Green UM	SD16070421
BFP-007	Black Fox	Volcanic - Ultramafic	Grey UM	SD16070421
BFP-007DUP	Black Fox	Duplicate		SD16070421
BFP-008	Black Fox	Volcanic - Ultramafic	Black UM	SD16070421
BFP-009	Black Fox	Intrusive - Melanosyenite?		SD16070421
BFP-010D	Black Fox	Intrusive - Melanosyenite?		SD16070421
BFP-010L	Black Fox	Intrusive - Syenite?		SD16070421
BFP-013	Black Fox	Sediments		SD16070421
BFP-015	Black Fox	Intrusive - Felsic	QFP	SD16070421
BFP-016	Black Fox	Volcanic - Ultramafic	Grey	SD16070421
HP-006	Hislop	Volcanic - Felsic	Massive, ~1 m from vein, weakly altered	SD16070421
HP-007	Hislop	Volcanic - Felsic	Massive, close to vein, strongly altered	SD16070421
HP-010	Hislop	Volcanic - Mafic		SD16070421
HP-015	Hislop	Volcanic - Felsic	Flow-banded, weakly altered	SD16070421
HP-017	Hislop	Volcanic - Felsic	Massive, close to vein, strongly altered	SD16070421
HP-020	Hislop	Intrusive - Syenite II	Syenite II	SD16070421
HP-022a	Hislop	Volcanic - Felsic	Variolitic	SD16070421
MRG-1		Standard	Mount Royal Gabbro	SD16070421
SY-3		Standard	Syenite Rock	SD16070421
HPSW-002	Hislop	Volcanic - Mafic?		SD17268059
HPSW-007	Hislop	Intrusive - Syenite II		SD17268059
HPSW-011	Hislop	Intrusive - Syenite I		SD17268059
HPSW-011Dup	Hislop	Intrusive - Syenite I		SD17268059
HPSW-013	Hislop	Intrusive - Syenite I		SD17268059
HPSW-021	Hislop	Volcanic - Ultramafic	More sheared UM away from Syenite I	SD17268059
HPSW-024	Hislop	Volcanic - Ultramafic	Altered/competent UM, ~3 m from Syenite I	SD17268059
HPSW-027	Hislop	Volcanic - Ultramafic	Altered/competent; adjacent to Syenite I	SD17268059
HPR2-017	Hislop	Volcanic - Felsic		SD17268059
HPR2-076	Hislop	Intrusive - Mafic, LAM?		SD17268059
CK-102	Contact Zone	Volcanic - Mafic	Least altered	SD17268059
CK-107	Contact Zone	Volcanic - Mafic	Moderately altered sodic-carbonate	SD17268059
CK-113	Contact Zone	Volcanic - Mafic	Moderately altered chlorite-rich	SD17268059
LK-NIP-1		Standard		SD17268059

Package	ME-MS81								
Element	Ba	Ce	Cr	Cs	Dy	Er	Eu	Ga	Gd
Units	ppm								
BFP-002	214	89.6	610	6.75	3.64	1.61	2.21	13.6	6.32
BFP-004	92	40.7	120	0.05	1.48	0.57	0.92	6.2	2.45
BFP-006	161.5	2.2	1780	0.3	0.93	0.54	0.18	5.2	0.65
BFP-007	4.8	0.5	760	0.06	<0.05	<0.03	<0.03	0.6	0.06
BFP-007DUP	4.7	<0.5	750	0.03	<0.05	<0.03	<0.03	<0.1	<0.05
BFP-008	10.5	5.2	1950	0.35	1.48	0.94	0.33	8.3	1.43
BFP-009	116	55.9	640	1.01	3.45	1.69	1.61	13.4	5.02
BFP-010D	39.2	108.5	740	0.27	4.45	2.06	2.82	15.2	7.02
BFP-010L	863	45.6	70	0.04	1.92	0.96	1.14	17.4	2.73
BFP-013	418	58.3	170	0.65	2.3	1.23	1.15	17.7	3.03
BFP-015	552	26.4	20	0.25	1.18	0.7	0.55	17.8	1.44
BFP-016	2.9	<0.5	850	0.04	<0.05	<0.03	<0.03	0.7	<0.05
HP-006	154	41.4	30	0.13	17.65	11.55	2.72	34.8	14.95
HP-007	22.4	35.8	30	0.06	15.05	10	2.29	27.5	12.9
HP-010	125.5	8.7	80	1	3.49	2.35	0.7	14.5	3.07
HP-015	49.4	40.2	20	0.43	19.55	13.2	3.12	38.1	16.65
HP-017	56.1	46.3	30	0.09	18.35	11.75	2.71	19.4	15.4
HP-020	399	124	20	0.41	1.69	1.09	0.83	24.9	2.31
HP-022a	56.8	35.6	40	1.55	15.9	10.75	2.61	32.9	13.45
MRG-1	46.8	24.7	490	0.59	3.07	1.26	1.45	17.5	4.15
SY-3	427	2280	10	2.53	128	80.8	17.55	36.4	116.5
HPSW-002	75.6	14.5	20	0.24	5.68	3.72	1.28	18.6	4.89
HPSW-007	529	80.1	10	0.52	1.67	1.29	0.84	27.6	2.03
HPSW-011	701	62.4	20	0.18	1.19	0.73	0.66	21	1.65
HPSW-011Dup	764	66.2	20	0.22	1.12	0.66	0.71	21	1.83
HPSW-013	1220	54.3	10	0.71	1.4	0.94	0.58	29.7	1.74
HPSW-021	24.4	3.3	2100	0.77	0.98	0.53	0.2	7.4	0.83
HPSW-024	7.1	1.3	2060	0.37	1.03	0.63	0.22	6.4	0.81
HPSW-027	22.7	1.6	1360	0.65	0.99	0.61	0.22	7.5	0.88
HPR2-017	7	49.8	30	0.33	18.9	12.35	2.68	37.5	15.35
HPR2-076	44.5	8.9	80	2.43	3.17	2.03	0.79	13.1	2.78
CK-102	68.6	6.7	360	0.94	3.11	1.87	0.62	14.9	2.48
CK-107	159.5	6.8	400	4.64	2.26	1.65	0.48	15.7	1.82
CK-113	177.5	49.6	380	4.15	2.04	1.24	1.01	22.9	2.68
LK-NIP-1	143	19.3	160	0.57	3.84	2.32	1	20	3.61

Package	ME-MS81								
Element	Hf	Ho	La	Lu	Nb	Nd	Pr	Rb	Sm
Units	ppm								
BFP-002	2.6	0.69	41.3	0.22	3.4	43.8	10.85	118.5	8.36
BFP-004	1.4	0.25	18.3	0.09	3.1	21.8	5.3	3	3.98
BFP-006	0.5	0.22	0.9	0.1	0.4	1.6	0.34	21.7	0.57
BFP-007	<0.2	0.01	<0.5	<0.01	<0.2	0.3	0.06	<0.2	0.05
BFP-007DUP	<0.2	<0.01	<0.5	0.01	<0.2	0.1	<0.03	<0.2	<0.03
BFP-008	0.7	0.31	2.1	0.13	0.9	3.5	0.74	1.6	0.97
BFP-009	2.4	0.69	25.7	0.23	3.8	30	7.15	21.1	6.22
BFP-010D	2.7	0.88	55.3	0.25	6	48.8	12.7	3.8	9.06
BFP-010L	2.1	0.38	22.5	0.12	5.5	20.7	5.43	1.3	3.81
BFP-013	4.2	0.46	29.3	0.17	5.2	24.3	6.59	73.3	4.12
BFP-015	3.4	0.24	13.3	0.13	7.9	10.4	2.95	26.1	2.04
BFP-016	<0.2	<0.01	<0.5	<0.01	<0.2	0.1	<0.03	0.2	0.03
HP-006	9.8	4.02	13.2	1.93	13.9	34	6.62	2.6	11.75
HP-007	8	3.35	12.2	1.62	11.7	28.8	5.66	4.1	9.42
HP-010	1.5	0.75	3.2	0.36	2.2	6.7	1.34	75.4	2.3
HP-015	10.8	4.51	11.8	2.25	14.7	34.9	6.85	28	12.3
HP-017	9.8	4.2	17.5	1.92	13.1	34.4	6.97	13.8	11.25
HP-020	6.3	0.35	90	0.21	11.9	25.2	9.45	134	3.52
HP-022a	8.5	3.64	11.9	1.75	12.1	29.2	5.71	42.6	9.83
MRG-1	3.6	0.54	8.7	0.12	18.7	17.6	3.58	6.7	4.55
SY-3	9.2	28.8	1320	8.25	189	693	229	197	120.5
HPSW-002	2.8	1.26	5.2	0.58	3.8	12.2	2.32	17.6	3.51
HPSW-007	8.2	0.36	64.8	0.25	7.8	16.6	6.08	112	2.54
HPSW-011	3.9	0.23	36.1	0.12	7.4	19.5	6.08	63.8	3.03
HPSW-011Dup	3.8	0.22	38.9	0.11	7.4	20.7	6.54	72	2.97
HPSW-013	5.5	0.31	33.8	0.19	9.4	16.3	5.08	150	2.28
HPSW-021	0.5	0.22	1.4	0.08	0.5	2.1	0.47	1.4	0.72
HPSW-024	0.4	0.23	0.5	0.1	0.3	1.3	0.22	2.5	0.5
HPSW-027	0.2	0.22	0.8	0.08	0.2	1.3	0.25	32.8	0.55
HPR2-017	10.9	4.28	17.4	2.05	14.9	37.7	7.67	1.3	12.6
HPR2-076	1.3	0.68	3.4	0.34	2.1	6.9	1.41	45.2	2.26
CK-102	1.4	0.7	2.4	0.32	1.9	5.9	1.09	29.2	1.94
CK-107	1.5	0.57	3.4	0.3	2.1	4.5	1.03	99.4	1.47
CK-113	1.9	0.42	25.1	0.22	2.4	22.1	5.7	97	3.97
LK-NIP-1	2.3	0.83	8.9	0.31	4.4	11.8	2.6	12.5	3.26

Package	ME-MS81								
Element	Sn	Sr	Ta	Tb	Th	Tm	U	V	W
Units	ppm								
BFP-002	1	375	0.2	0.75	5.93	0.24	1.3	202	4
BFP-004	1	210	0.1	0.29	1.52	0.08	0.49	45	12
BFP-006	<1	119	<0.1	0.14	0.1	0.09	0.13	78	3
BFP-007	<1	12.6	<0.1	<0.01	0.08	0.01	<0.05	11	<1
BFP-007DUP	<1	11.7	<0.1	<0.01	<0.05	0.01	<0.05	7	1
BFP-008	<1	191.5	<0.1	0.24	0.21	0.13	0.08	146	1
BFP-009	1	258	0.2	0.67	3.33	0.26	1.03	210	2
BFP-010D	1	343	0.2	0.87	5.72	0.25	2.9	228	10
BFP-010L	1	388	0.2	0.35	4.64	0.14	1.84	49	9
BFP-013	1	115	0.4	0.39	5.83	0.19	1.59	95	4
BFP-015	1	164.5	0.5	0.22	3.84	0.1	1.72	14	6
BFP-016	<1	10.3	<0.1	<0.01	<0.05	<0.01	<0.05	14	1
HP-006	2	195.5	0.8	2.64	1.6	1.78	1.47	214	<1
HP-007	2	68.1	0.6	2.21	1.32	1.55	1.52	46	10
HP-010	<1	117	0.1	0.54	0.26	0.36	0.09	322	1
HP-015	3	80.7	0.8	3.01	1.83	2.05	1.3	253	1
HP-017	2	146.5	1.4	2.68	1.74	1.82	0.79	72	61
HP-020	<1	120.5	0.4	0.34	70.5	0.19	17.7	40	5
HP-022a	2	88.2	0.7	2.43	1.59	1.6	1.02	228	1
MRG-1	3	273	0.7	0.56	0.7	0.17	0.25	602	1
SY-3	6	304	20.4	19.9	995	11.5	649	52	1
HPSW-002	1	177.5	0.2	0.84	0.46	0.56	0.13	392	2
HPSW-007	<1	262	0.1	0.26	29.7	0.22	8.18	23	4
HPSW-011	<1	570	0.3	0.22	16.4	0.1	3.89	7	17
HPSW-011Dup	<1	512	0.2	0.23	15.75	0.11	4.41	6	10
HPSW-013	<1	618	0.3	0.24	19.2	0.16	5.06	161	6
HPSW-021	<1	117	<0.1	0.14	0.16	0.08	0.06	132	1
HPSW-024	<1	137	<0.1	0.14	0.05	0.1	<0.05	125	2
HPSW-027	<1	412	<0.1	0.15	<0.05	0.08	0.54	201	6
HPR2-017	3	63.9	0.9	2.77	1.77	1.99	1.61	252	4
HPR2-076	<1	63.3	0.1	0.5	0.26	0.31	0.16	261	<1
CK-102	<1	122.5	0.1	0.44	0.22	0.29	0.07	249	1
CK-107	1	168.5	0.1	0.36	0.25	0.26	0.2	291	20
CK-113	1	40.7	0.1	0.34	0.79	0.21	0.49	405	39
LK-NIP-1	1	163.5	0.3	0.64	1.58	0.32	0.48	291	1

Package	ME-MS81	ME-MS81	ME-MS81	ME-ICP06	ME-ICP06	ME-ICP06	ME-ICP06	ME-ICP06	ME-ICP06
Element	Y	Yb	Zr	SiO ₂	Al ₂ O ₃	Fe ₂ O ₃	CaO	MgO	Na ₂ O
Units	ppm	ppm	ppm	%	%	%	%	%	%
BFP-002	16.7	1.36	102	39.1	10.95	9.34	8.84	10.35	4.8
BFP-004	5.9	0.45	42	54.8	10.75	3.99	4.02	7.4	6.16
BFP-006	5.2	0.59	18	38.4	4.94	7.81	3.64	17.75	1.04
BFP-007	<0.5	0.04	2	28.6	0.1	8.84	0.15	34.5	0.01
BFP-007DUP	<0.5	0.04	3	29.1	0.08	8.86	0.16	34.8	0.01
BFP-008	7.8	0.83	27	36.7	6.77	10.65	7.07	19.2	1.88
BFP-009	16.6	1.6	93	43.3	11.7	9.28	6.94	9.48	5.77
BFP-010D	22	1.71	106	43.8	9.71	8.69	8.38	7.12	5.49
BFP-010L	10.1	0.97	86	52.3	13.8	3.49	7.39	4.05	8.11
BFP-013	12	1.29	176	65.5	14.6	4.44	0.75	2.21	2.96
BFP-015	6.8	0.78	122	72.6	15.15	1.54	0.24	0.23	7.11
BFP-016	<0.5	0.05	2	30	0.11	9.36	0.22	33.2	0.01
HP-006	100	12.25	354	60.4	12.8	6.96	5.29	1.48	8.45
HP-007	85.1	10.4	288	68.3	9.94	6.47	3.11	1.09	5.49
HP-010	19.8	2.37	54	53.3	13.55	12.8	6.68	7.22	3.71
HP-015	111	14.4	385	61.5	13.1	7.75	4.55	1.46	7.51
HP-017	106.5	12.4	354	55.6	12.7	7.32	4.55	1.92	6.87
HP-020	11.5	1.49	408	63	18.05	1.81	1.55	0.44	3.86
HP-022a	90.2	11.05	316	61.5	12.15	8.03	5.14	1.77	6.15
MRG-1	12	0.88	101	38.4	8.43	17.6	15.05	13.35	0.72
SY-3	687	65.9	350	59.6	11.65	6.33	8.39	2.64	4.09
HPSW-002	32.9	3.55	95	52	10.95	15	9.14	3.43	4.97
HPSW-007	11.9	1.56	413	63.3	18.15	1.63	1.5	0.53	6.61
HPSW-011	7.9	0.73	186	64.8	18.4	1.15	0.44	0.16	7.54
HPSW-011Dup	7.6	0.73	175	64.5	18.25	1.18	0.61	0.25	6.98
HPSW-013	9.9	1.23	261	59.6	23	1.46	0.26	0.37	3.08
HPSW-021	5.2	0.59	17	42	5.02	9.99	4.93	23.3	0.66
HPSW-024	5.8	0.63	12	32.5	5.34	10.65	8.86	21.8	0.57
HPSW-027	7.3	0.49	9	18.95	3.64	6.82	22.2	13.05	0.05
HPR2-017	106	13	396	58.6	12.8	7.18	4.54	1.2	7.3
HPR2-076	18.8	1.96	51	46.1	10.45	16.3	6.68	11.85	3.45
CK-102	18	2.04	46	50	15.85	10.55	9.71	8.96	2.3
CK-107	13.4	1.7	53	45.2	16.9	7.88	7.86	3.3	4.17
CK-113	11	1.63	63	28.9	16.3	26.6	3.64	6.58	0.63
LK-NIP-1	21.5	2.1	86	49.5	15.35	13.55	10.15	7.16	2.4

Package	ME-ICP06	ME-ICP06	ME-ICP06	ME-ICP06	ME-ICP06	ME-ICP06	ME-ICP06	OA-GRA05	TOT-ICP06
Element	K ₂ O	Cr ₂ O ₃	TiO ₂	MnO	P ₂ O ₅	SrO	BaO	LOI	Total
Units	%	%	%	%	%	%	%	%	%
BFP-002	2.03	0.09	0.74	0.2	0.43	0.04	0.02	13	99.93
BFP-004	0.22	0.02	0.63	0.06	0.24	0.02	0.01	11.55	99.87
BFP-006	0.81	0.27	0.23	0.11	<0.01	0.01	0.02	24.5	99.53
BFP-007	<0.01	0.12	0.01	0.11	<0.01	<0.01	<0.01	27.3	99.74
BFP-007DUP	<0.01	0.12	0.01	0.11	<0.01	<0.01	<0.01	27.2	100.45
BFP-008	0.05	0.28	0.39	0.17	0.02	0.02	<0.01	16.7	99.9
BFP-009	0.44	0.09	0.73	0.16	0.34	0.03	0.01	12.2	100.47
BFP-010D	0.12	0.11	0.9	0.15	0.45	0.04	<0.01	9.42	94.38
BFP-010L	0.12	0.01	0.32	0.15	0.18	0.04	0.1	8.38	98.44
BFP-013	3.12	0.02	0.53	0.05	0.13	0.01	0.05	5.23	99.6
BFP-015	1.5	<0.01	0.2	<0.01	0.07	0.02	0.06	1.23	99.95
BFP-016	<0.01	0.14	0.01	0.13	<0.01	<0.01	<0.01	26.5	99.68
HP-006	0.1	0.01	0.59	0.08	0.1	0.02	0.02	3.56	99.86
HP-007	0.24	0.01	0.51	0.06	0.09	<0.01	<0.01	4.77	100.08
HP-010	1.86	0.01	0.99	0.18	0.05	0.01	0.01	1.6	101.97
HP-015	1.49	<0.01	0.63	0.09	0.1	0.01	0.01	2.53	100.73
HP-017	0.75	<0.01	0.62	0.1	0.12	0.02	0.01	6.54	97.12
HP-020	9.21	<0.01	0.11	0.03	<0.01	0.01	0.05	1.27	99.39
HP-022a	1.63	0.01	0.71	0.09	0.12	0.01	0.01	3.02	100.34
MRG-1	0.17	0.07	3.75	0.17	0.05	0.03	0.01	1.2	99
SY-3	4.09	<0.01	0.14	0.33	0.51	0.04	0.05	1.25	99.11
HPSW-002	0.71	<0.01	1.46	0.25	0.13	0.02	0.01	1.01	99.08
HPSW-007	5.8	<0.01	0.11	0.07	0.03	0.03	0.06	1.93	99.75
HPSW-011	5.61	<0.01	0.12	0.01	0.13	0.07	0.08	1.01	99.52
HPSW-011Dup	6.26	<0.01	0.11	0.02	0.11	0.06	0.09	1.28	99.7
HPSW-013	10.7	<0.01	0.12	0.01	0.05	0.08	0.14	2	100.87
HPSW-021	0.03	0.31	0.32	0.12	0.02	0.01	<0.01	11.9	98.61
HPSW-024	0.06	0.31	0.26	0.15	0.01	0.01	<0.01	17.75	98.27
HPSW-027	2.53	0.21	0.18	0.21	0.01	0.05	<0.01	32.3	100.2
HPR2-017	0.06	<0.01	0.66	0.07	0.11	<0.01	<0.01	4.19	96.71
HPR2-076	1.48	0.01	0.92	0.22	0.08	0.01	0.01	2.53	100.09
CK-102	1.12	0.05	0.73	0.17	0.04	0.02	0.01	2.05	101.56
CK-107	2.98	0.06	0.77	0.2	0.05	0.02	0.02	10.1	99.51
CK-113	2.56	0.05	0.76	0.15	0.04	<0.01	0.02	10.1	96.33
LK-NIP-1	0.47	0.02	1.11	0.19	0.12	0.02	0.02	0.09	100.15

Package	ME-MS61L							
Element	Ag	Al	As	Ba	Be	Bi	Ca	Cd
Units	ppm	%	ppm	ppm	ppm	ppm	%	ppm
BFP-002	0.028	5.51	30.5	223	2.4	0.117	6.02	0.105
BFP-004	0.061	5.26	57.8	148	0.35	0.17	2.73	0.047
BFP-006	0.019	2.46	295	178	0.56	0.082	2.4	0.036
BFP-007	0.007	0.05	1.97	23	0.08	0.065	0.1	0.012
BFP-007DUP	0.008	0.04	1.56	10	0.07	0.072	0.11	0.011
BFP-008	0.028	3.55	23.3	14	0.31	0.035	4.91	0.061
BFP-009	0.063	5.89	11.95	121	1.74	0.206	4.8	0.038
BFP-010D	0.412	4.83	12.5	100	0.81	2.4	5.86	0.078
BFP-010L	1.005	6.83	7.63	911	0.67	4.67	5.04	<0.005
BFP-013	0.044	7.41	66.6	426	1.2	0.241	0.55	0.034
BFP-015	0.051	7.27	11.9	583	1.49	0.117	0.18	0.007
BFP-016	0.107	0.05	64.3	21	0.1	0.152	0.15	0.016
HP-006	0.012	6.5	2.14	196	4.59	0.029	3.78	0.153
HP-007	6.94	5.13	3.93	32	3.03	0.153	2.26	0.037
HP-010	0.036	6.63	1.44	147	0.54	0.03	4.39	0.08
HP-015	0.013	6.67	1.59	69	4.14	0.062	3.24	0.043
HP-017	1.875	6.28	28.7	63	1.01	0.476	3.33	0.055
HP-020	0.296	8.76	3.22	462	1.31	0.235	1.13	0.012
HP-022a	0.027	6	1.48	76	4.07	0.084	3.58	0.088
MRG-1	0.091	4.22	0.89	60	0.33	0.536	9.6	0.137
SY-3	0.007	5.89	20.1	470	22.3	0.295	5.48	0.191
HPSW-002	0.019	5.72	1.39	74	0.71	0.23	6.23	0.094
HPSW-007	0.355	8.5	10.15	500	2.05	0.139	1.01	0.148
HPSW-011	0.284	8.04	1.02	670	1.09	0.204	0.3	0.006
HPSW-011Dup	0.417	8.72	1.65	770	1.19	0.241	0.44	<0.005
HPSW-013	0.135	10.05	3.03	1150	5.19	0.108	0.17	0.023
HPSW-021	0.014	2.62	1.63	25	0.55	0.064	3.27	0.034
HPSW-024	0.008	2.92	7.12	8	0.56	0.02	6.13	0.034
HPSW-027	0.055	1.84	13.75	23	4.48	0.042	14	0.084
HPR2-017	0.012	6.94	2.61	8	3.64	0.305	3.28	0.012
HPR2-076	0.026	5.48	1.3	45	0.51	0.105	4.61	0.108
CK-102	0.081	7.53	2.41	67	0.31	0.243	6.56	0.056
CK-107	0.205	7.95	16.15	150	1.97	0.287	5.33	0.069
CK-113	0.268	6.24	103.5	151	1.97	1.82	2.45	0.016
LK-NIP-1	0.053	7.86	0.94	135	0.47	0.027	6.91	0.109

Package	ME-MS61L							
Element	Ce	Co	Cr	Cs	Cu	Fe	Ga	Ge
Units	ppm	ppm	ppm	ppm	ppm	%	ppm	ppm
BFP-002	88.6	42.9	480	6.98	67.2	5.96	13.7	0.18
BFP-004	38.4	29.6	87.7	0.05	47.1	2.91	7.27	0.13
BFP-006	2.08	73.5	1470	0.26	42.5	5.18	5.31	0.07
BFP-007	0.33	119.5	574	0.02	17.4	6.03	0.35	0.09
BFP-007DUP	0.18	118.5	569	0.02	15.9	5.99	0.3	0.08
BFP-008	5.48	86.1	1540	0.38	63.8	7.36	8.45	0.08
BFP-009	57	42.4	530	1.06	84.3	6.45	14.3	0.14
BFP-010D	113.5	49.4	504	0.3	31.4	5.69	16.75	0.2
BFP-010L	43.3	12	48.5	0.03	36.1	2.41	17.8	0.12
BFP-013	59.6	20.1	137	0.7	52.4	3.13	17.35	0.11
BFP-015	32.6	3	16.5	0.23	26.3	1.04	18.15	0.08
BFP-016	0.15	122	702	0.04	4.39	6.39	0.41	0.09
HP-006	43.2	9.1	24	0.13	2.56	4.76	39.7	0.13
HP-007	39.3	9.8	31.5	0.06	30.1	4.6	31.3	0.12
HP-010	8.29	41.4	75.8	0.92	116.5	8.39	14.35	0.1
HP-015	41	10.45	19.9	0.43	28.1	5.37	40.9	0.18
HP-017	46.5	10.25	24.4	0.1	41.8	4.82	21.1	0.14
HP-020	103.5	3.66	12	0.43	64	1.27	27	0.1
HP-022a	37.2	12.85	31.3	1.54	89.8	5.36	34	0.14
MRG-1	25.8	88.7	321	0.6	140.5	11.8	17.7	0.12
SY-3	>500	8.48	4.2	2.63	11.1	4.38	41.5	1.6
HPSW-002	14.6	39.8	11.5	0.28	14.9	10	17.65	0.21
HPSW-007	70.1	3.33	12.6	0.47	38.9	1.08	29.5	0.1
HPSW-011	59	1.11	16.6	0.22	27.1	0.68	19.05	0.08
HPSW-011Dup	63.6	1.255	15.6	0.26	26.5	0.79	20.4	0.09
HPSW-013	41.2	1.415	6.9	0.67	44.8	0.9	31.2	0.07
HPSW-021	2.8	86.1	1315	0.8	206	6.47	6.67	0.14
HPSW-024	1.32	106.5	1510	0.42	31	7.27	6.54	0.13
HPSW-027	1.78	55.3	979	0.72	45.5	4.41	7.32	0.08
HPR2-017	55.9	9.19	25	0.36	25.9	4.87	40.6	0.22
HPR2-076	9.26	82.4	51.9	2.68	58.7	10.95	13.05	0.21
CK-102	6.55	46.1	244	0.86	65.4	7.03	15.2	0.17
CK-107	5.06	37.2	294	4.3	143	5.03	14.7	0.1
CK-113	25	64.6	272	1.95	319	17.55	21.3	0.36
LK-NIP-1	18.25	56.4	117	0.57	165	8.95	17.7	0.16

Package	ME-MS61L							
Element	Hf	In	K	La	Li	Mg	Mn	Mo
Units	ppm	ppm	%	ppm	ppm	%	ppm	ppm
BFP-002	2.73	0.052	1.71	43.5	5.2	6.35	1520	6.15
BFP-004	1.45	0.013	0.18	16.75	0.8	4.81	486	0.77
BFP-006	0.294	0.016	0.66	0.813	4.8	10.65	800	0.41
BFP-007	0.02	<0.005	<0.01	0.168	1.7	20.6	847	0.35
BFP-007DUP	0.009	0.005	<0.01	0.086	1.7	20.9	820	0.8
BFP-008	0.425	0.032	0.04	2.2	7.6	12.15	1360	0.94
BFP-009	2.55	0.065	0.37	25.5	6.3	5.82	1230	0.54
BFP-010D	2.99	0.065	0.08	59.4	3	4.29	1170	20.5
BFP-010L	2.21	0.021	0.1	21.4	0.6	2.37	1090	674
BFP-013	3.44	0.028	2.56	29.3	2.2	1.26	414	2.48
BFP-015	3.42	0.013	1.24	15.8	0.7	0.13	32.2	2.48
BFP-016	0.018	<0.005	<0.01	0.08	3.3	20	1000	0.19
HP-006	10.4	0.182	0.08	13.45	8.1	0.85	660	2.22
HP-007	9.12	0.117	0.2	12.95	7.4	0.64	437	34.2
HP-010	1.165	0.064	1.55	3.02	24.1	4.18	1340	1.47
HP-015	10.15	0.192	1.26	11.65	13.3	0.83	700	1.16
HP-017	8.86	0.116	0.6	17.05	4.7	1.1	747	2.35
HP-020	5.69	0.011	4.62	75.1	8.6	0.25	274	5.23
HP-022a	8.14	0.164	1.31	11.8	16.8	1	727	1.24
MRG-1	3.81	0.084	0.15	9.07	3.6	8.01	1260	1.43
SY-3	9.57	0.114	3.44	1170	91.9	1.43	2360	0.64
HPSW-002	1.93	0.1	0.57	5.35	25.4	1.95	1830	1.64
HPSW-007	5.86	0.043	4.54	54.9	11.4	0.29	503	1.17
HPSW-011	3.67	<0.005	4.34	33.3	0.4	0.08	90.6	16.4
HPSW-011Dup	3.66	<0.005	5.07	37.1	0.5	0.14	167	31.7
HPSW-013	5.31	0.005	4.11	20.3	62.9	0.18	94.6	7.57
HPSW-021	0.403	0.027	0.04	1.185	42.7	14.25	887	0.31
HPSW-024	0.14	0.029	0.06	0.439	20.7	14.1	1140	0.19
HPSW-027	0.116	0.023	1.99	0.88	23.5	7.75	1500	1.02
HPR2-017	11.75	0.195	0.06	17.8	13.1	0.71	528	1.32
HPR2-076	1.485	0.063	1.2	3.44	25.3	7.25	1670	0.35
CK-102	1.24	0.05	0.82	2.32	14.6	5.22	1240	0.51
CK-107	1.38	0.164	2.29	2.24	19.8	1.81	1470	14.9
CK-113	1.72	0.11	1.71	9.74	67.5	3.4	1080	32.8
LK-NIP-1	2.23	0.065	0.37	8.15	9.6	4.22	1410	0.9

Package	ME-MS61L							
Element	Na	Nb	Ni	P	Pb	Rb	Re	S
Units	%	ppm	ppm	%	ppm	ppm	ppm	%
BFP-002	3.46	1.285	189.5	0.206	6.4	124.5	0.003	0.05
BFP-004	4.26	1.84	96.9	0.115	8.93	3.34	<0.002	0.69
BFP-006	0.729	0.18	908	0.007	11.5	22.8	<0.002	0.13
BFP-007	0.011	0.046	2850	0.002	0.29	0.11	<0.002	0.03
BFP-007DUP	0.007	0.023	2910	0.002	0.24	0.07	<0.002	0.03
BFP-008	1.395	0.147	969	0.014	1.59	1.8	<0.002	0.12
BFP-009	4.2	1.8	202	0.159	7.18	23.2	<0.002	0.18
BFP-010D	3.96	2.74	178	0.205	80	4	0.051	2.75
BFP-010L	5.79	5.11	33.2	0.083	104	1.07	0.824	1.55
BFP-013	2.13	4.3	64.2	0.054	8.29	74.3	<0.002	0.54
BFP-015	5.05	6.55	6.97	0.034	3.92	27	<0.002	1.13
BFP-016	0.006	0.028	2680	<0.001	2.34	0.14	<0.002	0.17
HP-006	6.23	14.7	10.25	0.046	3.48	2.63	<0.002	0.01
HP-007	4.07	12.95	10.2	0.044	6.99	4.63	0.015	4.64
HP-010	2.63	2.03	69.5	0.028	1.28	78.7	0.003	0.05
HP-015	5.4	15.4	11.35	0.048	4.79	29.5	<0.002	0.02
HP-017	4.9	13.65	13.25	0.051	6.5	12.9	0.002	4.05
HP-020	2.84	11.9	1.63	0.006	22.7	70.6	<0.002	0.73
HP-022a	4.31	12.55	16.1	0.053	3.1	43.3	<0.002	0.23
MRG-1	0.527	21.8	199	0.026	4.46	7.78	<0.002	0.07
SY-3	2.96	197.5	7.5	0.228	149	211	0.005	0.06
HPSW-002	3.47	4.07	23.5	0.053	1.76	19.95	0.004	0.01
HPSW-007	4.54	8.05	3.33	0.007	28	117	<0.002	0.42
HPSW-011	5.03	6.82	2.52	0.049	6.15	66	0.002	0.75
HPSW-011Dup	4.93	7.55	3.55	0.049	7.11	77.8	0.002	0.82
HPSW-013	2.06	9.74	2.01	0.02	12.2	63.8	<0.002	0.64
HPSW-021	0.472	0.299	1240	0.009	0.63	1.46	<0.002	0.08
HPSW-024	0.422	0.191	1400	0.006	0.61	2.86	<0.002	0.16
HPSW-027	0.03	0.184	798	<0.001	4.47	36.2	<0.002	0.38
HPR2-017	5.44	15.85	15.6	0.048	2.89	1.29	<0.002	0.03
HPR2-076	2.51	2.27	283	0.03	5.11	52.2	<0.002	0.56
CK-102	1.61	1.945	161.5	0.017	2.78	24.8	<0.002	0.19
CK-107	2.93	2.17	104	0.016	5.26	72.4	0.006	0.84
CK-113	0.457	2.51	181.5	0.019	9.7	21.8	0.045	7.07
LK-NIP-1	1.72	4.49	149	0.048	2.76	13	0.002	0.01

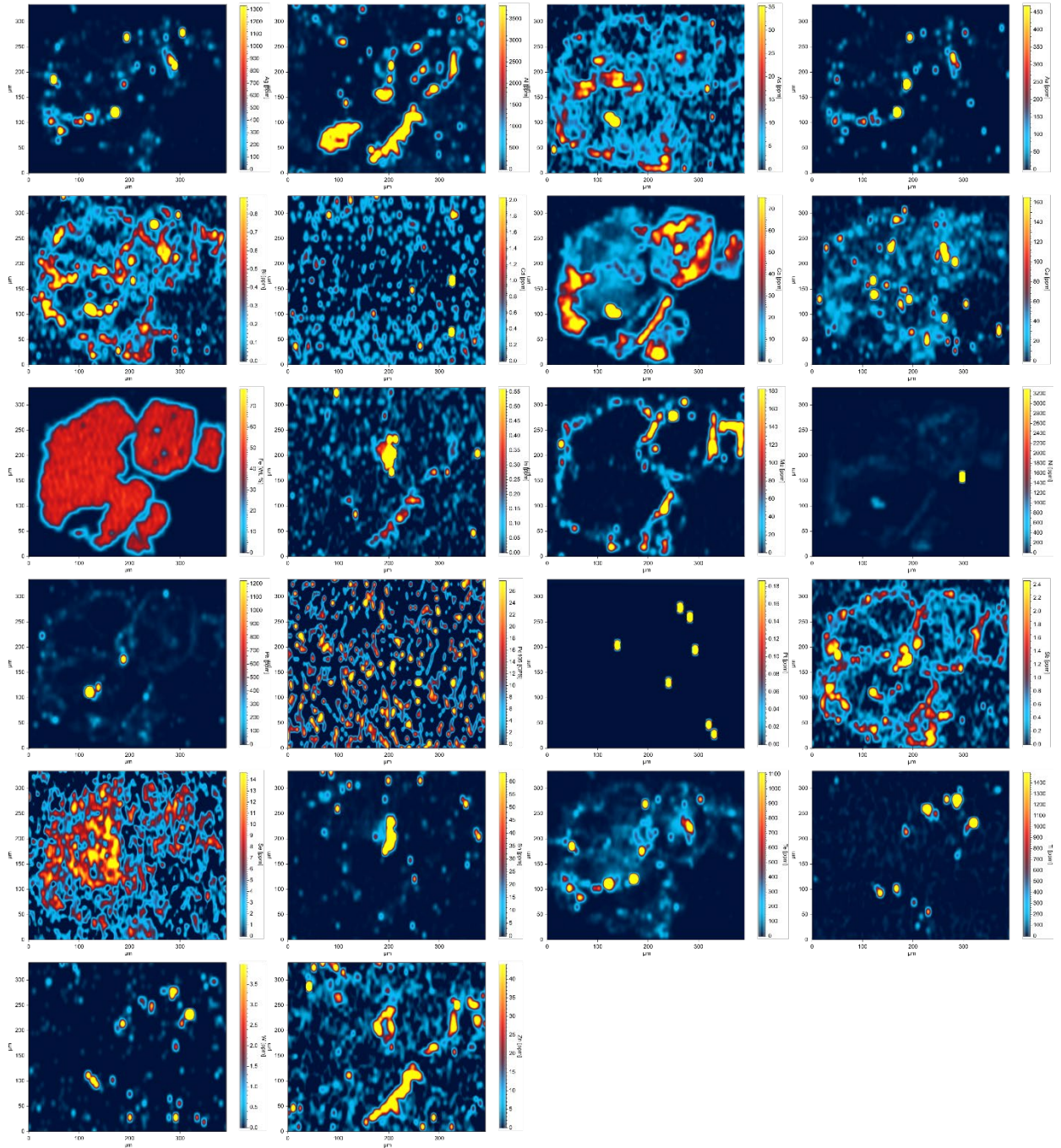
Package	ME-MS61L							
Element	Sb	Sc	Se	Sn	Sr	Ta	Te	Th
Units	ppm							
BFP-002	2.64	26.5	0.9	0.78	402	0.08	<0.04	5.8
BFP-004	0.74	26.7	1.1	0.3	222	0.07	0.12	1.645
BFP-006	0.79	17.05	0.4	0.2	123	0.01	0.05	0.078
BFP-007	0.39	2.94	0.2	0.06	13.35	<0.01	<0.04	0.065
BFP-007DUP	0.34	2.76	<0.2	0.03	12.6	<0.01	0.06	0.013
BFP-008	0.33	24.9	0.4	0.08	210	0.01	0.06	0.215
BFP-009	0.73	29.7	0.7	0.39	278	0.1	0.07	3.23
BFP-010D	1.18	32.4	2.7	1.07	365	0.11	0.62	5.9
BFP-010L	0.9	6.76	2.1	0.67	398	0.21	0.59	4.56
BFP-013	1.19	12.1	0.6	0.81	115.5	0.31	0.06	5.97
BFP-015	0.75	1.38	0.5	0.61	161	0.4	0.06	4.42
BFP-016	0.38	2.89	0.2	0.06	11.5	<0.01	0.3	0.021
HP-006	0.73	14.6	2.3	2.67	215	0.9	<0.04	1.485
HP-007	0.51	11.85	3.9	1.74	75	0.74	7.21	1.38
HP-010	0.45	44.5	1.3	0.46	124	0.13	0.04	0.26
HP-015	0.54	15.65	3.7	2.87	85	0.95	<0.04	1.655
HP-017	0.68	14.75	2.2	2.36	156	0.83	3.19	1.35
HP-020	0.54	0.87	0.9	0.35	129	0.36	0.5	70.7
HP-022a	0.34	18.9	3.9	2.44	91.3	0.74	0.05	1.515
MRG-1	0.46	54.1	1.3	3.33	302	0.87	0.06	0.812
SY-3	0.46	6.54	26.2	6.27	325	23.7	<0.04	950
HPSW-002	0.43	40.5	0.4	1	190.5	0.24	0.24	0.437
HPSW-007	0.34	1.91	0.2	0.32	254	0.11	0.8	29
HPSW-011	0.31	0.36	0.5	0.08	512	0.22	0.75	15.8
HPSW-011Dup	0.4	0.48	0.6	0.11	486	0.23	1.18	13.45
HPSW-013	0.52	0.64	0.5	0.38	537	0.33	0.75	17.55
HPSW-021	0.24	21.4	0.2	0.16	124	0.02	<0.04	0.144
HPSW-024	0.16	21.8	0.5	0.17	157.5	0.01	<0.04	0.051
HPSW-027	0.67	13.5	0.6	0.17	446	0.01	0.66	0.06
HPR2-017	0.61	16.5	<0.2	3.57	70.7	0.93	0.55	1.655
HPR2-076	0.12	39.2	0.6	0.54	71.3	0.13	0.04	0.272
CK-102	0.36	30	0.7	0.44	134.5	0.12	0.41	0.197
CK-107	2.36	36.7	0.8	0.6	172	0.12	0.17	0.162
CK-113	1.98	29	3.8	1.4	38.6	0.15	0.58	0.289
LK-NIP-1	0.1	31.8	0.5	0.79	173.5	0.28	<0.04	1.395

Package	ME-MS61L							
Element	Ti	Tl	U	V	W	Y	Zn	Zr
Units	%	ppm						
BFP-002	0.257	0.885	1.25	176	0.891	13.95	96.7	105.5
BFP-004	0.185	0.021	0.64	33	6.44	5.43	17.2	45.8
BFP-006	0.05	0.111	0.08	85.4	1.235	2.38	54.1	10.6
BFP-007	0.005	<0.004	0.05	6	0.239	0.23	51.6	0.7
BFP-007DUP	0.004	<0.004	0.01	5.4	0.219	0.12	51.3	0.6
BFP-008	0.041	0.014	0.05	144.5	0.178	2.84	69.2	17.3
BFP-009	0.184	0.134	1.04	188.5	0.983	12.05	184	97.2
BFP-010D	0.272	0.05	3.05	201	5.51	19.1	153	119
BFP-010L	0.155	0.014	1.95	46.4	8.7	8.63	20.1	91
BFP-013	0.269	0.339	1.58	87.8	3.53	7.29	34.1	129
BFP-015	0.094	0.118	1.71	13.1	5.13	5.03	8.6	118
BFP-016	0.003	<0.004	0.02	8.3	0.189	0.14	70.9	0.9
HP-006	0.351	0.021	1.47	199	0.471	61.5	70	357
HP-007	0.306	0.038	1.54	45.5	10.8	34.3	25.2	301
HP-010	0.508	0.178	0.06	280	0.341	19.8	88.8	36.6
HP-015	0.383	0.062	1.29	230	1.09	89.7	64.3	348
HP-017	0.362	0.036	0.67	69.2	64	24.3	26.4	310
HP-020	0.061	0.37	18.65	39.2	4.85	10.9	13.5	336
HP-022a	0.412	0.115	1	206	0.444	90.9	57	277
MRG-1	2.15	0.037	0.26	501	0.303	12.4	200	105.5
SY-3	0.081	1.36	635	50.4	1.105	>500	252	333
HPSW-002	0.851	0.048	0.11	366	1.845	36.2	104	48
HPSW-007	0.066	0.199	7.47	22.7	3.87	10.3	62.3	282
HPSW-011	0.065	0.194	3.47	6.8	5.74	7.68	3.1	176
HPSW-011Dup	0.068	0.239	4.25	7.7	5.7	7.72	3.7	173
HPSW-013	0.076	0.358	4.75	155.5	4.32	8.06	22	244
HPSW-021	0.106	0.008	0.07	124	0.373	3.11	51.8	12.7
HPSW-024	0.094	0.006	0.02	123.5	1.04	4.63	56.7	2.6
HPSW-027	0.079	0.148	0.55	191	4.98	8.33	46	2.2
HPR2-017	0.398	0.007	1.53	240	4.24	70.5	30.5	391
HPR2-076	0.56	0.168	0.16	258	0.164	21.6	157.5	44.3
CK-102	0.415	0.246	0.05	245	0.663	18.75	64.6	32.5
CK-107	0.452	0.537	0.15	280	19.35	8.12	72	43.4
CK-113	0.427	0.543	0.43	380	35.7	5.89	261	53.4
LK-NIP-1	0.664	0.086	0.41	275	0.312	22.8	99.3	78.3

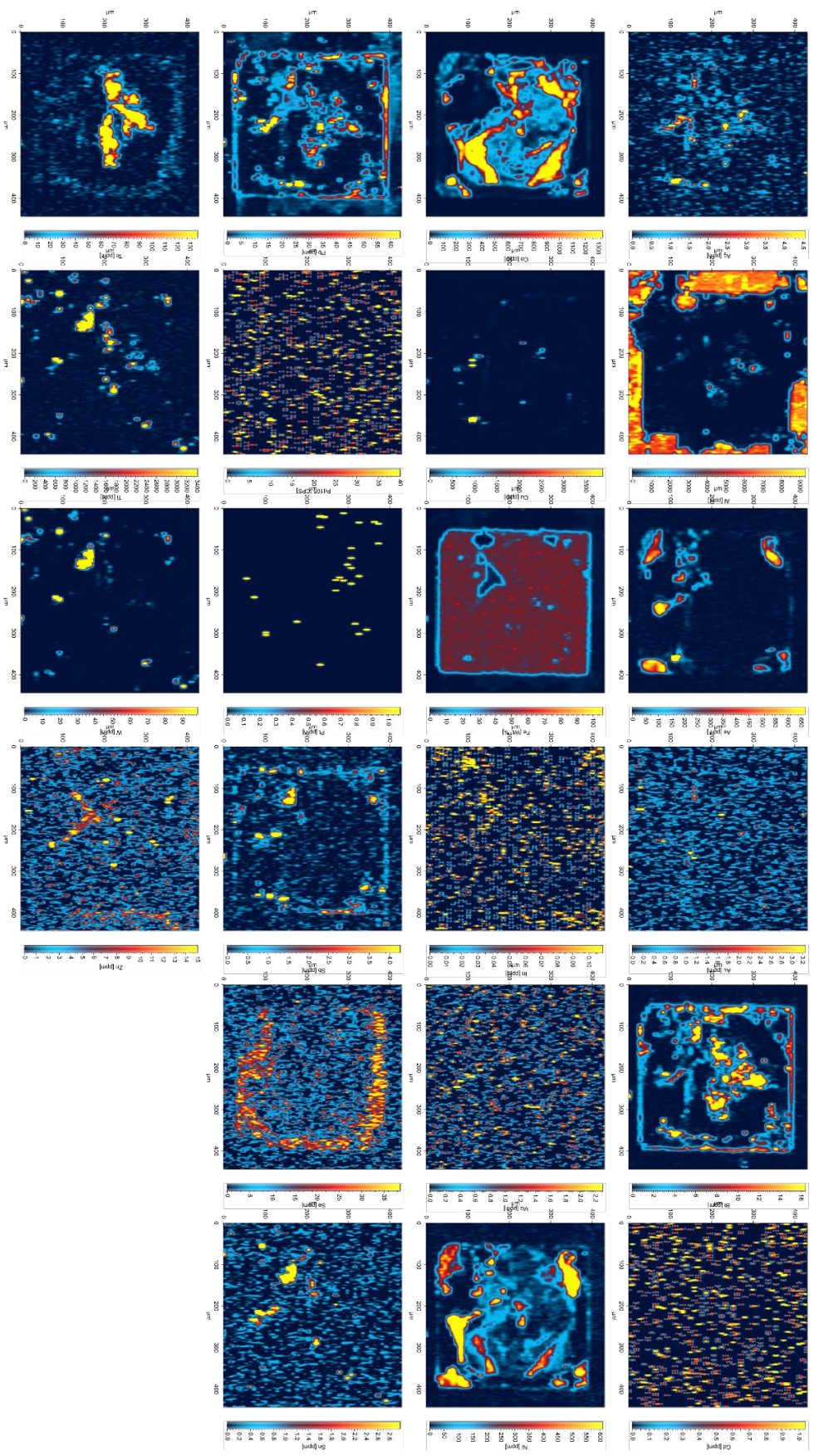
Package	Au- ICP22	Fe- VOL05	C- IR07
Element	Au	FeO	C
Units	ppm	%	%
BFP-002	0.005	3.59	3.35
BFP-004	0.449	2.7	3.31
BFP-006	0.005	6.43	6.51
BFP-007	0.002	6.58	7.1
BFP-007DUP	0.002	6.19	6.91
BFP-008	0.103	6.5	3.76
BFP-009	0.004	5.02	3.14
BFP-010D	0.034	2.7	3.33
BFP-010L	0.032	1.29	2.85
BFP-013	0.013	3.09	1.16
BFP-015	0.081	0.64	0.06
BFP-016	0.037	7.84	6.75
HP-006	0.002	0.51	1.05
HP-007	1.175	0.77	0.77
HP-010	0.005	7.71	0.08
HP-015	0.002	1.16	0.67
HP-017	1.29	1.67	1.83
HP-020	0.16	0.64	0.36
HP-022a	0.004	1.67	0.82
MRG-1	N/A	N/A	N/A
SY-3	N/A	N/A	N/A
HPSW-002	<0.001	6.86	0.28
HPSW-007	0.141	0.9	0.48
HPSW-011	0.09	0.19	0.12
HPSW-011Dup	0.109	0.25	0.21
HPSW-013	0.116	0.32	0.07
HPSW-021	<0.001	6.41	2.15
HPSW-024	0.001	6.79	3.8
HPSW-027	0.064	5.43	9.02
HPR2-017	<0.001	1.6	0.99
HPR2-076	<0.001	8.4	0.21
CK-102	0.021	6.83	0.06
CK-107	1.075	4.68	2.16
CK-113	0.6	13.05	0.84
LK-NIP-1	N/A	9.98	0.02

APPENDIX B: PYRITE LASER ABLATION MAPS

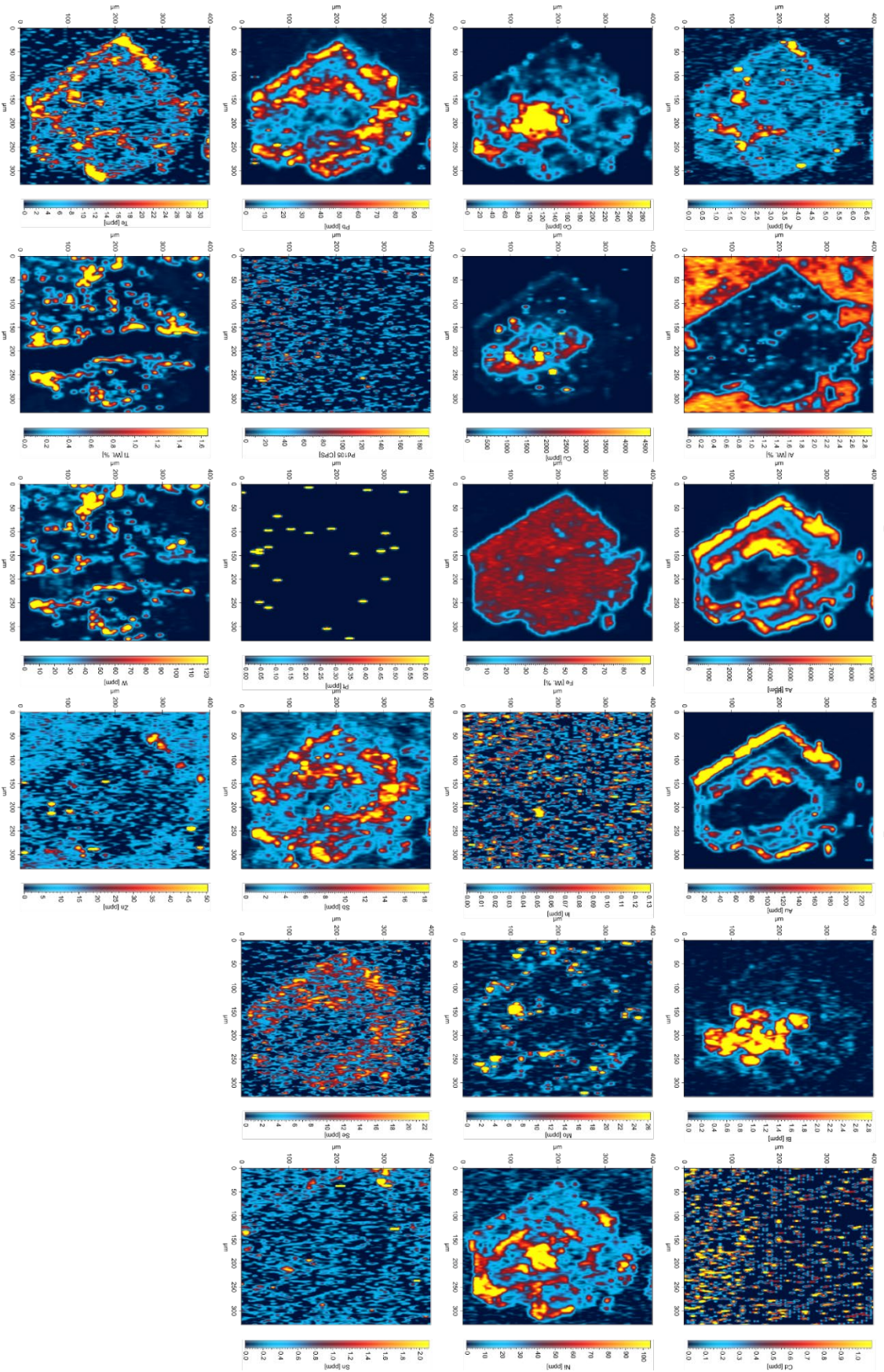
Hislop Pyrite



Black Fox Pyrite



Grey Fox 147 Zone Pyrite



Grey Fox Contact Zone Pyrite

